Dipole traps and optical lattices for quantum simulations

by

Mathis Baumert

A thesis submitted to
The University of Birmingham
for the degree of
DOCTOR OF PHILOSOPHY

Midlands Ultra-cold Atom Research Centre
School of Physics and Astronomy
College of Engineering and Physical Sciences
The University of Birmingham

December 2012

UNIVERSITY OF
BIRMINGHAM

University of Birmingham Research Archive

e-theses repository

This unpublished thesis/dissertation is copyright of the author and/or third parties. The intellectual property rights of the author or third parties in respect of this work are as defined by The Copyright Designs and Patents Act 1988 or as modified by any successor legislation.

Any use made of information contained in this thesis/dissertation must be in accordance with that legislation and must be properly acknowledged. Further distribution or reproduction in any format is prohibited without the permission of the copyright holder.

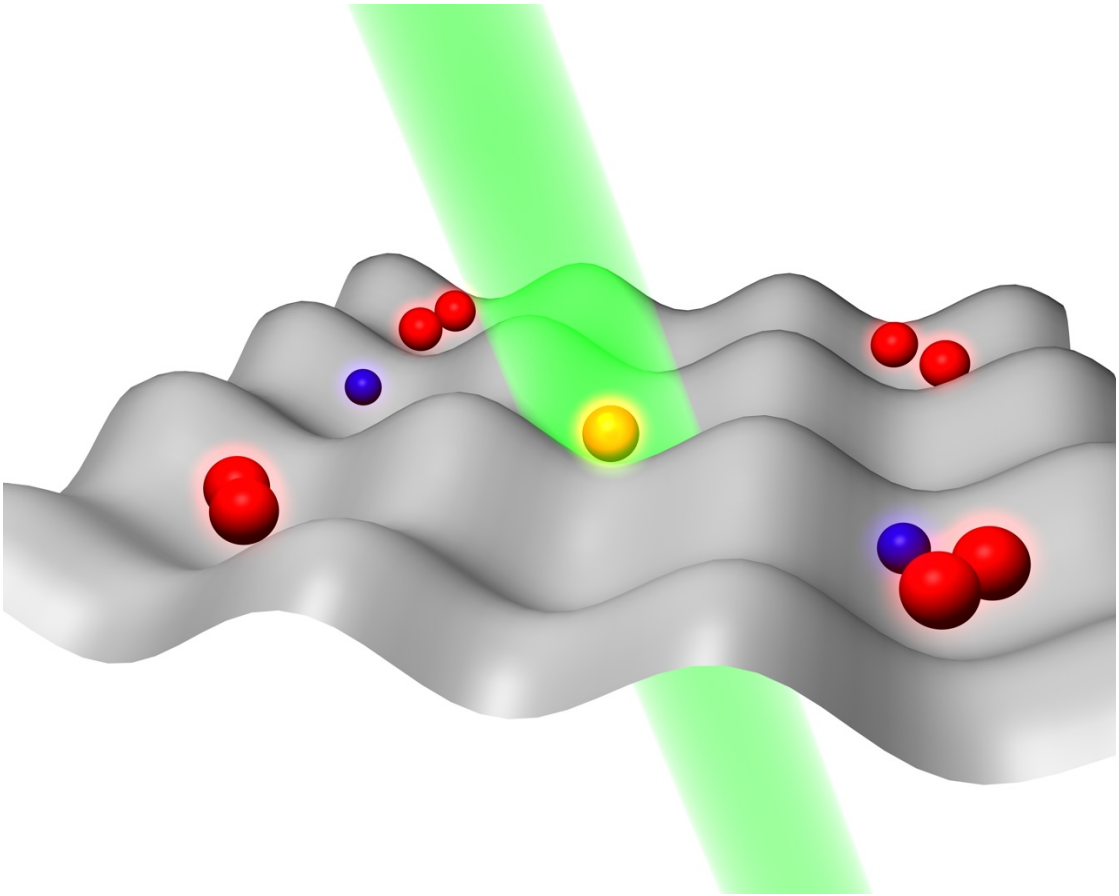

An artist's impression of single-site addressability in an optical lattice.

Abstract

Research on Bose Einstein condensates has over the past few years developed into an interesting field of physics. Current research aims for the creation of working quantum simulators which may be able to help explain and understand condensed matter physics phenomena which as yet cannot be explained. The research leading up to the experiment outlined in this thesis is intended to contribute to the understanding of these phenomena particularly that of 2D quantum systems.

In the course of this thesis trapping and manipulation schemes for dipole traps and optical lattices will be introduced. Numerical simulations have been conducted to assess the dependency of parameters leading to a stable, optimised dipole trap. The design of an aspherical dipole trap was used, set up and characterised.

Numerical simulations of maximally localized Wannier functions were carried out to obtain and understand the interactions in optical lattices and to postulate further parameters for the experiment.

A fast and stable computer control was devised using the latest field-programmable-gate-array (FPGA) technology. The robustness and versatility of this technology was proved

by adapting the software to suit different hardware and using the control in four different experiments. The electronic systems for the hardware used have been developed to yield a timing of 25ns for the digital channels and 1μs for the analogue channels.

A method to successfully transport magnetically trapped atoms with a repeatable positioning accuracy of 10μm is introduced, explained and characterized.

Contents

Chapter

1

Introduction

Since the first observation of Bose-Einstein condensation (BEC) in 1995 this field of research has evolved into a very important field of physics [1, 2]. A Bose-Einstein condensate in dilute ultracold atomic samples is a quantum many-body system where many atoms occupy a single quantum mechanical wave function. Their purity makes BECs an ideal quantum model system, which together with optical lattices [3] has led to a new field of "quantum simulations" of models for condensed matter phenomena.

In contrast to most condensed matter systems which always contain imperfections, cold atom systems are generally pure and allow for a wide range of direct or indirect detection techniques.

In recent years experiments with cold atoms have been used to simulate and investigate aspects of condensed matter and solid state physics, such as the Mott insulating phase [3], Anderson localization [4–6] and superexchange interactions [7].

However, most of these experiments have been performed in 1D or 3D, while a wide range of phenomena which are matter of current research in condensed matter physics are based on interactions that happen in 2D planes. This ranges from effects i.e. high-T_c

super-conductivity to extraordinary materials e.g. graphene. In addition 2D systems pose a problem in theoretical understanding. Whilst 1D systems are often analytically solvable and 3D systems can be approximated using mean field theories, neither of these approaches can adequately explain 2D systems. Theoretical physics has made much progress in recent years in novel numerical techniques for example, Quantum-Monte-Carlo (QMC) calculations and, in particular the utilisation of, higher computing power despite which there still exists no reliable means of checking the ability of theoretical models to predict or establish the characteristics of a 2D system.

However, a cold atom system offers the possibility to simulate 2D models in an experiment using an analogue quantum system.

The object of this thesis is to design an experiment which can act as a quantum simulator of 2D systems. For this we have to produce an optical lattice able to mimic the structure of condensed matter systems. A high level of control for the system also has to be achieved in order to manipulate and detect single atoms [8, 9]. While most cold atom experiments use indirect diffraction measurement techniques with limited resolution it is the requirement of this project that the experiment incorporate direct measurement techniques such that it is possible e.g. to distinguish atoms which occupy neighbouring lattice sites in an optical lattice with single-site resolution. Another degree of control that is required is a tunable degree of disorder as this has been shown to give rise to fascinating phenomena like the aforementioned Anderson localisation.

The pseudo phase diagram given in fig. 1.1 illustrates the phases that the differing degrees of control, incorporated in the experiment, should achieve:

- Low disorder and low interaction provides a superfluid atom sample (SF).
- No disorder and high interaction leads to the Mott insulating phase (MI).
- High disorder and no interaction results in Anderson localisation (AL).

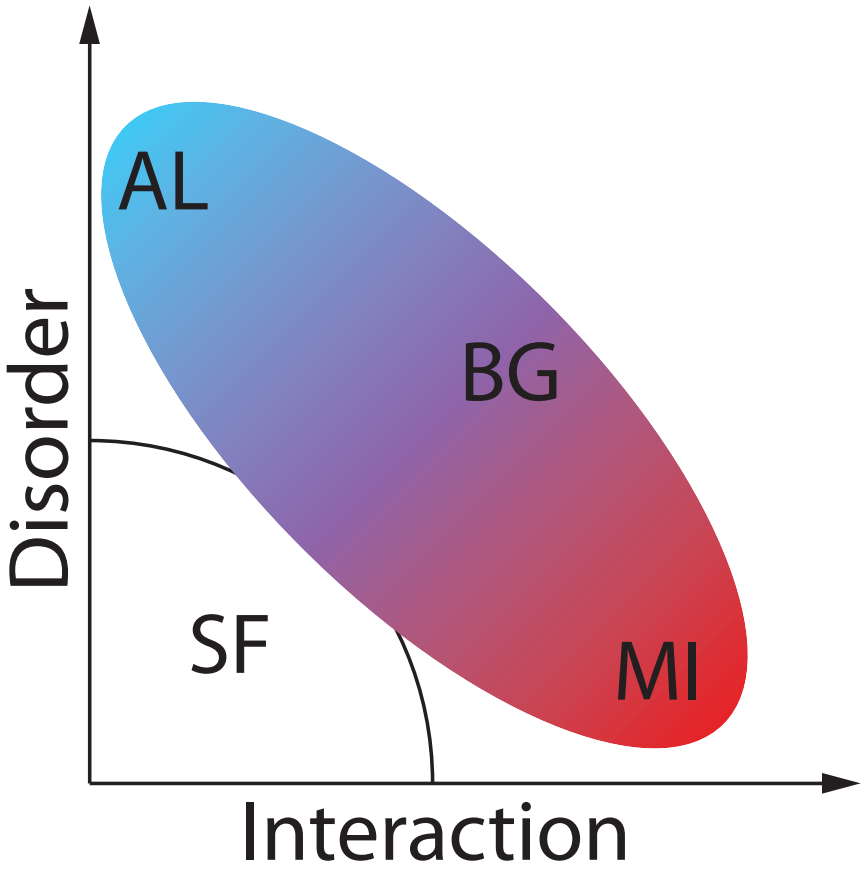

Figure 1.1: Pseudo phase-diagram showing different phases depending on the disorder strength and the interaction energy with SF: super fluid; AL: Anderson localisation; MI: Mott insulator; BG: Bose-glass. The experiment described in this thesis will be used to investigate parts of this phase diagram.

- In between both of these phases the Bose glass phase (BG) is anticipated, though not as yet realised.

The experiment described in this thesis aims to investigate the phases shown in the diagram. In doing so certain challenges have to be overcome in order to reach a satisfactory conclusion to the objective of the thesis, a quantum simulation of a 2D system.

- A brief description of the experiment layout, illustrating the way the experiment operates and listing key equipment (see ch. 2).

- A brief introduction to an experiment which investigates the behaviour of classical particles in a disordered system (see ch. 3). It will be possible to perform the proposed experiment with the set up which is described in this thesis.

- A brief theoretical description of dipole traps and optical lattices is presented (see ch. 4 and 5). This forms the basis for numerical simulations which have lead to the final design of the system. The simulation results are presented in ch. 4.6 and ch. 5.5 respectively.

- The computer control, atomic transport, UHV glass cell and dipole trap laser system are outlined together with a description of the mechanical components, computer programs, electronic hardware and their calibration (see ch. 6)

- Concludes with the current status of the experiment and outlook for future research (see ch. 7).

Chapter

2 Experiment set up

The experiment, the subject of this thesis utilises two atomic species, bosonic ^{87}Rb and fermionic ^{40}K. Previous experiments have shown that rubidium and potassium strongly interact in magneto-optical traps (MOT) and atom numbers are much reduced in mixed MOTs [10, 11], the design of the experiment utilises separate MOT systems for both species to allow for higher particle numbers. Firstly the equipment used is listed and then the operation of a typical cycle of the experiment illustrated.

2.1 Equipment

The mechanical configuration (see fig. 2.1) consists of two 2D-3D MOT vacuum chambers (A1-B1 & A2-B2) connected by vacuum tubes (C1 & C2) to an ultra high vacuum (UHV) glass cell (science chamber, D) where the actual experiments take place. For laser cooling there are several diode laser-/tapered-amplifier-systems generating light stabilized to the transition frequencies of ^{87}Rb and ^{40}K respectively. The cooling light is guided to the experiment via optical fibres. For atom capture, high current coils are used to generate

magnetic traps (in fig. 2.1 the coils E are only displayed on one MOT chamber). As the coils reach currents of up to 100A they are cooled on the bare copper of the conductors using non conductive cooling fluids (see Appendix A).

For transport of the atoms an automatic translation stage is used which has coils mounted to capture the atoms (F). Evaporation is done by a radio frequency (RF) generator which is controlled by a Raspberry Pi^{TM}. Optical trapping is accomplished using 1550nm 10W telecommunication fibre amplifiers which are fed into the dipole trap optics (G). Manipulation is done by imaging tailored patterns onto the atoms using a spatial light modulator (SLM) together with a 12W 532nm laser[1]. Imaging and manipulation is performed by using glass corrected microscope lenses[2] (H) and scientific CCD cameras. The whole experiment is controlled by a FPGA system[3]. Differential pumping stages are included at different places in order to achieve low pressures in the science chamber (I).

2.2 Operation

In the following the execution of an experimental cycle is outlined. The current status of the experiment is described in ch. 7.

Each of the species utilised will be captured in two dimensions using conventional laser cooling techniques [15–17] in individual vacuum chambers (2D MOT chamber). Afterwards the resulting string of partially cooled atoms is transferred to an adjacent 3D MOT chamber using a near resonant pushing beam. Within this chamber the atoms are recaptured and cooled in all three dimensions which in the case of Rubidium reduces the temperature to $\approx 200\mu$K. The atoms are further cooled in an optical molasses [18] which for Rubidium further reduces the temperature to $\approx 10\mu$K [19,20]. At this point the atoms are in the F = 2 hyper-fine state equally distributed over the m_F states. The magnetic

[1] Coherent Verdi V12 [12]
[2] Mitutoyo G Plan Apo 50x microscope lenses [13]
[3] National Instruments NI 7841R [14]

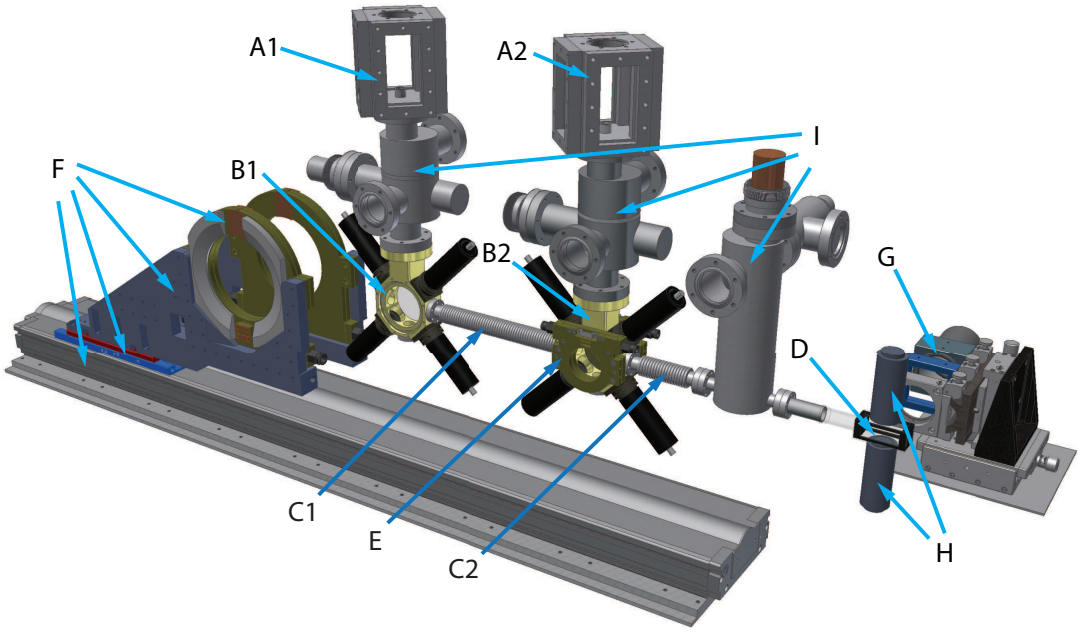

Figure 2.1: Schematic of the experiment layout with **A1**-**B1** & **A2**-**B2**: 2D-3D MOT vacuum chambers; **C1** & **C2**: connecting vacuum tubes; **D**: UHV glass cell; **E**: Coils for magneto-optical trapping and magnetic trapping; **F**: Translation stage with mounted coils used to transport the atoms to the glass cell; **G**: Optics to generate the 2D dipole trap; **H**: High-resolution microscope objective lenses used for single-site and single-atom resolution; **I**: Differential pumping stages used to achieve a low pressure in the glass cell.

trap is sensitive to the spin orientation and atoms which are not in the $m_F = +2$ state will be lost. To avoid this a short burst of circularly polarized resonant light is shone onto the atoms to transfer all atoms into the required state. Further on the magnetic field in the coils mounted onto the translation stage are ramped up and the atoms trapped inside are moved over to the science chamber. At this stage the cooling process is continued by inducing evaporative cooling by exposing the atoms to RF frequency [21]. Once the temperature has been sufficiently reduced the pancake shaped dipole trap is ramped up. The atom sample is then further cooled by reducing the laser intensity to induce further evaporative cooling. Once the now 2D atom sample reaches coherence arbitrary potentials e.g. optical lattices can be imaged onto the atoms using the SLM. After some evolution time the result are collected by imaging the sample onto a ccd camera [22, 23].

Chapter

3 Classical transport in two dimensions

Cold atom experiments in disordered systems can be generally divided into the categories of quantum experiments dominated by matterwave multipath interference and classical experiments dominated by percolation effects. Quantum effects are typically requiring very low temperatures on the order of $T \approx 10\text{nK}$ [6]. As the conditions for classical particles in disordered systems are much less stringent it is a natural step to explore these experiments first. This will also allow to acquire a very good knowledge and control of the experiment.

In a disordered system particles with sufficiently low energy are classically trapped by a system consisting of small non-connected classically allowed wells and lakes. When averaging over all realisations of the disorder, particles with an energy high enough will follow a network of classically allowed paths, also described as a percolating cluster, which allows for normal diffusion. Between the regimes of localisation and diffusion a sub-diffusion regime can be expected. With rising particle energies diffusion will become super-diffusive and eventually the particle's movement will be solely described by ballistic expansion. There also exists a sharp transition from the localised to diffusive regime

which is characterised by a critcal energy [24], the percolation threshold which is also true for the 2D systems described here. In this chapter I will introduce the theory [25] which underlies classically disordered cold atomic gases and propose measurements which can help to test predictions and thereby contribute to a better understanding of disordered 2D systems.

In the following I will introduce the fundamental terminology and parameters of disordered systems and briefly explain the different diffusion regimes. Subsequently I will give a further introduction to the percolation threshold and discuss important related parameters.

3.1 Disorder

There is a multitude of techniques to create disordered potentials one solution is to generate a speckle pattern by illuminating a scattering target with a coherent laser beam [6, 26]. The speckle size is proportional to r/R with r being the distance of the scattering target to the cold atom sample and R being the radius of the illuminating laser beam. While the beam generated in such a way has isotropic speckle grain size in radial direction the speckle size in the axial direction is much larger and shows an anisotropy between axial and radial directions. In all recent experimental attempts the speckle beam had to be shone at an angle due to experimental constraints which images this anisotropy onto the experiment. The approach that is made in this thesis is to use spatial light modulators (SLM) in order to generate arbitrary potentials to explore several of the regimes which will be introduced here including isotropic disorder potentials.

There are largely two different ways in which cold atoms can be affected by disordered potentials. First, interaction can happen on a quantum level where a single particle scatters multiple times which can lead to coherent back-scattering or localisation phenomena e.g. Anderson localisation. This is an interference phenomenon of the single particle

wave function and cannot be explained in a classical way. The key criterion for this is that there exists a high probability of a single particle scattering multiple times and interfering with itself.

In order to achieve a classical system we consider the disorder to be analogous to [25]:

$$\lambda_{dB} \ll \sigma_R \ll l_B \ll L \ll L_{loc} \tag{3.1}$$

with λ_{dB} being the de Broglie wavelength, σ_R being the characteristic length scale of the disorder. l_B is the mean free path which describes the average length scale between two subsequent scattering processes. L is the size of the system and L_{loc} is the localisation length of quantum interference effects.

If the system is tuned in a way that localisation caused by single particle interference is suppressed, strictly classical behaviour is observed. The average distance between two subsequent scatter events is given by the mean free path l_B. To limit the system to classical behaviour it has to be ensured that the distance between two subsequent scattering events is large compared to the de Broglie wavelength which means that any self-interference of a scattering particle takes place on a very long length scale. It follows that $\lambda_{dB} \ll l_B$. The effects which are described in ch. 3.2 are based purely on classical behaviour of the system.

The measure of L_{loc} in equation (3.1) is most important as according to [5] all samples in two dimensions must be localised. The localisation length depends exponentially on the product $-k_{dB} \cdot l_B$ with k_{dB} being the de Broglie wave vector. While $k_{dB} \cdot l_B \approx 1$ shows strong Anderson localisation, for weak localisation $k_{dB} \cdot l_B \gg 1$ has to be fulfilled which means that the localisation length is large compared to the system size $L \ll L_{loc}$ and can be neglected. The set up described in this thesis is able to generate disorder in the

classical limit with $k_{dB} \cdot l_B \gg 1$ down to $k_{dB} \cdot l_B < 1$ enabling the experiment to explore both the classical as well as the quantum regime [27].

A characteristic parameter of disordered systems is the mean square displacement $\langle r(t)^2 \rangle \sim Dt^\alpha$ for a particle released into the system at $t = 0$. D is a diffusion constant and α is the parameter characterising the type of diffusion. There are five categories:

Ballistic expansion $\alpha_r = 2$

This is the case of a nearly free or free particle. For the latter the mean square displacement would be $\langle r(t)^2 \rangle = v^2 t^2$ with v being the velocity of the particle.

Super-diffusion $1 < \alpha_r < 2$

Super-diffusion describes the anomalous diffusion occurring for $1 < \alpha_r < 2$. See fig. 3.1 for examples of the mean square displacement for sub-diffusion, normal diffusion and super-diffusion. An example for this is transport in organic cells which occurs at higher velocities than normal diffusion would permit. In this example the transport is fuelled by motor proteins.

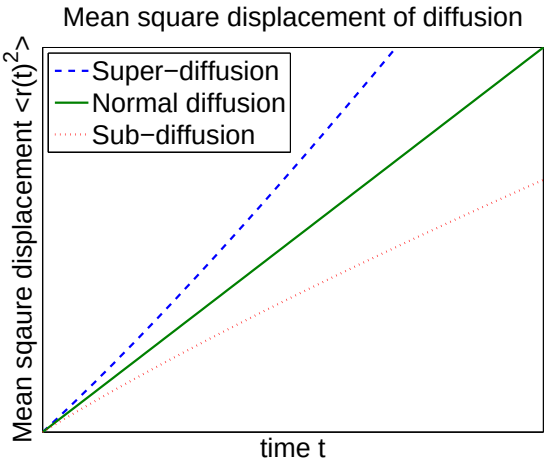

Figure 3.1: Graph showing the mean square displacement for a) sub-diffusion $\alpha_r = 0.8$; b) normal diffusion $\alpha_r = 1$; c) super-diffusion $\alpha_r = 1.2$

Normal diffusion $\alpha_r = 1$

This is the case of normal diffusion as observed in most scattering materials which can be described by the particle performing a random walk through the system.

Sub-diffusion $0 < \alpha_r < 1$

Sub-diffusion is describing any kind of anomalous diffusion with an exponent of $0 < \alpha_r < 1$. In this case diffusion is hindered by obstacles and/or traps. Again examples can be found in organic systems such as macromolecular crowding.

Localisation $\alpha_r = 0$

This is the trivial case of $\langle r(t)^2 \rangle = 0$ emphasizing the intuitive assumption that a localised particle should not move and as such its displacement is negligible. A particle released into such a system at first ballistically explores the classically allowed regions until it has scattered several times. It continues to further explore the system in a diffusive manner until it has fully explored the percolated lake it is trapped in. At this point the diffusion constant drops to zero effectively localising the particle.

3.2 Percolation threshold

Considering a disordered potential with Gaussian disorder correlation of an amplitude of E_d the classically allowed area in this potential for a certain particle purely depends on its energy E_p. If the particle energy is small it will be localised (classically trapped) to a small area which offers a potential dip deep enough to accommodate the particle. If the particle energy is large enough neighbouring potential dips will merge into larger lakes which over a certain threshold will penetrate the whole system like a percolated ocean thus allowing for normal diffusion (see fig. 3.2 a-c).

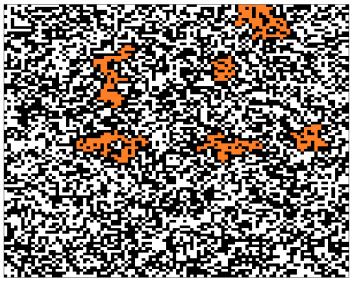

(a) $E_p/E_d = 0.5$

(b) $E_p/E_d = 0.55$

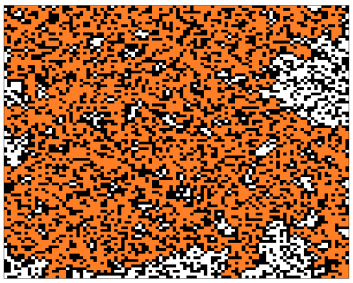

(c) $E_p/E_d = 0.6$

Figure 3.2: Graphs showing the classically allowed regions for a particle of energy E_p in disorder with an amplitude of E_d, a) With the particle energy being about half of the disorder potenial there exist only small percolated areas (examples of such coloured in orange); b) with a slightly higher energy the percolated areas increase dramatically in size ($E_p/E_d = 0.55$); c) a small further increase leads to full percolation of the system ($E_p/E_d = 0.6$)

The transition from classically trapped particles with low energy to diffusive particles is sharp and is characterised by the percolation threshold. The exact value depends on the type of disorder (e.g. Gaussian correlation) and the isotropy of the system. The steepness of the transition depends on the system size L.

3.2.1 Determining the percolation threshold by experiment

As described previously the main parameters which control the percolation threshold are the correlation of the disorder and the isotropy. The system described in this thesis has good control over both by utilizing SLMs for the generation of arbitrary potentials.
Using the new tool of single atom resolution allows new ways of imaging these effects to be used. Whilst previous experiments relied on conventional time-of-flight imaging, which images the momentum space of the atoms, the approach of this experiment gives access to the real space. Diffusion can thus be observed after a certain evolution time by measuring the density of atoms. One problem that arises however is the detection technique. Whilst dense atom clouds can easily be imaged by absorption imaging [22] using resonant light and imaging the "shadow" of the atoms onto a camera this becomes inefficient with very few atoms. The approach which has been used in recent related experiments [8, 9] is that of fluorescence imaging. However the downside of this technique is that atoms which are too close to each other engage in light induced collisions which remove the particle pairs from the trap [28]. To avoid this mechanism influencing the measurement the atomic density needs to be smaller than a critical particle density. Crude estimates using the Thomas-Fermi approximation indicate that particle numbers of $5000 - 10000$ particles would be below this critical density and could be imaged using fluorescence imaging without the influence of light induced collisions.
This makes it possible to not only identify the exact point of the percolation threshold but also to determine the critical area fraction to which the threshold is connected. This can be done by observing areas not connected to the percolated ocean which stay localised. The experiment permits the SLM-potential to be put on the camera giving unique opportunities to map the behaviour of single atoms to specific parts of the disorder, as well as studying the effects of differently correlated disorders. It also becomes possible to critically investigate the behaviour near the percolation threshold by changing individual pixels on the SLM and repeating the experiment.

Chapter

4

Optical trapping

In this chapter I will introduce the basic theory of optical dipole traps [29–32] in cold atom physics and introduce important parameters of the system to describe the efficiency of different trap designs. In particular, I will explain how trap depth and trap frequencies are determined by laser beam intensity and beam waists.

It is the aim of this chapter to illustrate a trap design which allows for the generation of a degenerate 2D Bose gas. In order to obtain a 2D system the chemical potential of the gas has to be below the energy level of the first excited state in a harmonic oscillator. This culminates in the condition: $\hbar\omega > k_B \cdot T$. With a reasonable temperature of $T = 100\text{nK}$ this implies that the trap frequency has to be larger than $\omega > 2\pi \cdot 1.3\text{kHz}$. The trap therefore, has to have a tight confinement in one direction, which from now on will be called the vertical direction, and very shallow confinement in the other two directions that is the horizontal directions. It is important that on the gas be isotropic in the 2D plane to exclude any anisotropic effects from influencing the experiment. This requires that the shallow confinement of both horizontal directions has to be the same.

In order to achieve a comparison of all trap designs the results of all trap designs have been compared to the design specifications for the experiment. The trap employed in the experiment has, in order to to meet the 2D condition stated earlier, to be able to generate a trap frequency of a few kHz. The astigmatic trap design met this requirement with a maximum trap frequency of $\omega = 2\pi \cdot 2.6\text{kHz}$ and was chosen for the experiment. In the following section a short introduction to dipolar forces will be given (ch. 4.1). Thereafter different trap layouts for 2D trapping will be examined and discussed (ch. 4.2 - 4.5). Finally the results of the calculations will be presented and compared (ch. 4.6).

4.1 Dipole trapping

The following derivations and calculations are based on [33]. In the following I will introduce the optical dipole moment in order to understand optical dipole potentials. A light field which is interacting with an atom induces a dipole moment with its electrical field vector. With α being the complex polarisability and $\vec{E}$ being the electric field vector the atomic dipole moment follows as:

$$\vec{p} = \alpha \vec{E} \tag{4.1}$$

the dipole potential of the dipole moment in the external electric field is given by:

$$U_{dip} = -\frac{1}{2}\left\langle \vec{p}\vec{E} \right\rangle = -\frac{1}{2\epsilon_0 c}\Re(\alpha) I \tag{4.2}$$

with I being the intensity of the external field. The dipole force for an atom in the laser beam follows as:

$$\vec{F}_{dip}(\vec{r}) = -\nabla U_{dip}(\vec{r}) = \frac{1}{2\epsilon_0 c}\Re(\alpha)\nabla I(\vec{r}) \tag{4.3}$$

with the polarisability α and the decay rate Γ[1] a simplified form of the dipole potential can be derived [33].

$$U_{dip}(\vec{r}) = \frac{\pi c^2 \Gamma}{2\omega_0^3}\left(\frac{2+\mathcal{P}g_{\mathrm{F}}m_{\mathrm{F}}}{\Delta_{2,\mathrm{F}}} + \frac{1-\mathcal{P}g_{\mathrm{F}}m_{\mathrm{F}}}{\Delta_{1,\mathrm{F}}}\right) I(\vec{r}) \tag{4.4}$$

This includes corrections for a multi-level system with g_{F} being the Landé factor and m_{F} the number of the ground state and $\Delta_{2,\mathrm{F}} = \omega_{5^2S_{1/2}\rightarrow 5^2\mathrm{P}_{3/2}} - \omega_{\mathrm{laser}}$ being the detuning to the $5^2S_{1/2} \rightarrow 5^2\mathrm{P}_{3/2}$ transition in units of angular frequency and $\Delta_{1,\mathrm{F}}$ the detuning in respect to the $5^2S_{1/2} \rightarrow 5^2\mathrm{P}_{1/2}$ transition while $\mathcal{P}$ is representing the polarisation of the laser beam. Linear polarisation is given by $\mathcal{P} = 0$ while $\sigma^{\pm}$ are given by $\mathcal{P} = \pm 1$.
The intensity of a focussed Gaussian laser beam is then given as:

$$I_{FB}(r,z) = \frac{2P}{\pi w^2(z)} \exp\left(-2\frac{r^2}{w^2(z)}\right) \tag{4.5}$$

with P being the power of the laser beam and w being the beam size. The scattering rate is given by [33]:

$$\Gamma_{scatt}(\vec{r}) = \frac{\pi c^2 \Gamma^2}{2\hbar\omega_0^3}\left(\frac{2+\mathcal{P}g_{\mathrm{F}}m_{\mathrm{F}}}{\Delta_{2,\mathrm{F}}^2} + \frac{1-\mathcal{P}g_{\mathrm{F}}m_{\mathrm{F}}}{\Delta_{1,\mathrm{F}}^2}\right) I(\vec{r}) \tag{4.6}$$

The beam size "w" of a Gaussian beam is defined as the radius at which the intensity drops down to $\frac{I_{max}}{e^2}$. Hence,

[1] for ^{87}Rb $\Gamma = 2\pi \cdot 6.0666\mathrm{MHz}$ [34]

$$w(z) = w_0\sqrt{1 + \left(\frac{z}{z_R}\right)^2} \tag{4.7}$$

with z being the propagation direction and the Rayleigh range being given by:

$$z_R = \frac{\pi \cdot w_0^2}{\lambda} \tag{4.8}$$

In order to establish to trap frequencies harmonic approximations are made, comparing the coefficients of the second term of the Taylor series with those of a harmonic oscillator. The zeroth and first term of the Taylor series turn out to be zero or can be neglected in the systems looked at:

$$\frac{U''_{dip}}{2!}x^2 = \frac{1}{2}mx^2\omega^2 \tag{4.9}$$

Thus with this relationship it is possible to establish the necessary parameters for optical dipole traps.

4.2 Cylindrical lens trap

The use of a laser beam able to be focussed asymetrically by means of a cylindrical lens appeared to be the simplest concept from which to proceed.
By this means advantage can be taken of the fact that Gaussian beams diverge with $\sim 1/w_0$ in the far field. A schematic of the dipole trap envisaged is given in fig. 4.1.
The x-coordinate being horizontal radial direction, the y-coordinate being the vertical radial direction and the z-coordinate being the axial direction as can be seen in fig 4.1, the intensity distribution of the laser beam related to equation (4.5) gives:

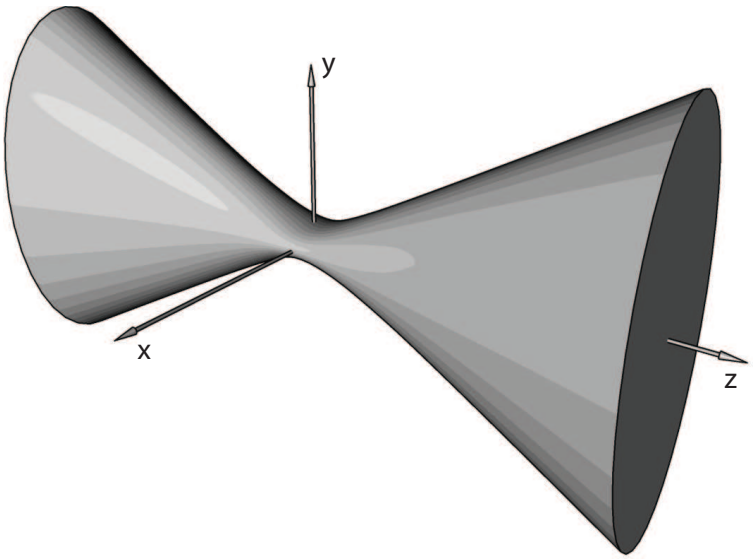

Figure 4.1: Laser beam with an asymmetrical beam profile allowing for a strong vertical confinement (y-direction) while leaving the horizontal confinement comparably weak (x- and z-direction).

$$I_{FB}(x,y,z) = \frac{2P}{\pi w_x(z) w_y(z)} \exp\left(-2\left(\frac{x^2}{w_x^2(z)} + \frac{y^2}{w_y^2(z)}\right)\right) \tag{4.10}$$

where x and y denominate the transverse directions of the laser beam while z points in the propagation direction.

The first goal is to calculate the necessary laser power of the laser beam to set the vertical trap frequency to a few kHz. Corresponding to this the aspect ratio has to be calculated so that the transverse trap frequencies are the same in both directions. The laser beam should hereby have a waist in the horizontal direction of approximately $w_h \approx 0.5$mm.

Another important factor to be established is the scattering rate of atoms in the laser beam as this can significantly reduce the life time of a degenerate gas in this trap. To establish the scattering rate the wavelengths of various commercially available lasers have been examined and compared.

In order to establish the aspect ratio which is required to obtain a circular shaped quasi 2D trap the Taylor expansion of equation (4.10) in the radial direction of the laser beam and in the propagation direction has to be derived. This results in a Taylor series of the exponential term for the radial direction and in an expansion of the $\frac{1}{w_x w_y}$ term for the propagation direction. All elements of the Taylor series except the second element are being neglected. The intensity in the vertical direction is calculated as

$$I_{vert}(y) = \frac{2P}{\pi w_{x,0} \cdot w_{y,0}} \exp\left(-2\frac{y^2}{w_{y,0}^2}\right) \tag{4.11}$$

$$I_{vert-taylor}(y) = \frac{4P}{\pi w_{x,0} \cdot w_{y,0}^3} y^2 \tag{4.12}$$

analogous to this the horizontal off-axis intensity follows as:

$$I_{hor}(x) = \frac{2P}{\pi w_{x,0} \cdot w_{y,0}} \exp\left(-2\frac{x^2}{w_{x,0}^2}\right) \tag{4.13}$$

$$I_{hor-taylor}(x) = \frac{4P}{\pi w_{x,0}^3 \cdot w_{y,0}} x^2 \tag{4.14}$$

The intensity in the axial direction follows as:

$$I_{axial}(z) = \frac{2P}{\pi w_{x,0} \cdot w_{y,0} \sqrt{1+\frac{z^2}{z_{x,R}^2}} \sqrt{1+\frac{z^2}{z_{y,R}^2}}} \tag{4.15}$$

$$I_{axial-taylor}(z) = \frac{P}{\pi w_{x,0} \cdot w_{y,0}} \left(\frac{1}{z_{x,R}} + \frac{1}{z_{y,R}}\right) z^2 \tag{4.16}$$

With the expansions of these equations and equation (4.9) it is possible to get access to the trap frequencies. The vertical trap frequency follows as:

$$\omega_{vert} = \sqrt{\frac{\pi c^2 \Gamma}{2\omega_0^3}\left(\frac{2+\mathcal{P}g_{\mathrm{F}}m_{\mathrm{F}}}{\Delta_{2,\mathrm{F}}}+\frac{1-\mathcal{P}g_{\mathrm{F}}m_{\mathrm{F}}}{\Delta_{1,\mathrm{F}}}\right)}\sqrt{\frac{8P}{\pi w_{x,0}\cdot w_{y,0}^3\cdot m_{Rb}}} \tag{4.17}$$

the horizontal off-axis trap frequency follows then as:

$$\omega_{hor} = \sqrt{\frac{\pi c^2 \Gamma}{2\omega_0^3}\left(\frac{2+\mathcal{P}g_{\mathrm{F}}m_{\mathrm{F}}}{\Delta_{2,\mathrm{F}}}+\frac{1-\mathcal{P}g_{\mathrm{F}}m_{\mathrm{F}}}{\Delta_{1,\mathrm{F}}}\right)}\sqrt{\frac{8P}{\pi w_{x,0}^3\cdot w_{y,0}\cdot m_{Rb}}} \tag{4.18}$$

the on-axis trap frequency is:

$$\omega_{axis} = \sqrt{\frac{\pi c^2 \Gamma}{2\omega_0^3}\left(\frac{2+\mathcal{P}g_{\mathrm{F}}m_{\mathrm{F}}}{\Delta_{2,\mathrm{F}}}+\frac{1-\mathcal{P}g_{\mathrm{F}}m_{\mathrm{F}}}{\Delta_{1,\mathrm{F}}}\right)}\sqrt{\frac{2P}{\pi w_{x,0}\cdot w_{y,0}\cdot m_{Rb}}\left(\frac{\lambda^2}{\pi^2 w_{x,0}^4}+\frac{\lambda^2}{\pi^2 w_{y,0}^4}\right)} \tag{4.19}$$

As the other two axes of the quasi 2D plane be of equal frequency $\omega_{axis} = \omega_{hor}$ has to be satisfied leading to the beam ratio relationship:

$$w_{x,0} = \left(\frac{4\pi^2}{\lambda^2 w_{y,0}^2}-\frac{1}{w_{y,0}^4}\right)^{-\frac{1}{4}} \tag{4.20}$$

Given start parameters for the large waist of the squeezed laser beam it is possible to calculate the necessary aspect ratio. Given the vertical trap frequency of 2.6kHz it is possible to rearrange equation (4.17) to calculate the necessary laser power for this to give:

$$P = \left(\frac{\pi c^2 \Gamma}{2\omega_0^3}\left(\frac{2+\mathcal{P}g_{\mathrm{F}}m_{\mathrm{F}}}{\Delta_{2,\mathrm{F}}}+\frac{1-\mathcal{P}g_{\mathrm{F}}m_{\mathrm{F}}}{\Delta_{1,\mathrm{F}}}\right)\right)^{-1}\frac{\pi w_{x,0}\cdot w_{y,0}^3\cdot m_{Rb}\cdot\omega_{vert}^2}{8} \tag{4.21}$$

various results will be presented in ch 4.6.

4.3 Red detuned interference trap

Another approach to the problem of creating a quasi 2D trap layout is to create a strongly confining 1D lattice in a vertical direction with red detuned laser beams [35] which cause an attractive force for the atoms. However, it is important that the single lattice planes have a large lattice spacing capable of being tuned. The easiest method to create an optical 1D lattice is by using a laser beam and superimpose upon it the retroreflected beam to create a standing wave. This arrangement has both advantages and disadvantages. The main advantage is that the set up is relatively easy to achieve. One disadvantage is that the reflected beam will inevitably be attenuated so that the lattice will not be fully modulated. The main disadvantage, however, is that the lattice spacing cannot be tuned but is fixed to a value of $\frac{\lambda}{2}$.
The main disadvantage led to the decision to adopt a different approach.Generating standing waves is not limited to retroreflected beams. Standing waves also emerge when two laser beams with the same polarisation are aimed at an arbitrary angle. The lattice spacing a is then given by:

$$a = \frac{\lambda}{2\sin(\frac{\phi}{2})} \tag{4.22}$$

where λ is the wavelength of the incoming laser beams and ϕ is the angle between the two laser beams.
Again it is important that the trap layout of the 2D plane is symmetric. A schematic of this set up is given in fig 4.2
In fig. 4.2 “d” is the diameter of the 2D disc in which the atoms are trapped. “d” corresponds to twice the beam waist in horizontal direction. As the large waist in the

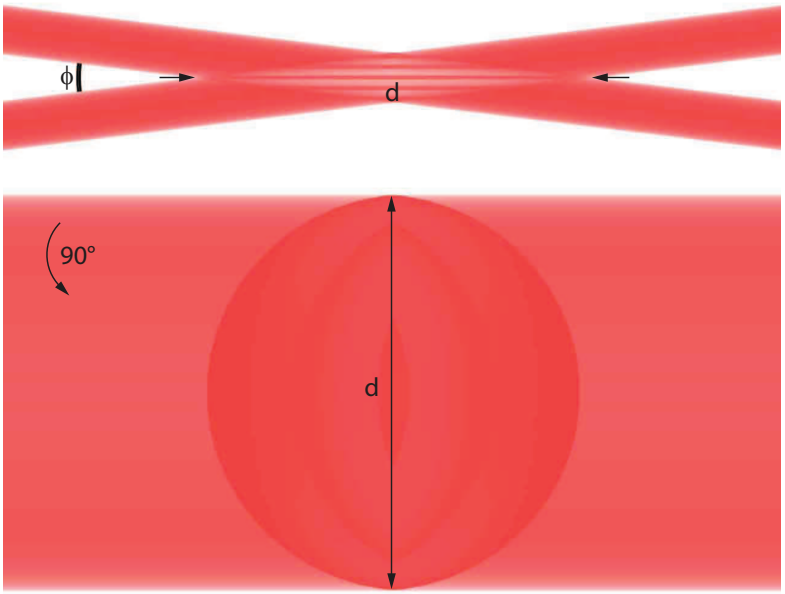

Figure 4.2: The top view shows the dipole trap set up in horizontal direction from the side with gravity pointing downwards. The coloured stripes indicate the interference pattern with "d" being the spacing between neighbouring intensity maxima and ϕ being the angle between the beams. The bottom picture is rotated by 90° with gravity pointing into the picture showing a view from the top. It can be seen that the beams have to have strongly asymmetric beam sizes in both horizontal and vertical directions in order to achieve the circular trapping region indicated by the slightly darker circle

horizontal direction is given ab initio in the same way as in the previous chapter the smaller waist will be given in proportion of the given waist by:

$$w_{y,0} = w_{x,0} \cdot \frac{\lambda}{2a} \tag{4.23}$$

Looking at the lattice confinement and the harmonic confinement separately the Gaussian shape of the laser beam will be neglected at first in calculating the trap frequency in the 1D lattice. The intensity is then given as:

$$I_{1D}(y) = I_{max} \cdot \sin^2\left(\frac{\pi}{a}y\right) \tag{4.24}$$

$$I_{max} = \frac{2P}{\pi \cdot w_{x,0} \cdot w_{y,0}} \tag{4.25}$$

with the Taylor expansion following as:

$$I_{1D-taylor} = I_{max} \cdot \frac{\pi^2}{a^2}y^2 \tag{4.26}$$

from this the trap frequency follows as:

$$\omega_{1D} = \sqrt{\frac{\pi c^2 \Gamma}{2\omega_0^3}\left(\frac{2+\mathcal{P}g_{\mathrm{F}}m_{\mathrm{F}}}{\Delta_{2,\mathrm{F}}} + \frac{1-\mathcal{P}g_{\mathrm{F}}m_{\mathrm{F}}}{\Delta_{1,\mathrm{F}}}\right)}\sqrt{\frac{4\pi P}{w_{x,0} \cdot w_{y,0} \cdot m_{Rb} \cdot a^2}} \tag{4.27}$$

analogous to this the necessary laser power for an ab initio given trap frequency:

$$P = \left(\frac{\pi c^2 \Gamma}{2\omega_0^3}\left(\frac{2+\mathcal{P}g_{\mathrm{F}}m_{\mathrm{F}}}{\Delta_{2,\mathrm{F}}} + \frac{1-\mathcal{P}g_{\mathrm{F}}m_{\mathrm{F}}}{\Delta_{1,\mathrm{F}}}\right)\right)^{-1} \frac{w_{x,0} \cdot w_{y,0} \cdot m_{Rb} \cdot a^2 \cdot \omega_{vert}^2}{4\pi} \tag{4.28}$$

Depending on these parameters it is now important to calculate the harmonic confinement of the laser beams to assess whether the arrangement is quasi 2D or not. To do this the trap frequency of a Gaussian laser beam has to be calculated once again in accordance with equation (4.18).

Having done that the results for the red detuned interference trap will be presented and compared to the other designs in ch 4.6 later.

4.4 Blue detuned interference trap

The trapping scheme discussed in this section, uses a similar approach as in ch. 4.3. However, in this case a blue detuned laser will be used. Blue detuned laser beams provide a repelling force to atoms so that they will be confined to the dark regions of the lattice instead of the bright regions populated in the red detuned case. Put simply the light intensity an atom experiences is responsible for light scattering meaning that the scattering rate for atoms in a blue detuned lattices would be much lower than for the red detuned case [33]. However, theoretical research [36] indicates that the scattering rate is dependent on the intensity gradient which is still high enough to result in comparable scattering.

The transverse confinement of the red detuned interference trap was dominated by the harmonic confinement of the lattice beams forming the lattice. In the blue detuned case harmonic confinement can be neglected, since atoms are accumulated in the regions without light. However, there exists a repelling harmonic confinement caused by the spatially dependent ground state energy. From quantum mechanics it is well known that the ground state energy of an harmonic oscillator is given by $E_0 = \frac{1}{2}\hbar\omega$. The trap frequency is influenced by the Gaussian intensity distribution whereby the ground state energy at the laser beam edges is lower than at the centre.

The previous derived equations for trap frequencies (eg equation (4.17)) show that they are dependent on the square root of the intensity. Therefore corresponding to equation (4.5) and equation (4.10), the ground state energy is distributed over the horizontal axis of the laser beam as:

$$E_0(x) = \frac{1}{2}\hbar\omega_{vert}\exp\left(-\frac{x^2}{w_{x,0}^2}\right) \tag{4.29}$$

$$E_{0-taylor}(x,\, y) = \frac{1}{2}\hbar\omega_{vert}\cdot\frac{x^2}{w_{x,0}^2} \tag{4.30}$$

with this it is possible to calculate the repelling harmonic confinement:

$$\omega_{blue-hor} = \sqrt{\frac{\hbar\cdot\omega_{vert}}{m_{Rb}\cdot w_{x,0}^2}} \tag{4.31}$$

As the confining potential is much smaller in the blue detuned case than in the red detuned case, much smaller beam waists are required to obtain the same ratio of transverse and vertical trap frequencies which requires much less laser power. The repelling confinement, however, has to be compensated by a red detuned light shift to prevent the atoms being ejected from the trap. There are advantages to the use of lower power lasers, they are cheaper to procure and use and are relatively safe in operation. Their main advantage, however, is a much reduced scattering rate of the atoms which allows much higher condensate life times. The results which have been calculated for this form of trap will be presented and compared in ch. 4.6.

4.5 Astigmatic lens trap

Since it is difficult to set up an optical system which manages to highly focus the beam in one direction and leave it fairly unaltered in the other (see ch. 4.2) it was decided to introduce an astigmatic element to shift the vertical focal point away from the horizontal [37]. This gives rise to a similar trap geometry and characteristics as in ch. 4.2. The key concept in this decision was to use a very high quality and high NA

aspherical focussing lens in combination with a high quality cylindrical lens with a very long focal length. From the standard lens equations follows:

$$\begin{aligned} \frac{1}{f_x} &= \frac{1}{f_c} + \frac{1}{f_a} - \frac{d}{f_c f_a} \\ \frac{1}{f_y} &= \frac{1}{f_a} \end{aligned} \tag{4.32}$$

with f_c being the focal length of the cylindrical lens, f_a the focal length of the aspherical lens and d the distance between both lenses. x is denominating the horizontal plane while y is indicating the vertical plane.

This results in the beam first generating a vertical focus and some distance later a horizontal focus as can be seen in fig 4.3.

While the previous trap layouts have been theoretically very simple and experimentally very hard to implement this system is theoretically difficult in conception but simple to implement. The Intensity of such a laser beam is derived from:

$$I(x,y,z) = \frac{2P}{\pi w_x(z) w_y(z)} \exp\left(-2\left(\frac{x^2}{w_x(z)^2} + \frac{y^2}{w_y(z)^2}\right)\right) \tag{4.33}$$

with:

$$\begin{aligned} w_x(z) &= w_{x,0} \cdot \sqrt{1 + \left(\frac{z - \Delta z}{z_R}\right)^2} \\ w_y(z) &= w_{y,0} \cdot \sqrt{1 + \left(\frac{z}{z_R}\right)^2} \end{aligned} \tag{4.34}$$

where Δz is the separation between the two foci. Due to the asymmetry of the trap it is not feasible to analytically describe the Taylor expansion and a numerical approach

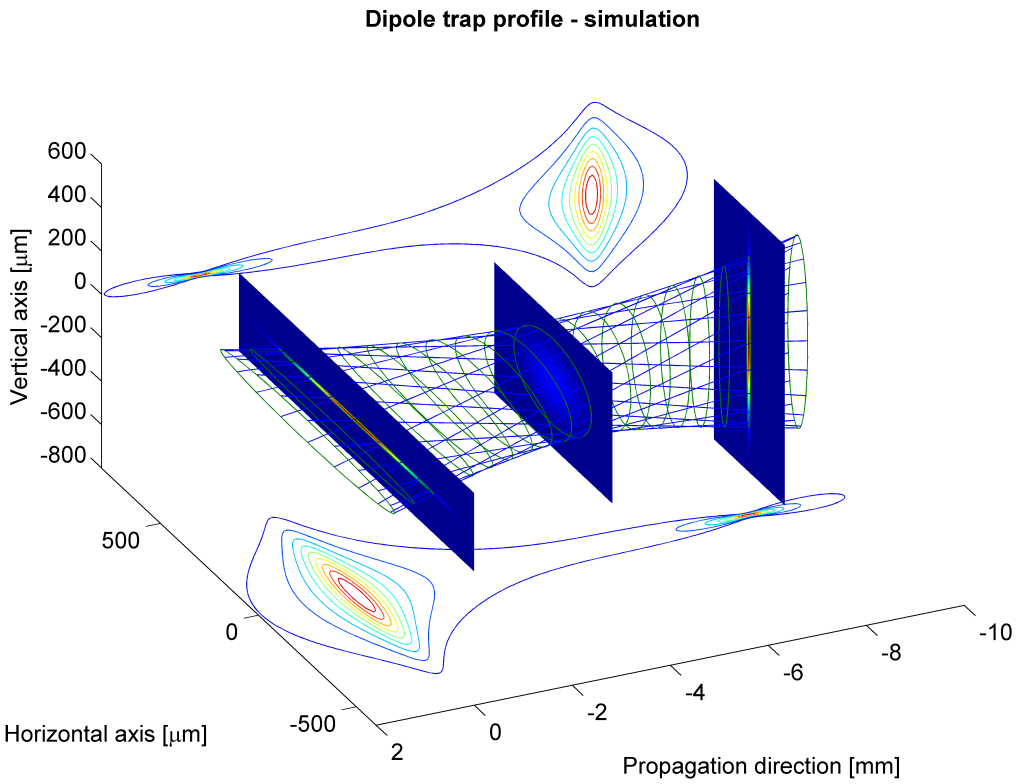

Figure 4.3: Schematic of the astigmatic dipole trap. The graph shows the horizontal (Propagation direction = 0) and vertical foci (Propagation direction = −8) as well as the intensity distributions (Contour plot in background). It can be seen that the introduction of an astigmatic element leads to a hugely asymmetrical beam profile. Parameters have been analogous to ch. 4.6.4

is taken. When numerically calculating the trap frequencies it needs to be taken into account that the trap centre will be slightly pulled out of the horizontal beam waist due to the asymmetry of the trap and gravity. The results for trapping frequencies and trap depths are discussed in ch. 4.6.4.

4.6 Results

In the following calculations the previous considerations are presented. It will be shown that with respect to laser power and system complexity the astigmatic dipole trap is the most suitable choice of trap to satisfy the objectives of the experiment.

4.6.1 Cylindrical lens trap

Evaluating the derivations of ch. 4.2, variables that have to be given ab intio are the trap frequency, the beam size and the laser wavelength. For the wavelength it was decided to utilise commercially available fibre lasers which have a wavelength of $\lambda = 1550$nm. The trap frequency will be set to $\omega_{vert} = 2\pi \cdot 2.6$kHz to achieve a tight confinement in the vertical direction and to allow for quasi 2D trapping in the horizontal direction. In the following, the necessary power will be calculated which is dependent on the waist. It was decided that the waist size chosen should be large compared to similar experiments and be within the range of $w_{x,0} = 0.2 - 0.7$mm. The necessary laser power (shown in fig. 4.4(a)) is acceptable up to a horizontal beam waist of 400μm. Looking at the harmonic confinement (see fig. 4.4(b)) this is also in acceptable limits. The ratio of vertical to horizontal trap frequency are hereby $1:30 - 1:60$ in the range of beam waists of $0.2 - 0.4$mm. In fig. 4.4(c) the resulting aspect ratio of the beams for the dipole trap can be seen which also shows the main limitation. In the usable range from $0.2 - 0.4$mm the aspect ratios range over $1:20 - 1:50$ which is experimentally difficult to implement. Specialised prisms to squeeze the aspect ratio of laser beams are commercially available. Beam quality is a key criterion to maintain, however the technical limit for this corresponds to a technical factor of six[2]. Fig. 4.4(d) is showing the resulting scattering rate Γ_{scatt} and thus a rough estimate for the inverse of the resulting condensate life time. For a beam waist of 0.4mm this corresponds to $t \approx 3.5$s. This has to be considered in

[2]Toptica variable anamorphic prism pair [38]

comparison to the necessary evolution times (see ch. 5.5). This arrangement is therefore in all aspects insufficient to meet the requirements of the experiment.

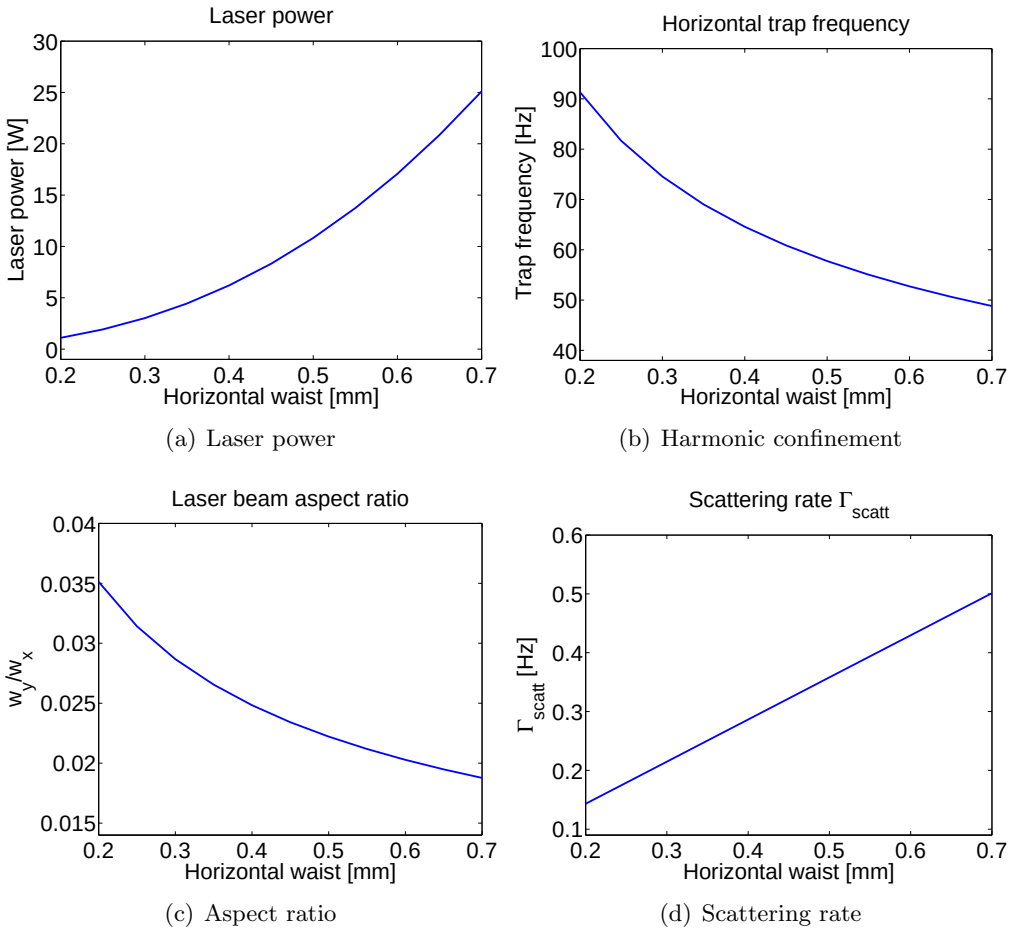

(a) Laser power

(b) Harmonic confinement

(c) Aspect ratio

(d) Scattering rate

Figure 4.4: Dipole trap with a reference trap frequency of $\omega_{vert} = 2\pi \cdot 2.6\text{kHz}$ in relation to the beam size for ^{87}Rb; wavelength of the dipole trap laser $\lambda = 1550\text{nm}$. a) shows the necessary power to achieve the reference trap frequency; b) shows the resulting horizontal confinement; c) shows the necessary beam aspect ratio in order to achieve the target trap frequency; d) shows the rate at which the Rubidium atoms scatter the off-resonant dipole trap beam.

4.6.2 Red detuned interference trap

For the interference set up the first idea was to choose a very high lattice spacing in the order of magnitude of $a = 10\mu$m. The intention behind this was that it should be easier to load a single plane in this lattice with atoms than with smaller lattice spacings. With the previously chosen parameters of $w_{x,0} = 0.4$mm and $\omega_{vert} = 2.6$kHz this leads to the laser powers shown in fig. 4.5(a). The laser power needed is comparable to that of the cylindrical lens set up. However, the horizontal trap frequency (see fig. 4.5(b)) is lower by a factor of three compared to the focussed beam trap which gives an instant advantage to this arrangement. The scattering rate is not dependent on the beam waist and has been determined as $\Gamma_{scatt} = 0.06$Hz which is lower than the results in ch. 4.6.1 and would be sufficient with an estimated life time of $t \approx 16$s.

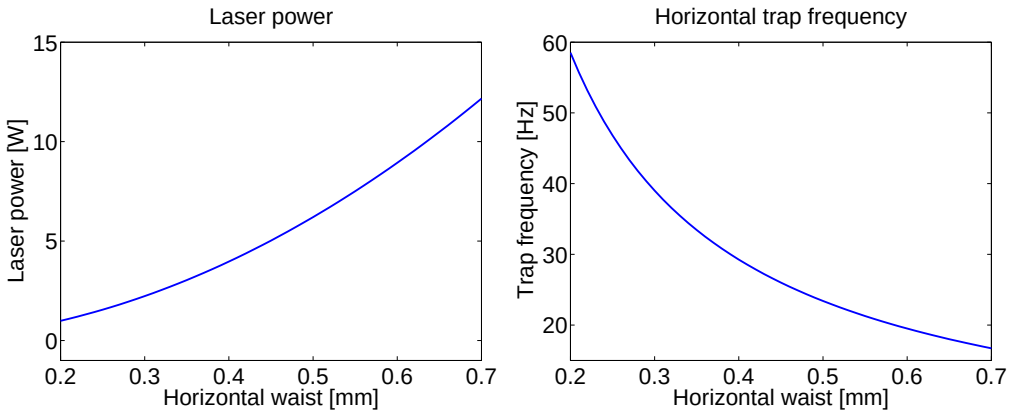

(a) Laser power (b) Harmonic confinement

Figure 4.5: Dipole trap formed by a 1D optical lattice with a reference trap frequency of $\omega_{vert} = 2\pi \cdot 2.6$kHz in dependence on the beam size for ^{87}Rb; wavelength of the dipole trap laser beams $\lambda = 1550$nm; lattice constant of 1D lattice $a = 10\mu$m. a) shows the necessary power to achieve the reference trap frequency; b) shows the resulting horizontal confinement.

By making the lattice constant variable it becomes apparent that it is possible to achieve a set up with a more suitable parameter range if lower lattice spacings were chosen (large

beam waist, very high trap frequency ratio of nearly $1:1000$). The trap frequency shows a linear dependence to the lattice spacing going down to $\omega < 2\pi \cdot 5\text{Hz}$ for small values (see fig. 4.6(b)). The necessary laser power also shows a linear behaviour and is in an accessible range with $P < 0.5\text{W}$ (see fig. 4.6(a)) for small lattice spacings. The scattering rate is also further reduced by two orders of magnitude with $\Gamma_{scatt} = 0.6\text{mHz}$ (see fig. 4.6(c)). Another advantage of lower lattice spacings comes from higher aspect ratios of the beams. As mentioned previously it is possible to deform a circular aspect ratio with the use of prisms or similar methods however this only works well for an aspect ratio of up to $1:4$. As can be seen in fig. 4.6(d) the aspect ratio is relatively easy to achieve for low lattice spacings but difficult to realise with lattice spacings of $a = 10\mu\text{m}$. The angles (see fig. 4.7(a)) under which the laser beams must be shone in are also more accessible as they are a lot larger for low lattice spacings than for the previous parameters.

4.6.3 Blue detuned interference trap

Taking the results of ch. 4.6.2 the laser power and the trap frequency for a lattice spacing of $a = 1.0\mu\text{m}$ can be seen in fig. 4.8(a) and 4.8(b) in contrast to the same graphs for $a = 10.0\mu\text{m}$ (see fig. 4.5(a) and 4.5(b)). For the blue detuned lattice it is now possible to calculate the necessary beam waist to achieve the same harmonic confinement as for the red detuned lattice (see fig. 4.9(a)). From this the necessary power for the blue detuned trap (see fig. 4.9(b)) can be calculated. This shows that a lot less laser power is necessary to achieve the same results. Taking the scattering rates for the maximum intensities for both cases shows that the blue detuned lattice has a 40% lower scattering rate. This graph has been calculated for the atoms being in the maximum of the laser intensity. If recent findings (see ch. 4.4) turn out to be accurate this then gives a realistic estimate. If these findings are not supported by future research it is reasonable to assume that the scattering will be lower as the atoms are trapped at the minimum intensity.

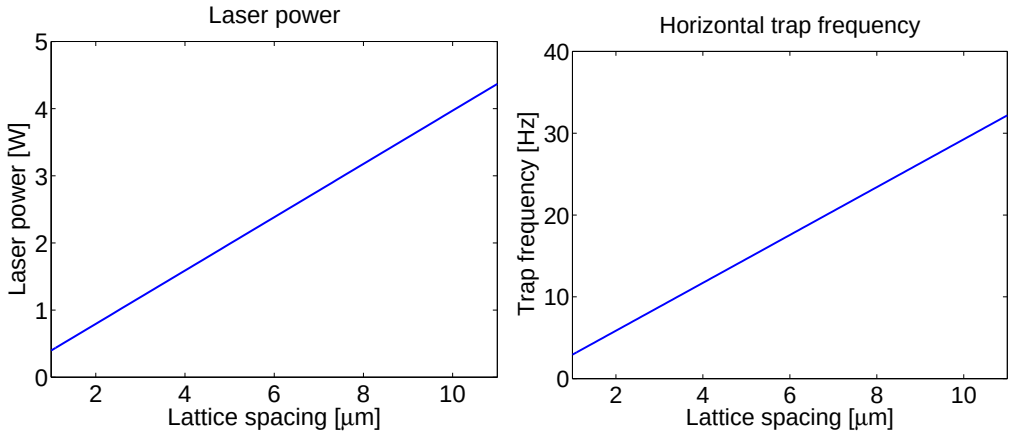

(a) Laser power

(b) Harmonic confinement

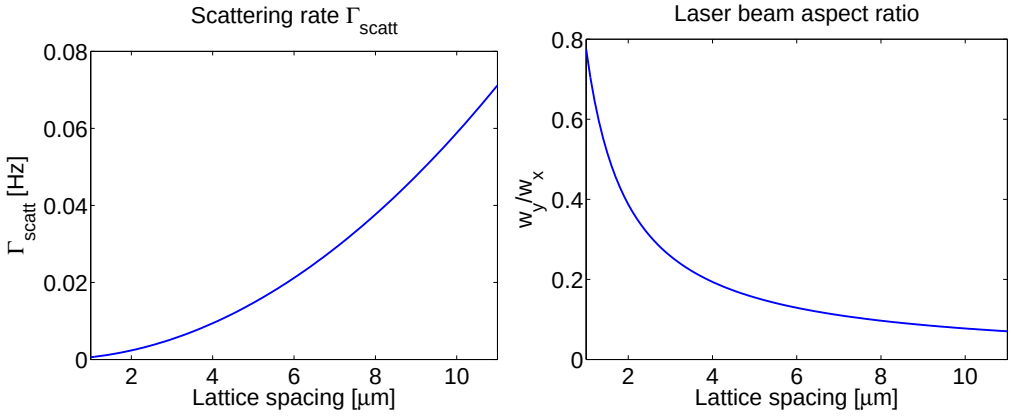

(c) Scattering rate

(d) Aspect ratio

Figure 4.6: Dipole trap formed by a 1D optical lattice with a reference trap frequency of $\omega_{vert} = 2\pi \cdot 2.6\text{kHz}$ in relation to the lattice constant for ^{87}Rb; wavelength of the dipole trap laser beams $\lambda = 1550\text{nm}$; horizontal beam size $w_{x,0} = 0.4\text{mm}$ (see fig. 4.1 for coordinate system). a) shows the necessary power to achieve the reference trap frequency; b) shows the resulting horizontal confinement; c) shows the rate at which the Rubidium atoms scatter the off-resonant dipole trap beam. d) shows the necessary beam aspect ratio in order to achieve the target trap frequency.

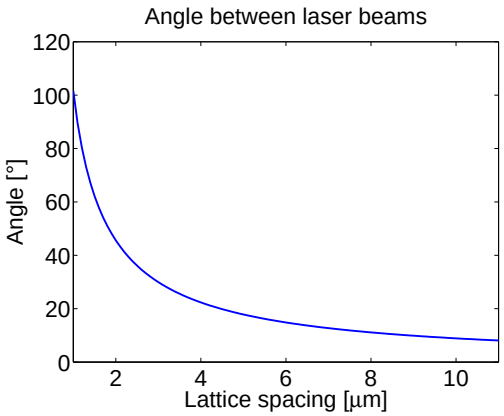

(a) Laser beam angle

Figure 4.7: Dipole trap formed by a 1D optical lattice with a reference trap frequency of $\omega_{vert} = 2\pi \cdot 2.6\text{kHz}$ in relation to the lattice constant for ^{87}Rb; wavelength of the dipole trap laser beams $\lambda = 1550\text{nm}$; horizontal beam size $w_{x,0} = 0.4\text{mm}$ (see fig. 4.1 for coordinate system). a) shows the angles between the lattice forming beams.

This gives an overall advantage for the blue detuned lattice set up. For a horizontal trap frequency of $\omega_{hor} = 2\pi \cdot 5\text{Hz}$ which gives a ratio of $\omega_{hor}/\omega_{vert} = 1 : 2000$ it follows a necessary beam waist of $w_{x,0} = 215\mu\text{m}$. In this case the resulting laser power is $P = 551\text{mW}$.

4.6.4 Astigmatic trap

In order to calculate the parameters of this set up the equations of ch. 4.2 are used to estimate the approximate aspect ratio at the horizontal focus which is then used to calculate the separation of the horizontal and vertical focus. It was decided to use $\lambda = 1550\text{nm}$ fibre amplifiers with an output power of 10W as the most viable compromise of beam power, power stability, frequency stability and cost. The light beam is switched through a single pass AOM and then coupled into a high power optical fibre leading to the dipole trap. Taking these factors into account a conservative estimate would be a maximum laser power of 5W at the point where the dipole trap is being generated.

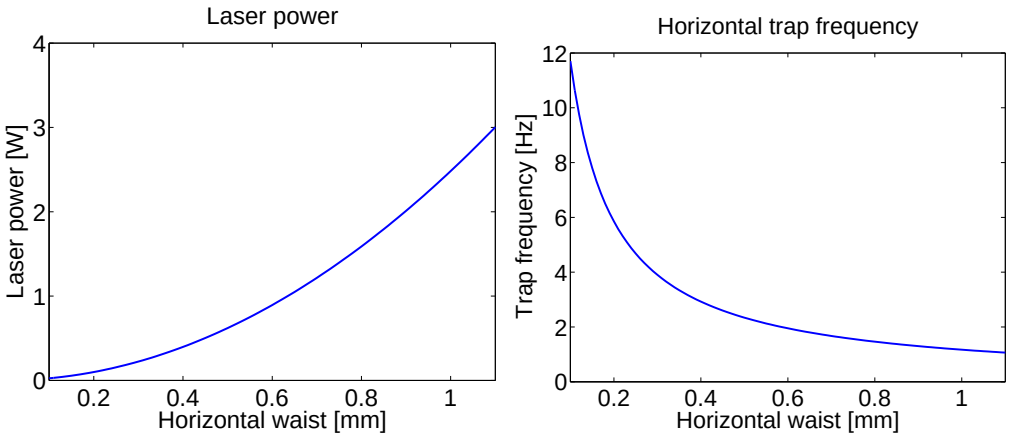

(a) Laser power (b) Harmonic confinement

Figure 4.8: Dipole trap formed by a 1D optical lattice with a reference trap frequency of $\omega_{vert} = 2\pi \cdot 2.6$kHz in relation to the beam size for ^{87}Rb; wavelength of the dipole trap laser beams $\lambda = 1550$nm; lattice constant of 1D lattice $a = 1\mu$m. a) shows the necessary power to achieve the reference trap frequency; b) shows the resulting horizontal confinement.

In order to preserve the symmetry of the two horizontal trap axes it was numerically determined that the astigmatism obeys a proportionality of $a \sim w^3$ where a is the distance between the horizontal and vertical foci. To determine the parameters we are looking into the range of $w = 5 - 20\mu$m and respectively $a = 1 - 64$mm as these are common ranges used in other experiments. Fig. 4.10(a) shows a decay of the trap frequencies at a fixed beam power which follows a strong power law with the horizontal trap frequency going down by more than a factor of 100, which is desirable, as it supports a more homogeneous 2D trapping. The vertical trap frequency at the same time goes down over this range by a factor of more than 30, which is highly undesirable as it weakens the overall confinement.

A further aspect is to examine the ratio between the vertical and horizontal trap frequencies as this indicates how close this set up is to a 2D confinement. A higher value indicates a more optimal trap for the purposes of this experiment. It can be seen in fig 4.10(b) that this ratio has a linear dependency on the beam waist with the set up being

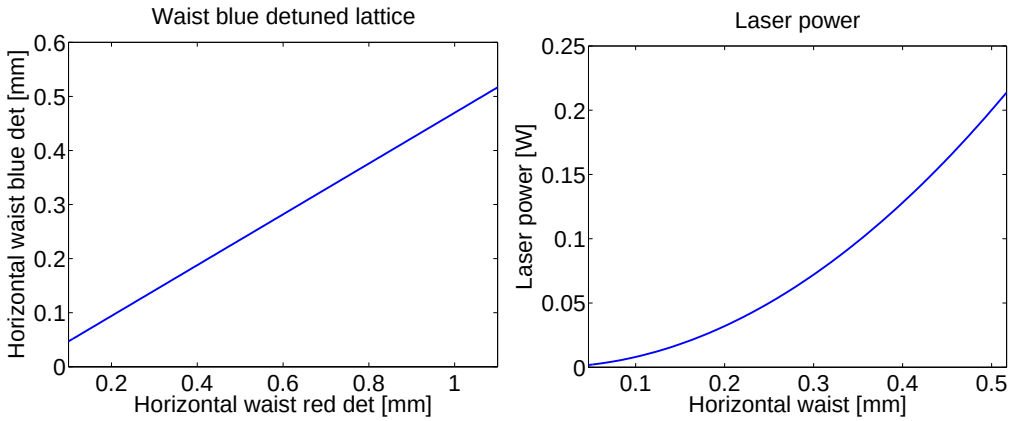

(a) Laser power (b) Harmonic confinement

Figure 4.9: Blue detuned dipole trap formed by a 1D optical lattice with a reference trap frequency of $\omega_{vert} = 2\pi \cdot 2.6$kHz in dependence on the beam size for ^{87}Rb; wavelength of the dipole trap laser beams $\lambda = 532$nm; lattice constant of 1D lattice $a = 1\mu$m. a) shows how the beam waists of fig. 4.8(a) for $\lambda = 1550$nm translate for the blue detuned lattice b) shows the necessary power to achieve the reference trap frequency in dependence of the rescaled beam size of (a).

better suited to the high end of the beam waist range. This is contrary to the overall confinement of atoms which are going to be trapped.

In order to achieve a sufficiently large vertical confinement and at the same time low horizontal confinement the horizontal waist at the point of the trap needs to be $w \approx 0.4mm$ similar to the case given in ch. 4.6.1. This leads to beam waists at the respective foci of $w_x(0) = w_y(0) = 10\mu$m with a waist separation of $\Delta z = 8$mm. This gives a vertical beam waist of $w_y = 394\mu$m at the point of the horizontal focus. Fig. 4.11(a) indicates the achievable trap frequencies in a range of 76mW to 5W of laser power. The first value indicates the minimum power at which the trap overcomes gravity. It has to be emphasized that gravity has not been taken into account in the calculations for other trap designs. It is however necessary to include this parameter for the astigmatic dipole trap chosen for this experiment, as will be explained later.

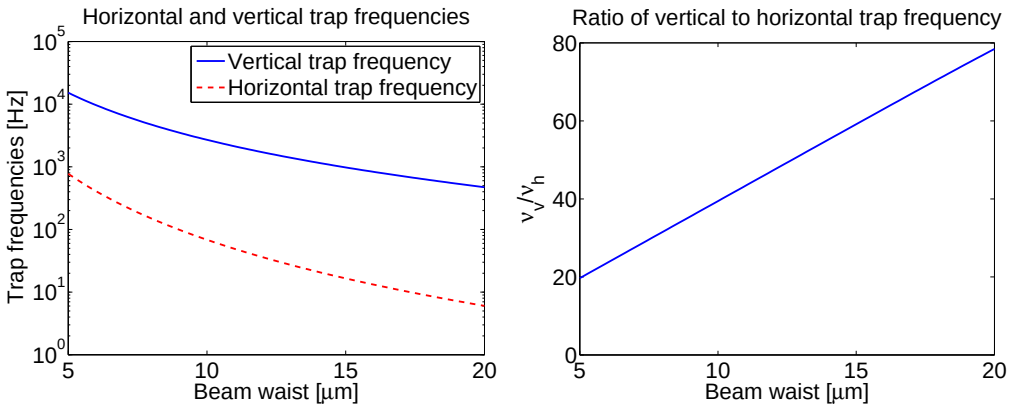

(a) Laser power (b) Harmonic confinement

Figure 4.10: Astigmatic dipole trap with maximum laser power $P = 5$W in dependence on the beam size for ^{87}Rb; wavelength of the dipole trap laser beams $\lambda = 1550$nm; the separation of the two foci varies accordingly from $a = 1-64$mm to maintain a horizontally symmetric trapping potential. a) shows how the trapping potential is strongly decaying with increasing beam size; b) shows that the ratio of vertical trapping to horizontal confinement is increasingly favourable at the same time.

It can be seen that the trap frequency takes a square root shape being proportional to $\omega \sim \sqrt{\mathrm{P}}$ which is in agreement with all previous calculations (see for example equation (4.18)). The dipole trap at this laser power corresponds to a trap depth of 63.8μK as can be seen in fig. 4.11(b). The astigmatic trap layout is similar to the cylindrical lens approach (see ch. 4.6.1).

The red detuned lattice trap relies on two beams (the two lattice forming beams) and the blue detuned lattice trap relies on at least three beams (two lattice forming beams and at least one red detuned laser beam for confinement). Both the cylindric and the astigmatic approaches feature a set up that relies on only one beam. It is this simplicity which outweighs the advantages of the lattice set ups which are noticeably at a higher ratio of vertical and horizontal trap frequencies. As the astigmatic trap is also much easier to set up compared to the cylindrical design the astigmatic design was chosen as the trap layout for this experiment. This design is able to produce a degenerate 2D Bose

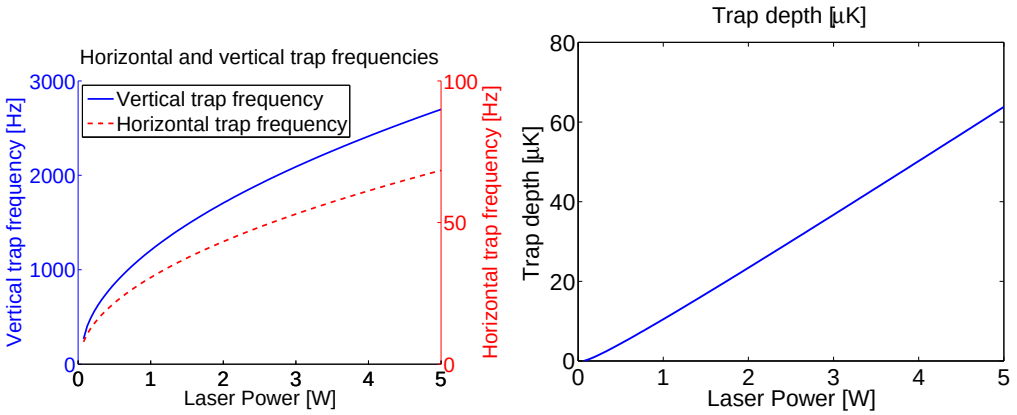

(a) Laser power

(b) Harmonic confinement

Figure 4.11: Astigmatic dipole trap with a reference trap frequency of $\omega_{vert} = 2\pi \cdot 2.6\text{kHz}$ in relation to the laser beam power for ^{87}Rb; wavelength of the dipole trap laser beams $\lambda = 1550\text{nm}$; the beam size is $w_0 = 10\mu\text{m}$ and the separation of the two foci is $a = 8\text{mm}$. a) shows the trapping frequencies of the system. Note the expected square root dependence on the power; b) is showing the trap depth of the dipole trap in units of temperature

gas with a maximum vertical confinement of $\omega = 2\pi \cdot 2.6\text{kHz}$, the key criterion, with a horizontal harmonic confinement of $\omega = 2\pi \cdot 70\text{Hz}$.

Chapter

5

Optical lattices

In this chapter I introduce the basic theory describing cold atoms in optical lattices [3, 39–43] and introduce important parameters of the system which govern phases and dynamics. In particular I will introduce the on-site interaction U and the tunnelling energy J which are important to describe the Mott insulating phase that can be generated in optical lattices. The appropriate Hamiltonian will be introduced and diagonalised in order to calculate these parameters. The results will be used to provide a representation in maximally localised Wannier functions.

These calculations will be used in order to set the parameters needed to achieve the Mott insulating phase in the operation of the equipment described in this thesis. In particular, laser intensities as well as time scales are established in order to predict evolution times when conducting the experiment.

5.1 Bose-Hubbard model

As a Bose-Einstein condensate in optical lattices is generally a many-body problem it is best dealt with a Hamiltonian in second quantisation. The Hamiltonian is as follows [40]:

$$\hat{H} = \int d^3\vec{r}\ \hat{\Psi}^\dagger(\vec{r},\, t) \left\{ -\frac{\hbar^2}{2m}\vec{\nabla}^2 + V_{ext}(\vec{r},\, t) \right\} \hat{\Psi}(\vec{r},\, t) - \frac{g}{2} \int d^3\vec{r}\ \hat{\Psi}^\dagger(\vec{r},\, t)\, \hat{\Psi}^\dagger(\vec{r},\, t)\, \hat{\Psi}(\vec{r},\, t)\, \hat{\Psi}(\vec{r},\, t) \tag{5.1}$$

with

$$g = \frac{4\pi a_s \hbar^2}{m}$$

where a_s is the scattering length of the species of atoms in the lattice[1]. V_{ext} describes the external potential which includes the lattice potential on the one hand and on the other the confining trapping potential.

Introducing localised wavefunctions in form of Wannier functions and representing the wavefunction as an expansion of these gives:

$$\Psi(\vec{r}) = \sum_{\mathrm{i}} b_{\mathrm{i}} w(\vec{r} - \vec{r}_{\mathrm{i}}) \tag{5.2}$$

b_{i} is the bosonic field operator while $w(\vec{r} - \vec{r}_{\mathrm{i}})$ represents the Wannier function (Wannier functions will be discussed in more detail in Ch. 5.3). With this equation (5.1) reduces to:

$$H = -J \sum_{\langle \mathrm{i},\, \mathrm{j} \rangle} b_{\mathrm{i}}^\dagger b_{\mathrm{j}} + \sum_{\mathrm{i}} \varepsilon_{\mathrm{i}} \hat{n}_{\mathrm{i}} + \frac{1}{2} U \sum_{\mathrm{i}} \hat{n}_{\mathrm{i}}(\hat{n}_{\mathrm{i}} - 1) \tag{5.3}$$

[1] for ^{87}Rb $a_s \approx 100 a_0 \approx 5nm$

Thereby J is the tunnelling energy and U the on-site interaction. ε takes into account that the ground state is shifted between two lattice sites because of the trapping confinement [40].

Both of these quantities can be calculated using the localised Wannier functions mentioned above. The tunnelling is presented as the tunnelling matrix elements and thus:

$$J = -\int_{\mathbb{R}} dx\ w_0^*(x - x_\mathrm{i})\hat{H}_0 w_0(x - x_{\mathrm{i}+1}) \tag{5.4}$$

where $w_0(x - x_\mathrm{i})$ is the localised wavefunction on the i-th lattice site while $w_0(x - x_{\mathrm{i}+1})$ depicts the wavefunction on the neighbouring lattice site. Taking the interaction between two atoms into account the on-site interaction emerges as:

$$U = g\int_{\mathbb{R}} dx\ |w_0(x)|^4 \tag{5.5}$$

A phase diagram derived from mean-field theory [39] predicts localised phases like the Mott insulator for optical lattices. The localisation sets in when the tunnelling is suppressed by an on-site interaction. It is predicted that this happens at $\frac{\mathrm{U}}{z\mathrm{J}} \approx 5.8$ where z is the number of next neighbours which for the common case of three dimensions is $z = 6$. In order to get a better understanding of these effects the Tunnelling and the on-site interaction energies will be calculated in the following section.

5.2 Band structure calculation

In order to calculate the essential energies of the system such as tunnelling and on-site interaction we have to set up and solve the Hamiltonian. The derivations and calculations for that are based on [44, 45]. To simplify the problem we first describe the system

in 1D and later extend the model to two dimensions. Beginning with the 1D case the Hamiltonian has a very simple form:

$$\left(\frac{p^2}{2m} + U(x)\right)\Psi(x) = E\Psi(x) \tag{5.6}$$

where $U(x) = \sin^2(x)$ is the lattice potential which is formed by the standing light wave. The lattice has periodic boundary conditions which means we can write down the wavefunction $\Psi(x)$ and the potential $U(x)$ in Fourier series representation. As the reciprocal lattice vector $|\vec{G}| = \frac{2\pi}{a}$ is defined by the lattice constant a the Fourier series of the potential will be noted as a sum over G:

$$U(x) = \sum_G U_G e^{iGx} \tag{5.7}$$

Optical lattices usually have the form of $\sin^2(x)$ or an equivalent representation thus the Fourier series is limited to the Fourier coefficients of the first and minus first order. The lattice potential consists only of Fourier components which can be represented as integer multiples of $|\vec{G}|$. In contrast to that the wavefunction is constructed of all $\vec{k}$-vectors, so that:

$$\Psi(x) = \sum_k C_k e^{ikx} \tag{5.8}$$

after inserting this into equation (5.6) it follows:

$$\sum_k \frac{\hbar^2}{2m} k^2 C_k e^{ikx} + \sum_G \sum_k U_G C_k e^{i(k+G)x} = E \sum_k C_k e^{ikx} \tag{5.9}$$

as the exponential factors on both sides of the equation have to be the same, the Hamiltonian simplifies to:

$$\left(\frac{\hbar^2 k^2}{2m} - E \right) C_k + \sum_G U_G C_{k-G} = 0 \tag{5.10}$$

writing this down as a matrix we obtain the following:

$$\begin{pmatrix} U & \lambda_{k-2G} & U & 0 & & \cdots & \\ 0 & U & \lambda_{k-G} & U & 0 & & \vdots \\ & 0 & U & \lambda_k & U & 0 & \\ \vdots & & 0 & U & \lambda_{k+G} & U & 0 \\ & \cdots & & 0 & U & \lambda_{k+2G} & U \end{pmatrix} \begin{pmatrix} C_{k-3G} \\ C_{k-2G} \\ C_{k-G} \\ C_k \\ C_{k+G} \\ C_{k+2G} \\ C_{k+3G} \end{pmatrix} = E \begin{pmatrix} C_{k-3G} \\ C_{k-2G} \\ C_{k-G} \\ C_k \\ C_{k+G} \\ C_{k+2G} \\ C_{k+3G} \end{pmatrix} \tag{5.11}$$

with E being the energy eigenvalue and:

$$\lambda_k = \frac{\hbar^2 k^2}{2m} \tag{5.12}$$

to transform this into a square matrix which can be diagonalised we assume that the Fourier components of the wavefunction converge to zero for high “k”s. With this it is

possible to cut off the Fourier series in equation (5.8) and transform the set of linear equations into a square matrix:

$$\begin{bmatrix} \lambda_{k-2G} & U & 0 & & \\ U & \lambda_{k-G} & U & 0 & \\ 0 & U & \lambda_k & U & 0 \\ & 0 & U & \lambda_{k+G} & U \\ & & 0 & U & \lambda_{k+2G} \end{bmatrix} \begin{pmatrix} C_{k-2G} \\ C_{k-G} \\ C_k \\ C_{k+G} \\ C_{k+2G} \end{pmatrix} = E \begin{pmatrix} C_{k-2G} \\ C_{k-G} \\ C_k \\ C_{k+G} \\ C_{k+2G} \end{pmatrix} \tag{5.13}$$

This matrix can be diagonalised using standard algorithms giving the eigenvalues and the eigenvectors. The eigenvalues form the energy spectrum and thus the band structure. In fig 5.1 one can see the band structure of a 1D lattice as described above:
The lattice strength is $2E_R$ where E_R is defined as the recoil energy an atom gains by absorbing one photon of the lattice laser beam and thus:

$$E_R = \frac{\hbar^2 k^2}{2m_{\mathrm{Rb}}} = \frac{\hbar^2 (2\pi)^2}{2m_{\mathrm{Rb}} \lambda_{\mathrm{lat}}^2} \tag{5.14}$$

Multiplying the components of the eigenvectors with the appropriate phase factors gives rise to the Bloch wavefunctions. In fig 5.2 you can see the Bloch functions for $k = 0$ and $k = \frac{\pi}{a}$. These have been generated using the same parameters as in [42] and are in good agreement:

5.3 Wannier functions

Next we want to calculate the on-site interaction and the tunnelling. As these are defined using localised wavefunctions (see equation (5.4) and equation (5.5)) we need to find a basis in which the extended Bloch wavefunctions interfere to localised wavefunctions.

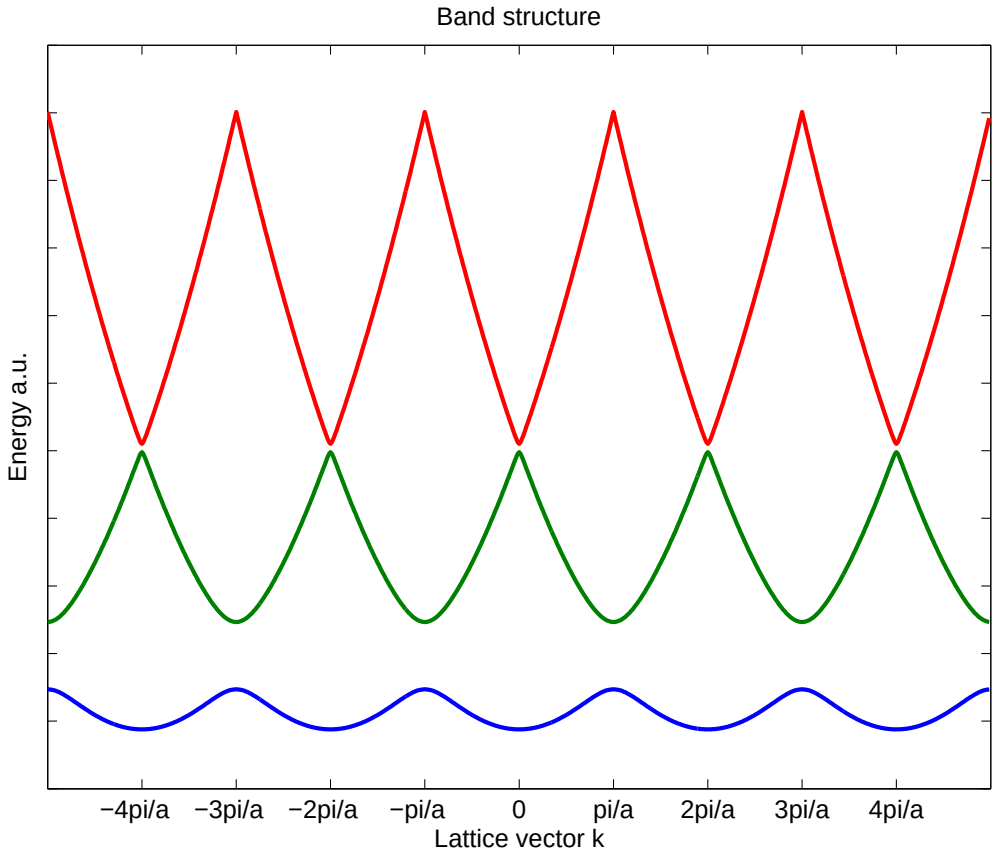

Figure 5.1: Band structure of first three bands of an infinite sinusodial lattice over six Brillouin zones. The lattice potential is $V = 2E_R$ (see equation (5.14) for definition of E_R). For the subsequent calculations it is assumed that a sample of atoms is localised to a specific energy band.

One way to solve this problem is to introduce wavefunctions in the Wannier basis. These are completely localised in the lowest Bloch band. To achieve this the band gap is considered to be large so that any coupling between the lowest and the first excited band can be neglected. In order to localise the wavefunction in the lowest band the resulting wavefunction has to be a superposition of all Bloch functions of the lowest band. It is also assumed that the lattice is finite with N lattice sites. With this the wavefunction follows as:

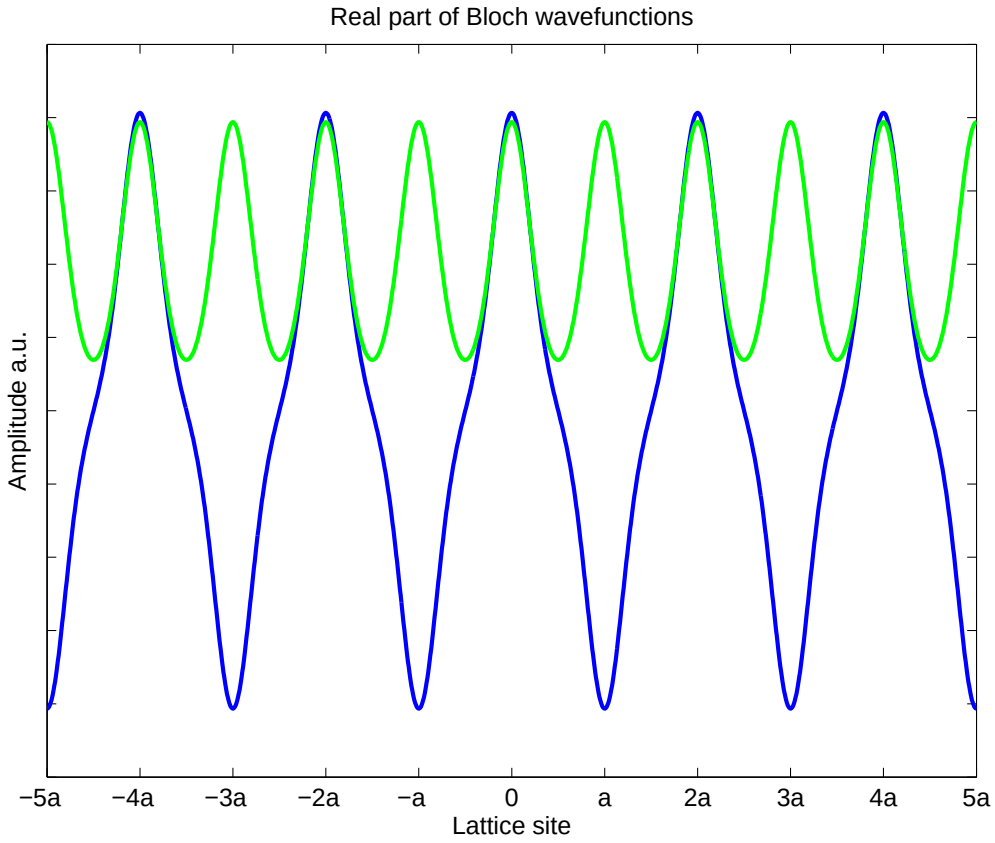

Figure 5.2: Real part of Bloch function in an infinite sinusodial lattice over ten lattice sites. The green trace is showing the lattice vector $k = 0$ and the blue trace is showing the lattice vector $k = \pi/a$. The lattice potential is $V = 8E_R$ (see equation (5.14) for definition of E_R)

$$w_n\left(x - X_\mathrm{i}\right) = \frac{1}{\sqrt{N}} \sum_{-k}^{+k} e^{-ikX_\mathrm{i}} \Psi_{n,k}(x) \tag{5.15}$$

The symmetry of the system can now be taken into consideration. It is known that the wavefunction of the lowest band (first band) has even symmetry while the first excited band (second band) has odd symetry. Taking this into account the Wannier function can be simplified to:

$$w_1\left(x - X_\mathrm{i}\right) = \frac{2}{\sqrt{N}} \sum_{0}^{+k} \cos(kX_\mathrm{i}) \Psi_{1,k}(x) \tag{5.16}$$

$$w_2\left(x - X_\mathrm{i}\right) = \frac{2i}{\sqrt{N}} \sum_{0}^{+k} \sin(kX_\mathrm{i}) \Psi_{2,k}(x) \tag{5.17}$$

5.4 2D Wannier functions

To calculate Wannier functions in 2 dimensional optical lattices the above calculations have to be adapted. The initial Hamiltonian (see equation (5.10)) evolves into:

$$\left(\frac{\hbar^2 (k_x^2 + k_y^2)}{2m} - E \right) C_{k_x,\, k_y} + \sum_{G_x} \sum_{G_y} U_{G_x,\, G_y} C_{k_x - G_x,\, k_y - G_y} \tag{5.18}$$

When representing this equation as a matrix as in equation (5.13) a problem occurs: the 2D problem has evolved into a 4D matrix which cannot easily be diagonalised. To eliminate this problem the 4D matrix is mapped onto a 2D matrix. This is achieved with taking the 2D matrices which result from taking G_y and $G\prime$ constant and mapping these 2D matrices into one large matrix. If the initial 4D matrix has $n \times n \times n \times n$ entries the reduced matrix will have $n^2 \times n^2$ entries. This allows conventional diagonalising algorithms which exist for 2D matrices to be used. Taking equation (5.10) and transforming it as outlined above gives:

$$\hat{H} = \left[\begin{array}{ccc:ccc:ccc}
\lambda_{k_x-G_x,k_y-G_y} & U_x & 0 & U_y & 0 & 0 & 0 & 0 & 0 \\
U_x & \lambda_{k_x,k_y-G_y} & U_x & 0 & U_y & 0 & 0 & 0 & 0 \\
0 & U_x & \lambda_{k_x+G_x,k_y-G_y} & 0 & 0 & U_y & 0 & 0 & 0 \\
\hdashline
U_y & 0 & 0 & \lambda_{k_x-G_x,k_y} & U_x & 0 & U_y & 0 & 0 \\
0 & U_y & 0 & U_x & \lambda_{k_x,k_y} & U_x & 0 & U_y & 0 \\
0 & 0 & U_y & 0 & U_x & \lambda_{k_x+G_x,k_y} & 0 & 0 & U_y \\
\hdashline
0 & 0 & 0 & U_y & 0 & 0 & \lambda_{k_x-G_x,k_y+G_y} & U_x & 0 \\
0 & 0 & 0 & 0 & U_y & 0 & U_x & \lambda_{k_x,k_y+G_y} & U_x \\
0 & 0 & 0 & 0 & 0 & U_y & 0 & U_x & \lambda_{k_x+G_x,k_y+G_y}
\end{array}\right] \tag{5.19}$$

This allows for diagonalisation and calculation of energy-eigenvalues and eigenvectors which form the 2D-Bloch wavefunction in the same way as the 1D problem. After diagonalisation the results can again be mapped back onto the 4D matrix to calculate the Bloch wavefunctions for each individual $k_x - k_y$ pair and following the calculation of the Wannier functions.

Whilst the 1D approach granted us access to Wannier functions of all energy bands showing a significant band gap to neighbouring bands the situation becomes more complicated in 2 or 3 dimensions. In higher dimensions the Wannier function of the second band is not complete in the representation of equation (5.15). The Wannier-function of the second band will naturally occupy the first and the second Brillouin zone. This is trivial for a 1D lattice as there is continuous connection between neighbouring Brillouin zones. This is however different in 2D and also in 3D. As can be seen in fig. 5.3(a) the Brillouin zones of the second and higher bands can not any more be easily divided into k_x and k_y components but you get a coupling of these. This leads to the Bloch functions of these k-vectors contributing to the Wannier function under non trivial phase angles. This results in a degeneracy which can only be resolved by hybridisation. Hybridisation with the third band becomes the natural choice when looking at the reduced zone scheme. This behaviour can be seen in degenerate Fermi gases in which both the second and third band are filled simultaneously [46].

It becomes apparent that the second and third band are linked as the free particle energy parabola is interrupted in the middle and divided into second and third band (see fig. 5.3(b)). The third band is the continuation of the second band while there is no such connection between the first and second band thus the Wannier function of the second band will take the form of a mixed state with the third band. It is most likely that the Wannier function will not be exponentially localised but will decay in accordance with a power law.

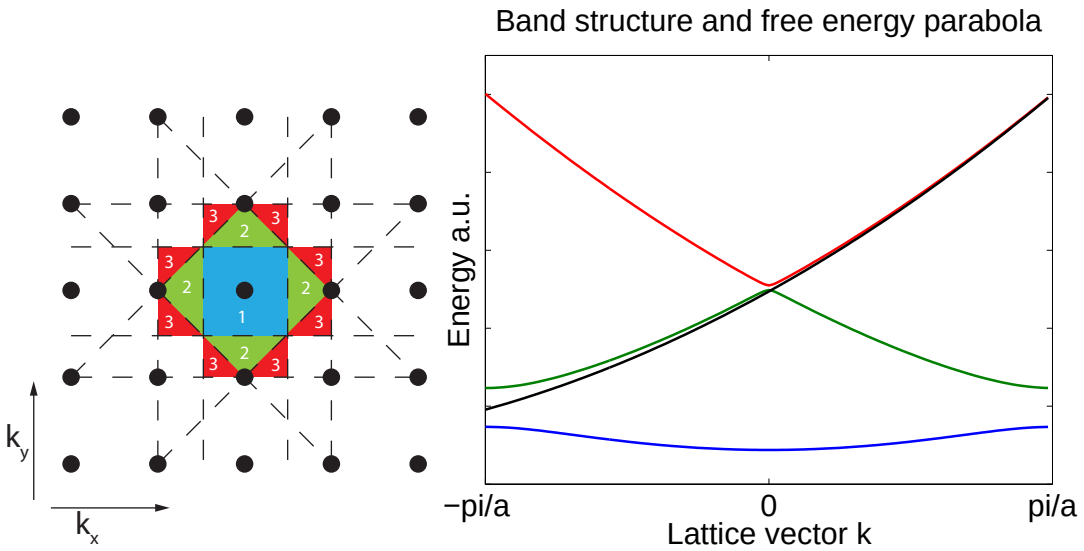

(a) Brillouin zones

(b) Reduced zone scheme

Figure 5.3: a) is showing the Brillouin zones in k-space. You can see that the second Brillouin zone does not have k_x and k_y as a basis and thus has to hybridise with the third band. b) is showing the Band structure of the first three bands in the reduced zone scheme overlayed with the free energy parabola (black line). You can see that the second band from the left is continued by the third band on the right as this is the natural path of the free energy parabola. This makes the second and third band the predestined hybridisation partners.

In the following I describe the process of calculating the pseudo-Wannier functions in 2D. These pseudo wavefunctions are the results of the evaluation equivalent to equation (5.15) in 2D without taking into account the previously discussed hybridisation. This results in wavefunctions which have no physical meaning, however, the true Wannier function can be obtained by correctly superimposing the pseudo-Wannier functions of hybridising bands. The calculation of the 2D pseudo-Wannier function in higher bands proves to be a lot more challenging than solving the problem in 1D. This occurs as a result of two main problems with the diagonalisation algorithms. The first algorithm creates a random sign for eigenvectors whilst the second is influenced by computing power a problem which will be discussed later. Whilst the eigenvector $\vec{C}_k$ is a solution to the problem so is

$-\vec{C_k}$ and which of the two is given by the algorithm is beyond our control. This seems a trivial problem at first however as the components of the eigenvectors turn out to be the frequency components of the Bloch functions, choosing the wrong eigenvector results in the introduction of random phase factors of π into the Bloch wavefunctions. This destroys the coherence of super-imposed Bloch wavefunctions and in turn causes the Wannier function to take a rather random shape. In 1D this problem can be easily solved. This is because the Hamiltonian deals only with n^2, where n is the number of Brillouin zones investigated, which allows for large numbers of n and a fine spacing in k-space. In the results presented later it was decided to select a symmetry for all calculation steps. This symmetry has been chosen because the generation of Wannier functions is effectively a Fourier transform introducing scaling anomalies when both sides of the Fourier transform are not symmetrical. Thus on the k-side of the Fourier transform the k-space is divided in $2^7 = 128$ steps and the Hamiltonian expands in the same amount of Brillouin zones. Therefore in real space each lattice site is also divided in 128 intervals and likewise the lattice expands over the same amount of lattice sites. With these parameters the calculation of a specific Wannier function takes around $1.5 - 2$s on an average computer.

In order to determine the right phase for the eigenvectors we can look at the scalar product of neighbouring eigenvectors $C_k \cdot C_{k+\delta k}$. Bloch functions with different $\vec{k}$ will by definition turn out to be orthogonal, the vectors $C_k \cdot C_{k+\delta k}$ which can be formed by the frequency components of these Bloch functions will not, however, be orthogonal. In contrast the smaller Δk the more aligned these vectors will be. This shows that the frequency components of Bloch functions, like most physical systems, avoid discontinuities and show a continuous transition of Bloch frequencies through reciprocal space. The eigenvectors can be multiplied with a factor of -1 in case $C_k \cdot C_{k+\delta k} < 0$ as can be seen in fig 5.4(a) and 5.4(b) the latter showing the continuous transition through reciprocal space.

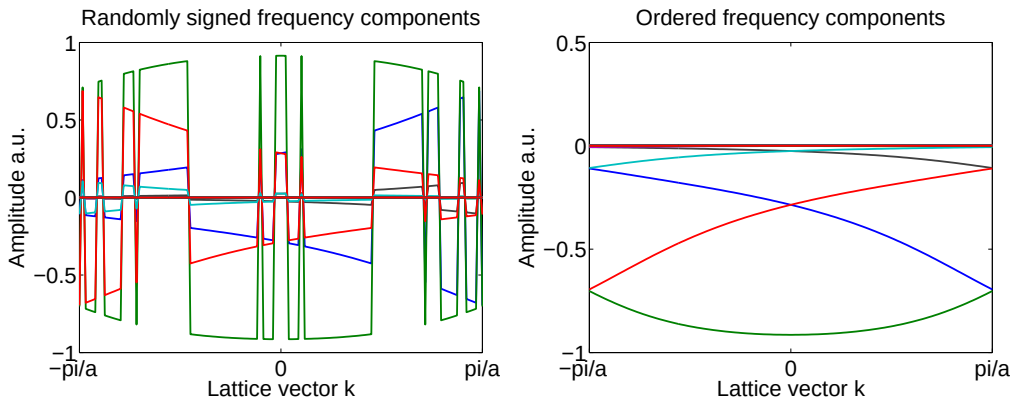

(a) Unsorted components

(b) Sorted components

Figure 5.4: Diagonalisation of equation (5.13) gives the frequency components of the Bloch function. a) showing the eigenvector components as produced by the diagonalisation algorithm and showing many discontinuities accounted by a randomly assigned factor of -1; b) is showing the same graph with the assigned random factors of -1 corrected.

While this always works for the lowest band this technique finds it's limitations in higher bands and low lattice potentials. Here it turns out that the frequency components stay near constant through most of the band but show a discontinuity at some point. There are two reasons for this. One being that by the mere definition of Wannier functions the band gaps need to be large so that the Wannier function is localised to this band. In a sinusoidal lattice this limit is quickly breached as the band gaps decay exponentially in higher bands. Secondly the potential is simply not low enough to localise the particle. In such a case one would expect a delocalised wavefunction in real space which leads to a peaked localisation in k-space. This is in agreement with the evolution of Bloch frequencies in k-space that we see. It follows, therefore, that great care need to be taken when analysing the results for higher bands and low potentials.

In 2D further problems occur which are mostly related to computing time in conjuction with the previously discussed random sign frequency vector problem. Firstly the 2D Hamiltonian scales with n^2 in each matrix direction or n^4 in means of total entries as

previously described. When taking $n = 2^4 = 16$ samples and using this also as the number of intervals in k-space this results, on the same average computer as before, in calculation times of around 30s while doubling that leads to 100min. The technique using scalar products to overcome the random sign problem works equally well for the lowest band as in 1D but finds it's limitations in higher bands. Also because of the aforementioned hybridisation we can expect kinks and other discontinuities in the Bloch frequencies. While most of the scalar products still show an alignment of neighbouring vectors of around ± 0.95 there are transitions where the alignment goes down to $\approx \pm 0.7$. When looking at the resulting graphs it is often impossible to tell, by sight, which sign is right as discontinuities exists in some frequencies whilst the remainder are running continuously (see fig. 5.5). To change the sign changes the frequencies at which others appear discontinuous. There are also scalar products of neighbouring vectors which show clear orthogonality with results of around $\pm 10^{-14}$. Two things are needed to enable the successful calculation of higher band pseudo-Wannier functions in 2D using the computer code developed to derive the calculations. A higher resolution in k-space and respectively the number of Brillouin zones taken into account and a more "clever" code in deciding the phase of the eigenvectors.

The big increase in computing time can be explained by trying to better understand modern diagonalisation algorithms based on Schur decomposition. Such an algorithm uses computing time n^3 [47]. As the matrix length is proportional to n^2 in this case due to the 4D $\rightarrow$ 2D mapping this results in the Schur decomposition being $n^{2^3} = n^6$. As mentioned before a strict symmetry is kept between numbers of sites being considered and intervals at one site. This adds an extra factor of n^2 of Hamiltonians requiring diagonalising resulting in an overall scaling factor of n^8. This is in agreement with the increase of computing time and highlights the key problem outlined earlier.

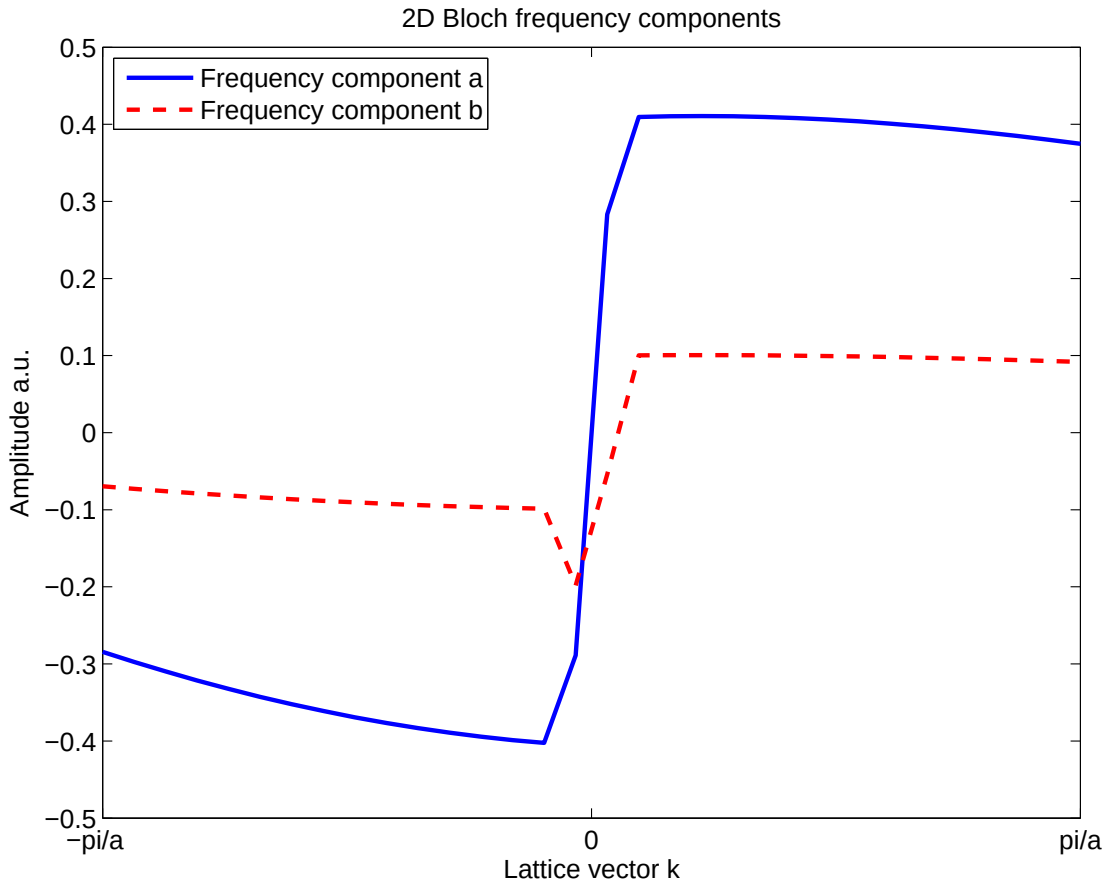

Figure 5.5: Showing two frequency components over the whole range of the k-space in x-direction. The component with the larger amplitude seems to undergo a seemingly smooth transition whilst the transition of the other component is more ambigious.

5.5 Lattice parameters

The calculation of Wannier functions finally gives access to the desired lattice parameters which were defined in Ch. 5.1. The Wannier functions and the corresponding on-site interaction U (see fig. 5.6(a)) and Tunneling J (see fig. 5.6(b)) are calculated for known parameters given in [3]. The results are identical in comparison with [45] which demonstrates that the program code is working properly.

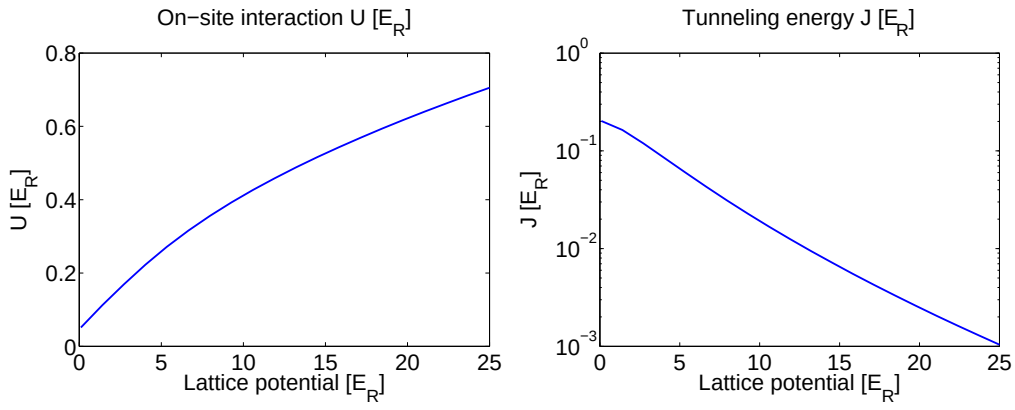

(a) On-site interaction (b) Tunneling

Figure 5.6: Parameters for ^{87}Rb atoms in a 3D optical lattice in relation to the lattice potential depth (in units of E_R, see equation (5.14)). Lattice wavelength $\lambda = 852$nm, lattice spacing $a = \lambda/2$. a) shows the on-site interaction U; b) shows the tunneling matrix element J (in units of E_R). The slight anomaly at the left end of the graph ($0 - 3\mathrm{E_R}$) which is caused by the wavefunction not having sufficiently decayed within the limits of the lattice.

The resolution of the microscope objective lenses used in the system offers a range of suitable lattice spacings from which it is possible to calculate the Laser powers needed to obtain the Mott insulating phase at different lattice spacings. To do this some parameters have to be given ab initio. The wavelength is already specified by the type of laser that will be used for the 2D lattice. In this a frequency doubled Nd:YAG with a wavelength of 532nm will be used. The beam waist should be large to minimise the harmonic confinement of the lattice beams and so is set to $w_{x,0} = 0.5$mm. The vertical confinement is set to $\omega_{trap} = 2\pi \cdot 2.6$kHz a pessimistic estimate for the maximum confinement that can be generated. This confinement is not achieved by the lattice beams themselves but the dipole trap (see ch. 4 and more specifically ch. 4.6.4) but still affects the onsite interaction (see equation (5.5)) as this is determined by a 3D integral. This can be reduced to a 2D integral with an effective coupling strength g_{2D} [45].

$$g_{2D} = 0.98\frac{E_R}{k^2} \tag{5.20}$$

with $k^2 = \nu_{trap} m_{Rb}/\hbar$.

It is now necessary to find out the laser power at the point of phase transition. With a beam waist of $w_{x,0} = 0.5$mm the laser power is derived as shown in fig. 5.7(a). It can be seen that higher lattice spacings require less power with the required power dropping from about 650mW down to 450mW. This coincides with the lattice potential which is shown in fig. 5.7(b). These parameters are given as frequencies which are calculated as $E = h \cdot \nu$. The use of E_R was omitted to avoid confusion as their usually exists a fixed relation between wavelength and lattice spacing, however, this is not the case in these calculations.

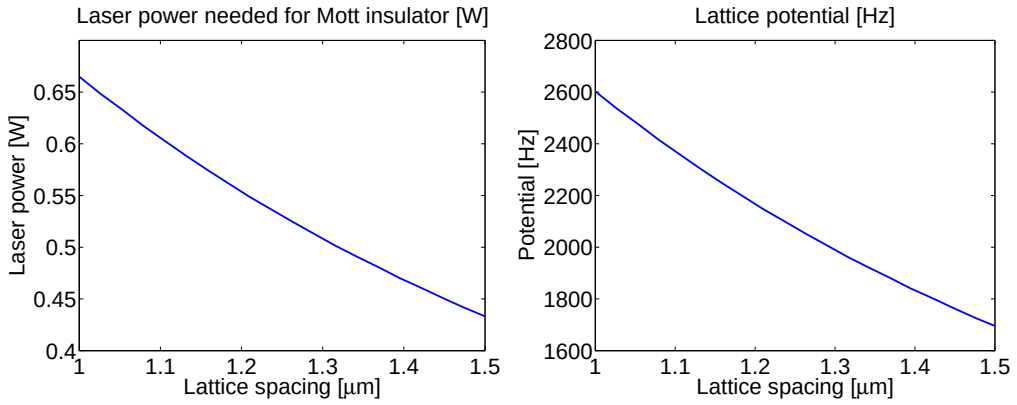

(a) Laser power

(b) Potential depth

Figure 5.7: Optical lattice at the point of transition to a Mott insulating phase for ^{87}Rb in relation to the lattice spacing. Wavelength of lattice forming beams $\lambda = 532$nm and a beam size of $w_0 = 0.5$mm. a) shows the necessary laser power in the lattice forming beams. b) shows the potential depth of the optical lattice.

The laser beams cause a harmonic anti-confinement which reduces from 2.2Hz to 1.8Hz as shown in fig. 5.8(a). This stands in contrast to the trap frequencies of the individual

potential wells in the lattice which range from about 2.4kHz down to 1.3kHz as can be seen in fig. 5.8(b). The difference between the energy scales of the interaction compared to the confinement potential of the enclosing laser beam is three orders of magnitude. This shows that the harmonic confinement of the lattice beams does not interfere with interactions occurring in the lattice.

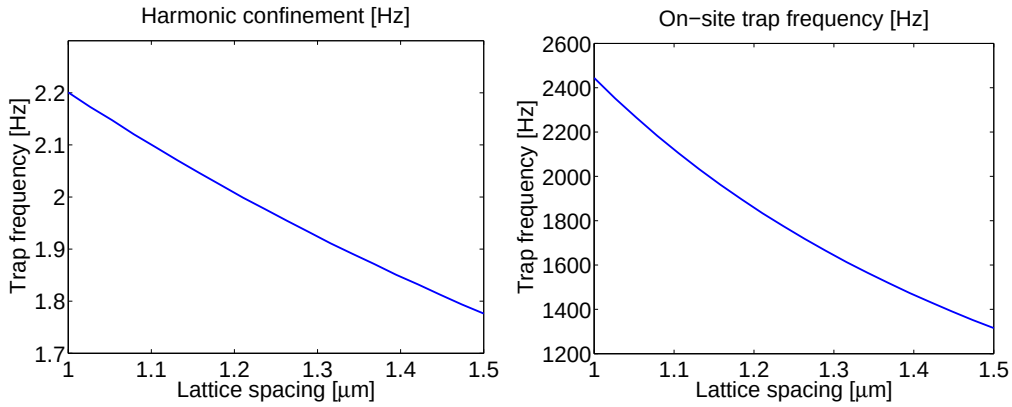

(a) Harmonic confinement

(b) On-site trap frequency

Figure 5.8: Optical lattice at the point of transition to a Mott insulating phase for ^{87}Rb in relation to the lattice spacing. Wavelength of lattice forming beams $\lambda = 532$nm and a beam size of $w_0 = 0.5$mm. a) shows the harmonic confinement caused by the lattice generating beams. b) shows the trap frequency on an individual lattice site. Note that the trap frequency on the lattice sites is much larger than the harmonic confinement making it unlikely that the latter will influence any effects occurring in the lattice.

On the other hand the change of tunnelling and on-site interaction for different lattice spacings are very important and are both diminishing as well (see fig. 5.9(a)). As these values of tunneling and on-site interaction are inverse to the time this gives an estimate about the time scales on which dynamics take place and therefore how long the BEC has to evolve for a desired effect to become visible. This is most important for the tunnelling as this gives a lower limit of approximately $1/t \approx 1/300$ms for the condensate to evolve at $a = 1.5\mu$m. These estimates have to be taken into consideration and balanced as the time for one experiment run is limited by the life time of the condensate. The life time of a

BEC is limited by multiple factors like vacuum, light scattering and three-body collisions and thus cannot be changed easily. It is therefore not desirable to have infinitely slow hopping speeds and respectively as small lattice spacings as possible.

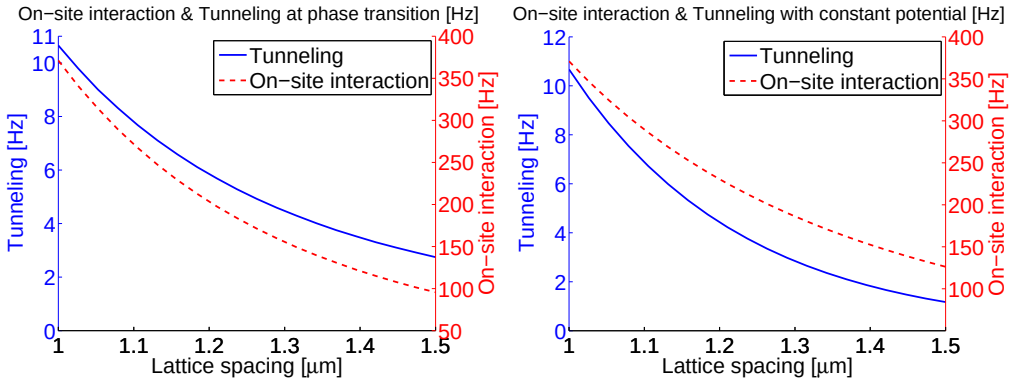

(a) Point of phase transition

(b) Constant potential $V = h \cdot 2.6\text{kHz}$

Figure 5.9: Optical lattice for ^{87}Rb in dependence on the lattice spacing. Wavelength of lattice forming beams $\lambda = 532\text{nm}$ and a beam size of $w_0 = 0.5\text{mm}$. a) shows a semi-logarithmic plot of the on-site interaction U [Hz] and the tunnelling matrix element J [Hz] for an optical lattice at the point of transition to the Mott-insulating phase. b) shows a semi-logarithmic plot of the on-site interaction U [Hz] and the tunnelling matrix element J [Hz] for an optical lattice with a fixed potential depth of $V = h \cdot 2.6\text{kHz}$.

When choosing the lattice spacing for the lattice two things have to be taken into account. It would be beneficial if the lattice constant could be as large as possible to improve the resolution, however, this leads to a weakly interacting regime while the main focus of current research is put on strongly interacting regimes. To illustrate this fig. 5.9(b) shows how the on-site interaction and the tunnelling change at a constant lattice depth of $V = h \cdot 2.6\text{kHz}$ with increasing lattice spacing. The lattice depth seen in fig. 5.7(b) is deep enough for all lattice spacings to generate a Mott insulator. However, the on-site interaction goes down by a factor of four while the tunneling is decreasing by roughly one order of magnitude.

Taking all factors into account it was decided to use lattices with spacings of $1.0 - 1.1\mu\text{m}$. One option to generate these lattices is to use a spatial light modulator (SLM), either a

micro mirror array or a liquid crystal based display, which can be used to shape a laser beam into arbitrary patterns. Due to the dynamic nature of a SLM the lattice spacing can be adjusted if the initial values turn out not to be feasible. Generation of optical lattices with the SLM may fail but it is still possible to generate an optical lattice with the 1550nm lasers used for the dipole trap. Each beam pair intersects with an angle of 90° meaning that both beam pairs have a common beam path (see fig. 5.10). The laser powers needed to reach the Mott insulating phase by this means are very similar to the frequency doubled Nd:YAG (see fig. 5.11).

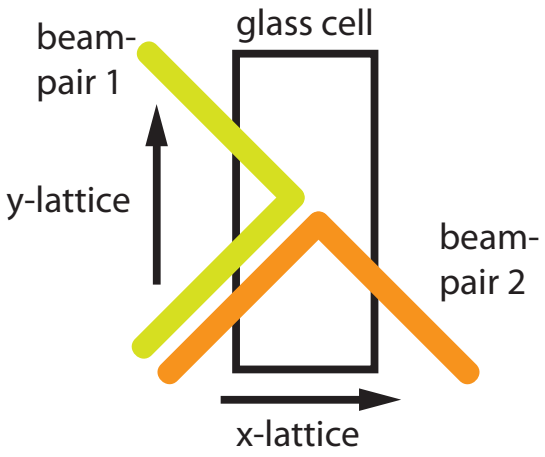

Figure 5.10: Schematic of alternative configuration to generate an optical 2D lattice with a lattice spacing of $a = 1.0 - 1.1\mu$m. Two beam pairs with a wavelength of $\lambda = 1550$nm and an angle of $\phi = 90°$ are superimposed in the glass cell. The beam pairs are perpendicular and have one common beam path. Both beam pairs are detuned to one another by several MHz to avoid any interference between the beam pairs.

To summarise, it was determined that the Mott insulating regime can be reached with an optical lattice with a lattice constant of $a = 1\mu$m at a lattice potential of $V = h \cdot 2.6$kHz. At this point the tunneling energy equates to $J = h \cdot 12$Hz meaning that the evolution times of the experiment have to be larger than $t > 100$ms. The laser power which is needed to achieve the necessary laser intensity equates to $P = 650$mW of $\lambda = 532$nm light.

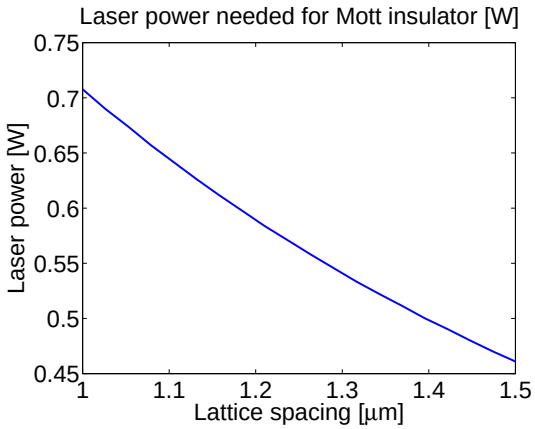

Figure 5.11: Optical lattice at the point of transition to a Mott insulating phase for ^{87}Rb in relation to the lattice spacing. Wavelength of lattice forming beams $\lambda = 1550$nm and a beam size of $w_0 = 0.5$mm. The graph shows the necessary laser power in the lattice forming beams.

Chapter

6 Components of the experiment

In the following the experiment components will be explained which have been designed, set up and characterised in the course of this thesis. I have structured this chapter as follows:

- The computer control (ch. 6.1)
- The buffering electronics used in conjunction with the computer control (see ch. 6.2)
- Introduction of the method used to transport the atoms from the MOT chamber to the science chamber (ch. 6.3)
- The design of the glass cell (6.4)
- The design and characterisation of the dipole laser system (ch. 6.5)

6.1 Computer control

For control of the experiment it was decided to use a system which incorporates very high stability and utilizes latest technological innovations. The hardware and software were designed to achieve high reliability as well as fast timing for the digital and analogue channels. The timing is limited by the hardware being 25ns for the digital and 1μs for the analogue channels. Timings of this accuracy are not used in the average cold atom experiment nor are they necessary for the experiments planned for the equipment under construction. They may, however, prove useful in future, as yet unplanned, experiments and the decision was made to retain these timing limits. The computer control system will be arranged as a network target accessible to all computers on the network and also allows control of TCP/IP devices. The idea behind introducing the computer control as a network device was to increase stability by separating it from the user interacted front end. Connection to the computer control is only activated to update an experiment cycle, which will run repeatedly until it is updated again.
The hardware chosen for the control system will be described and the advantages and disadvantages inherent in the choice of hardware chosen will be discussed. Finally finishing with with timing and noise measurements.

6.1.1 Field programmable gate arrays

For control of the experiment a commercial Field Programmable Gate Array (FPGA) system is used[1]. FPGA systems offer a wide range of advantages. For one the executing processor is placed on the extension computer cards. This eliminates the slow communication of the main computer processor to one of the peripheral cards using comparably slow protocols via the PCI BUS using DMA channels and interrupts. This allows for control of digital channel with 25ns resolution while analogue channels offer 1μs resolution. This enables the FPGA driven computer controls to be adapted to a larger variety of tasks. It

[1] National Instruments NI 7841R [14]

enables a high bandwidth and low latency which in addition to executing commands with a precise timing also allows implementation of feedback loops like PID controllers. This range of possibilities comes, however, at the cost of increased programming effort as each FPGA needs to run it's own software. The FPGA Bitfile which has to be programmed in an assembly type language (HDL) needs to be able to communicate with the main computer to acquire execution data. Thus the tasks which need to be implemented into the computer control divide onto different levels, either onto the computer side or the FPGA side. Furthermore, the computer[2] which runs the FPGA cards runs a Phar Lap real-time operating system (RTOS) which is a slimmed down operating system optimised for reliability and speed.

6.1.2 Program

The program running on the previously described hardware has been programmed using the graphical programming language LabVIEW. It is divided into three layers, the front end program which sends updated sequences to the computer control and can request certain data (e.g. protocols). The main computer control software receives these sequences and processes them into a usable form. It selects a specified amount of time slots which are grouped and transferred to the FPGA cards. The execution on the FPGA is synchronised with the execution of other controlled devices (e.g. network, serial port, usb). The FPGA software receives the data and executes these. In the following discussion these three layers are described beginning with the FPGA level, following with the main computer program and ending with the front end software.

FPGA software

The FPGA is the part of the hardware which controls and activates digital and analogue channels. As such the FPGA Kernel is designed to fulfil two tasks. A communication

[2]National Instruments NI PXI-8108 RT [48]

protocol which requests new data and writes those to the buffer and the other main loop in which the data from the buffer is executed time slot by time slot. Several fail safe measures have been implemented to prevent the buffer from overflowing and all channels are set to safe values in case the buffer runs empty together with synchronisation algorithms to keep multiple FPGA cards synchronised and to resynchronise them if they come out of an empty buffer mode.

FPGA - Communication protocol

The communications protocol is the algorithm where stability and rigidity is more important than in most other parts. The underlying idea includes the main program writing to the 32 Bit first-in-first-out buffer (FIFO) in the FPGA RAM and sending out an interrupt to the FPGA cards and waiting for this interrupt to being acknowledged. The FPGA acknowledges this interrupt and starts reading out the data from the FIFO writing it into the buffer. The FIFO is encoded in such a way that the first number contains the amount of time slots that are being transmitted. This is compared to the amount of free space in the buffer to ensure that the buffer does not overflow. Following that the length of the time slot in units of ticks is transferred and stored accordingly (see fig. 6.1 for a diagram of the data structure) in the appropriate buffer. Afterwards numbers for the digital channels are transferred. Boolean arrays containing the digital channel data have been transformed into the shape of 32 Bit numbers in order to simplify data transfer. The analogue channels give out voltages of -10V to +10V with a nominal resolution of 16 Bit. The voltage is controlled using a signed 16 Bit integer ($-32768 \widehat{=} -10\text{V}$ & $32767 \widehat{=} +10\text{V}$). In addition to this 16 Bit number a 48 Bit number representing the time dependent gradient is also being transmitted. This number consists of 16 integer Bits and 32 decimal Bits. This allows for quick changes to change the channel within two ticks from -10V to +10V and for slow changes to change the analogue channel by the lowest increment over a time of 2^{32} ticks which is the longest a time slot can last. These

$16 + 48 = 64$ Bit are being distributed onto 32 Bit numbers and are recombined in the execution loop. One Bit of the data for the digital channels is encoded to prompt the code to request more data. After reading out all time slots present, the algorithm waits for this prompt to occur and then continues to wait for an interrupt, acknowledges it and starts the read out process all over again.

The first reception of data is important as this data contains the safe values for a buffer empty situation. This data is written into the 0th address of the buffer. Afterwards only addresses beginning from 1 are overwritten because safe values are protected from being overwritten after this initial data exchange. If it is required to change these entries it is only possible by exiting the computer control software and restarting.

All read outs of data are synchronised between multiple FPGA cards in order to avoid race conditions, i.e. the case where the software might crash depending on which FPGA finishes its read-out first.

FPGA - Execution loop

The execution loop starts after the buffer has been filled to a certain level (see fig. 6.2). It first checks whether a time slot has ended and if necessary is being advanced to the next time slot. There is also a check whether the buffer has run empty and a buffer empty situation needs to be enabled, also at the end of a buffer empty situation all FPGA cards are being re-synchronised. Afterwards the appropriate values are read out of the buffer and are sent to a feedback loop which makes the data available with one tick of latency[3]. The delayed digital data is re-transformed into boolean arrays and sent to the digital channels. The analogue data is recombined into a 16 Bit integer starting value and a 48 Bit fixed point gradient and is sent to calculate the latest value for each analogue channel according to $f(t) = a + b \cdot t$

[3]This latency is part of the design of these FPGA boards and cannot be avoided

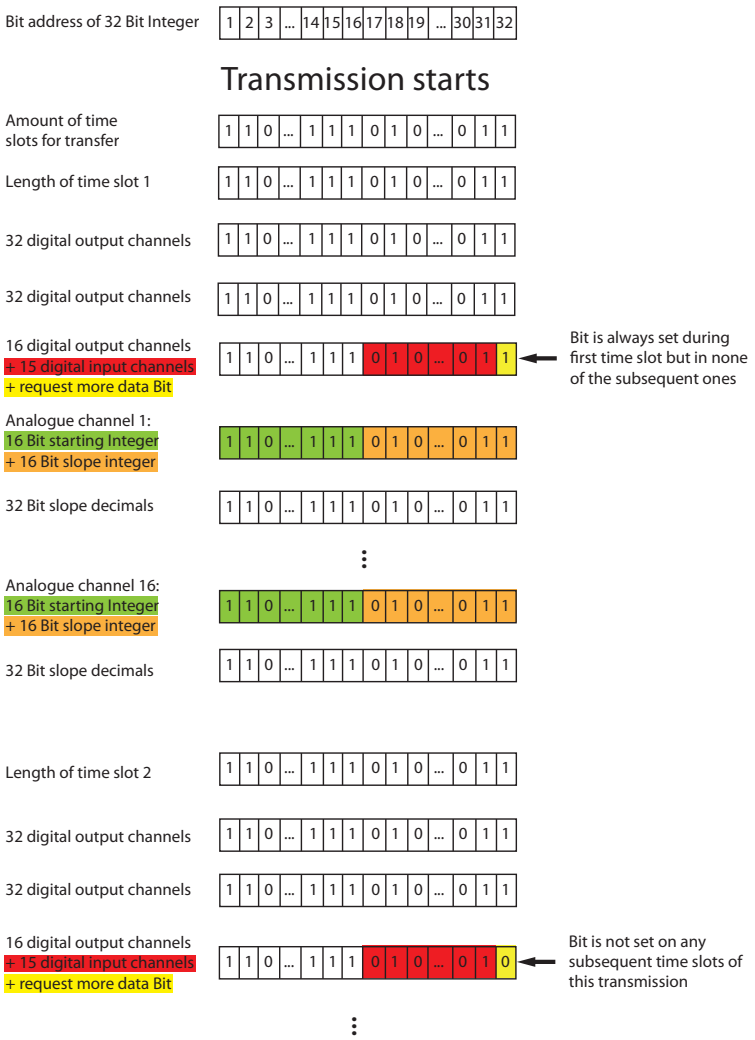

Figure 6.1: The sequence information which needs to be sent to the FPGA has to be encoded in 32 Bit integer numbers. As most information is not natively represented as such, different parts have to be mapped on specific Bits in these numbers. The amount of transferred time slots as well as the time slot lengths are native 32 Bit integers and don't require specific encoding. Each digital channel is represented by one Bit in the digital output channel numbers while the third of these numbers also carries the information if triggering is requested on one of the 15 digital input channels as well as the trigger for the FPGA to request the next data transmission. The analogue numbers consist of a 16 Bit integer for the starting value and a 48 Bit fixed-point number for the slope. The first 16 Bit of the slope are severed and merged with the starting value to form a 32 Bit integer while the remaining part of the slop forms another 32 Bit integer. Without the correct mapping of Bits the transmitted numbers have no meaning which is why they to be properly decoded on the FPGA side after transmission.

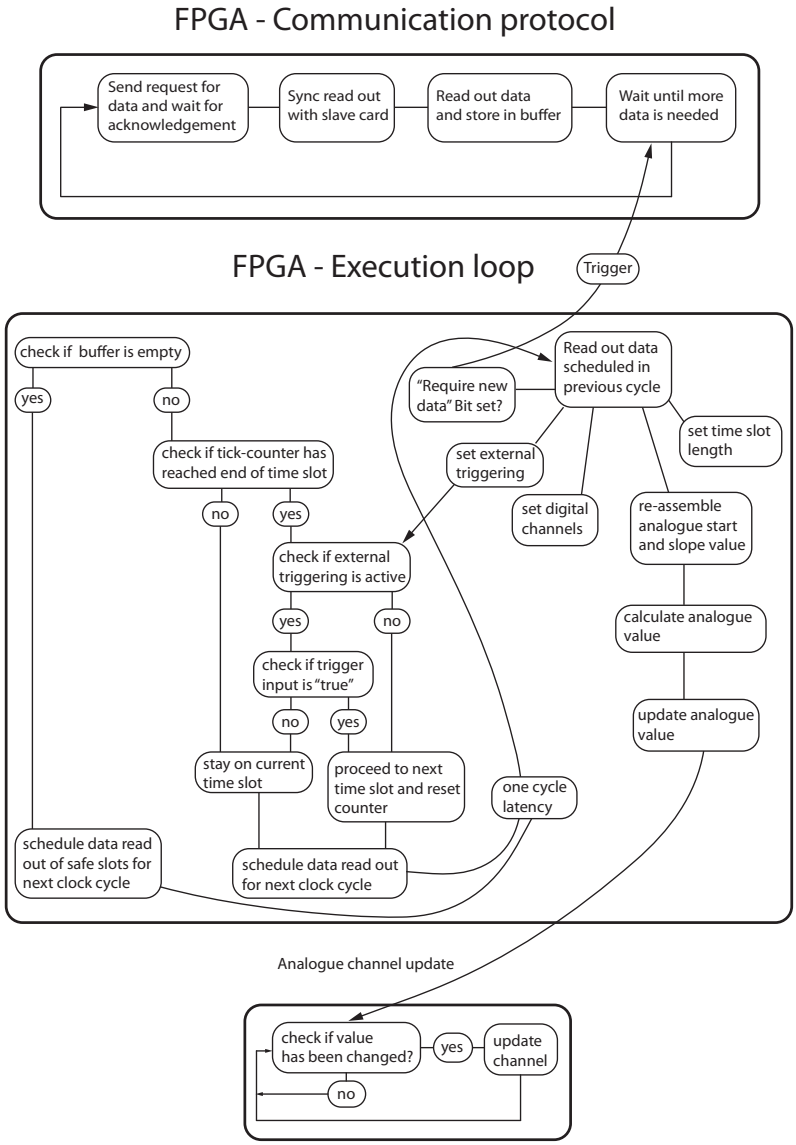

Figure 6.2: The FPGA program consists of two mostly independent loops. At the top is the communication protocol which establishes a connection to the controlling computer to receive those parts of the experiment cycle which are due to be executed. This action is triggered by the occurrence of a specific Bit amongst the digital channel data (see fig. 6.1). The main execution loop has several fail safe checks to ensure that the buffer still has time slots in the queue to be executed and can potentially wait for an external trigger. Following these checks the digital and analogue channels are set to the appropriate values. As the refresh rate of the analogue channels is too slow to be handled by the 40MHz timing of the execution loop the data is transferred to a slower loop which updates the analogue channels accordingly.

Additions and subtractions are not hugely difficult to compute but multiplications and especially divisions are. Multiplications are sent to special nodes in the FPGA which perform this activity. These nodes are very limited and a single multiplication can use up multiple nodes as they are strongly limited in the number of Bits each one can handle. This results in a problem, there are not enough resources to calculate all analogue channels at once. The execution loop runs at a clock speed of 40MHz whilst the analogue channels have an update rate of 1MHz, however, it is not necessary to compute all analogue channels every 25ns. To accommodate this within the limitations of the control hardware it was decided to split up the analogue channels and compute alternate even and odd numbered channels in subsequent ticks. Every two ticks the updated values are made available to the analogue channels, however, the analogue channel update is outside of the single cycle timed loop as the slow repetition rate does not allow for these to be placed into the 40MHz loop. The latest values are compared to the previous value and, if different, the analogue channel updated accordingly.

The main execution loop also contains the possibility to externally trigger the computer control, at the end of a time slot it is checked and if external triggering is required on specific digital lines the advance to the next time slot is delayed until the trigger is received. Afterwards the signal is synchronised with all installed FPGA cards and the code progresses to the next time slot.

PXI software

The PXI computer administers and processes all data as well as directly controlling all devices running on the virtual-standard-architectur (VISA). The main purpose of the PXI computer is it to feed the FPGAs with data and execute commands for VISA-devices synchronised with the FPGA. The main program on the control computer can thus be divided into three parts. Firstly, it needs to administer TCP/IP connections which send commands to the program. Secondly, it needs to process experiment sequences

into a more machine friendly form and make sure that the FPGAs are provided with sufficient amounts of data. Thirdly all other devices which are controlled and fall under the category of VISA devices need to be served and synchronised with the FPGAs.

PXI - Network protocol

The network protocol is based on a commonly available TCP/IP library[4]. Each string which is received by the protocol contains a short identifier string and then the actual message string. This message string is an arbitrary data type which is encoded as a string using the "flatten to string" function. In order to properly decode the string the original data structure must be known. The identifier is used to determine the purpose of the following string and loads the appropriate case to process the string. Using this technique it is possible to create a simple and versatile algorithm which can be easily expanded. The main functions which are currently implemented are:

- Initialisation (needs to run in order to start the program. Contains information about safe values which are being used in case the buffer runs empty)
- Updating sequence including all calculation intensive pre-processing
- Request whether the end of a cycle is coming in less than a second
- Updating counter delays (e.g. countering the mechanical delay of shutters)
- Closing the program
- Requesting protocol file (xml-format)

The initialisation takes the boolean array with safe values for the digital channels and the 16 Bit integer array with safe values for the analogue channels and generates several time slots of these. This initiates the first data transfer to the FPGAs and as described previously the very first slot cannot thereafter be altered.

[4]Simple Messaging Reference Library (STM) by National Instruments

When the sequence is updated most of the processing of the experiment cycle is done in this part. At first counter delays are introduced. The data in analogue channels initially consists of a starting value and a boolean which establishes whether a ramp to the value of the following time slot is supposed to be executed. The gradient is calculated and is carried forward in place of the previous boolean (see fig. 6.3).

In order to prevent accidental "time outs" by transmitting a very long time slot these are cut into smaller time slots of a maximum of half a second. If the sequence would be executed unaltered the computer control would freeze while waiting for this long time slot to finish making the whole control unresponsive. When running the same sequence cut into smaller sections the computer control remains responsive and can be aborted if desired to avoid having to wait for the completion of the sequence.

PXI - main execution loop

The main execution starts with an initialisation bit which is put on hold at the beginning in order to wait for the safe values as previously described. Once these arrive five slots are generated and transferred to the FPGAs which includes a slot in the middle which will cause the next request for data. Following that the buffer for the continuous loop is being initialised. The main loop starts by sending an interrupt to the master FPGA whose acknowledgement signifies the request for additional data. At the same time a time stamp is taken, which coarsely identifies which time slot the FPGA is currently executing. This time stamp is used to synchronise commands issued via the virtual-instrument-standard-architecture (VISA) to the FPGAs which is described in more detail later. In parallel with this a data set is generated consisting of time slots filling roughly half a second. The first slot contains the encoded Bit which causes more data to be requested. The VISA commands are amended with a tick count, which contains how many ticks after the beginning of the aforementioned data set they need to be executed. Afterwards the data is sent to the FPGAs and the routine is repeated (see fig. 6.3).

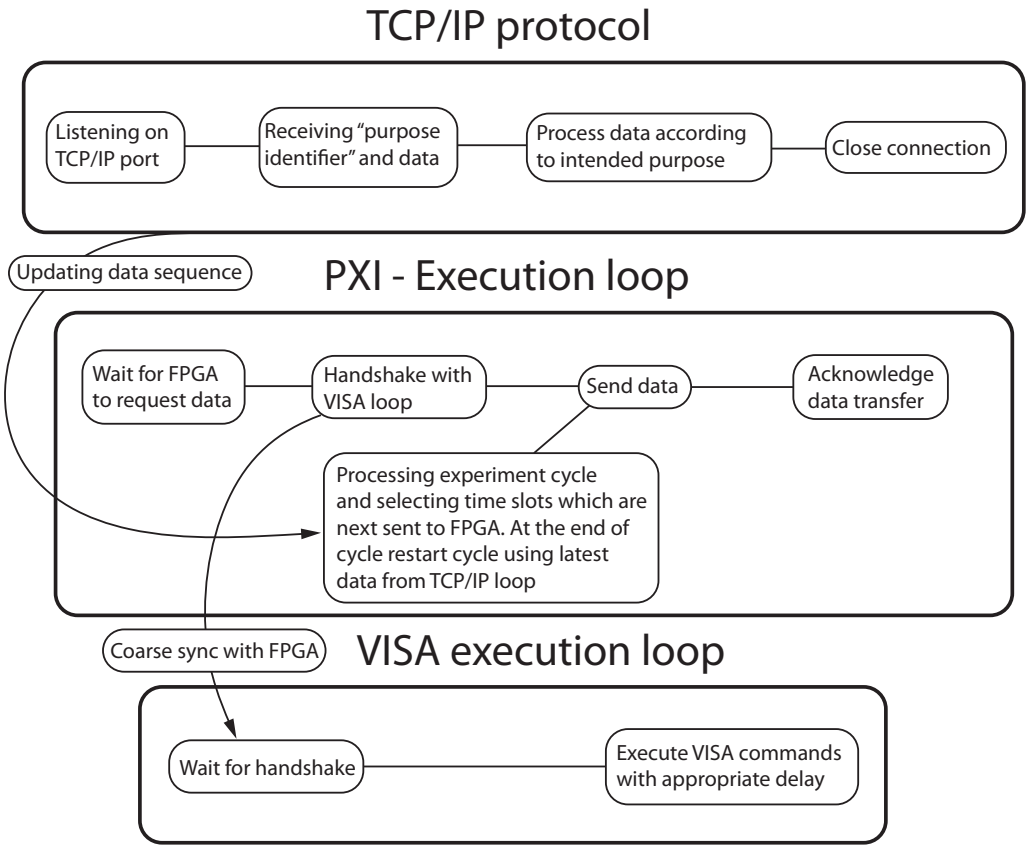

Figure 6.3: The program running on the PXI-computer consists of three mostly independent loops. The network protocol waits for external computers to build up a connection. Once the connection is established it receives the data and processes those accordingly before closing the connection and waiting again for a new connection. The processing depends on the purpose of the data connection. E.g. if a new sequence is transmitted it pre-processes the data by applying counter-delays to account for the time to open and close shutters as well as transforming the data structure into a less user- and more machine-friendly form. The main execution loop waits for the FPGA to request a data transmission (see fig. 6.2). Following which the loop coarsely synchronises with the VISA execution loop and transmits a number of time slots to the FPGA which have been prepared while the loop was waiting for the initial trigger. After synchronising with the main execution loop the VISA (virtual instrument standard architecture) execution loop starts to send out any queued commands to the respective devices keeping a coarse synchronisation to the FPGA.

PXI - VISA execution

All commands issued to GPIB, serial-port, USB and TCP/IP devices are administered by the virtual-instrument-standard-architecture (VISA). The VISA execution runs in parallel to the other processes and starts by waiting for data to be executed. When this data is provided by the main execution loop the data transfer is acknowledged with a handshake. Data consists of the VISA addresses and corresponding commands. These commands are encoded with a delay which tells how long after the FPGA requested more data the VISA commands needs to be sent out. The commands are sorted by delay and a loop is working these off. It is continuously checking that the delay has passed by comparing the actual time to the time stamp created after the FPGA acknowledged the interrupt (see previous chapter). If the required delay has passed a connection to the device is established and the command is sent out. With commands to different devices which are required to be sent at the same time this causes a delay for the subsequent commands as they need to be completed one at a time. This cannot be parallelised as the used ports need to be blocked and cannot, therefore, be used for additional data transfers at the same time (see fig. 6.3).

Front end

It was decided to keep the front end as flexible as possible. Instead of designing a complete control software a new meta language was developed. With the functions created, it was possible to program sequence modules controlling the different phases. It was generally thought that it would be an impossible task to create a control which is suitable for all situations. Creating a meta language leaves it to the user to program modules which are optimal. This requires a basic knowledge in programming.

The modules which have been designed include:

- start real-time (RT) Host. The main program is being started on the control system.
- initialisation of RT host. The safe values are being transmitted which causes the main program to start to execute sequences.
- stop RT host. The main program is stopped. (These three commands are not used in the design of sequences)
- Initialisation of a sequence. VISA names are being defined here also all arrays are generated correctly sized.
- time slot. This generates a new time slot with the time being input in either tick length or seconds.
- digital channels. A list of digital channels can be put in and changed to either true or false.
- analogue channels. An analogue channel can be set to a starting value and it can establish whether a ramp is to be executed to the value of the next time slot.
- VISA command. A string command can be set for any defined channel.
- transmit sequence. The sequence is sent via TCP/IP to the control system. It will be executed periodically after the present sequence has ended.

See fig. 6.4 for part of a typical implementation of a front end.

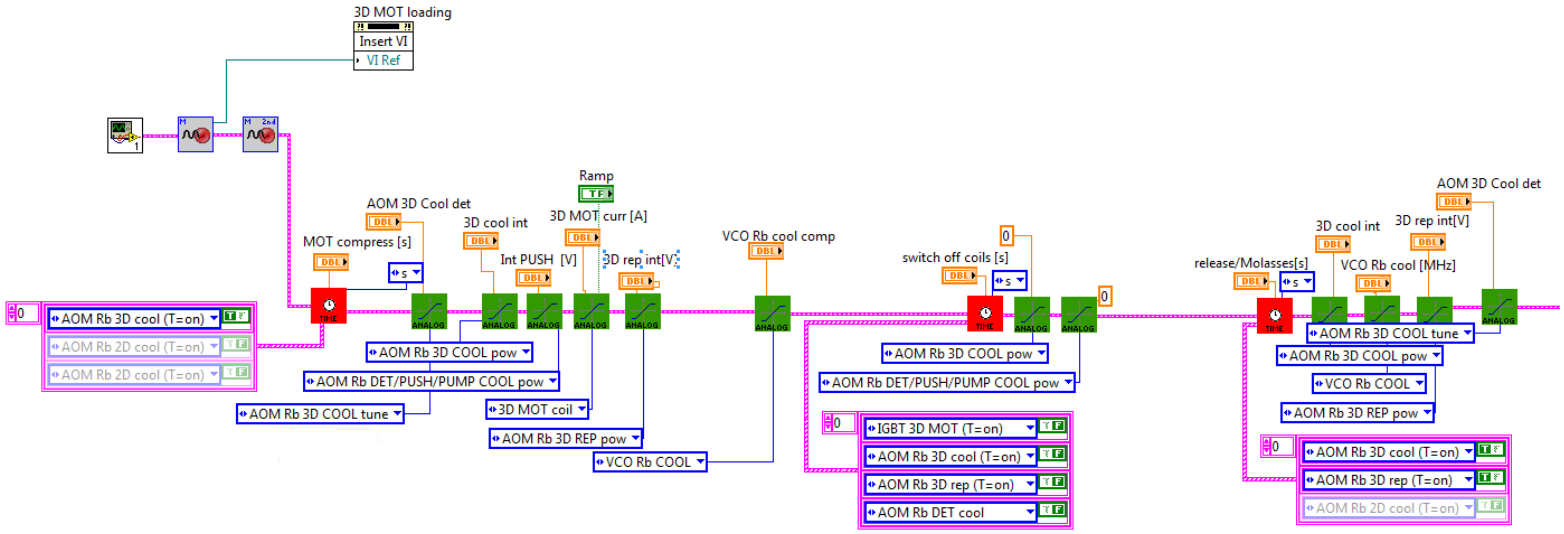

Figure 6.4: Typical part of a front end implementation. At the left hand side the box with the "1" initialises the experiment sequence. The following two grey boxes represent two fully integrated modules for loading the magneto-optical trap. The following red box generates a new time slot which also sets the digital channels for that time slot. The analogue channels are set to their appropriate values by the following green boxes. This is again followed by a red box which generates the succeeding time slot. This pattern is repeated for every part of the experiment cycle and is at the end tranferred to the PXI-computer via TCP/IP (see fig. 6.3)

Port to other hardware

It is possible to successfully port the code to a fully integrated controller/FPGA board. This board is much less powerful than the original hardware that this program was designed to use. The main controller uses a 400MHz single core processor compared to a 2GHz dual core unit. As multi threading is not effective on a single core and this processor does not support hyper-threading this can cause problems when the board is executing sequences which provide a high bandwidth of data. The process that prepares the data to be transferred to the FPGAs causes a CPU load of close to 100% which interferes with the process which runs the TCP/IP service. This can cause the controller to have frequent buffer low situations and for the whole board to become unresponsive to TCP/IP control. The code, however, has now been further adapted to reduce recurrent processor load when one time manipulation of data was sufficient. The integrated board uses a "Spartan 2" FPGA while the PXI-system used in the experiment presented in this thesis makes use of a "Virtex 5" FPGA. The performance difference between the single-board FPGA and the PXI FPGA which the program was designed for quickly became apparant. The clock speed of 40MHz was not possible to achieve and needed to be reduced to 10MHz. The placement of the multiplier chips on the "Spartan 2", is such, that some of them are blocked when look up tables (LUT) and block RAM is being used. With 20 analogue channels to be used the interlaced calculation of analogue channels had to be changed to evaluate only every 7 ticks as only three channels were possible to run in parallel even though the accuracy of the gradient has been greatly reduced. This is, however, in contrast to a refresh rate of 40μs compared to 1μs of the previous system which makes this a viable option.

6.1.3 Summary

A reliable computer control was designed with a timing of 25ns for the digital and 1μs for the analogue channels. The software also allows for various external devices to be

controlled including GPIB, serial-port, USB and TCP/IP controlled devices. The control software has proven to be portable to other systems which offer similar hardware even if this is much less powerful than the hardware incorporated in this set up.

6.2 Electronic buffering hardware

Between the computer control and the experiment buffer electronics are installed which will be described and explained in this chapter. The buffer electronics fulfils two purposes. Firstly, the capacitative load the digital channels can drive is 20pF which is very low and would already be outranged by a BNC cable with a length of half a metre. If a larger capacity is installed this will result in reduced timing according to $C = I_{max} \cdot t/V_{max}$ with $I_{max} = 4\text{mA}$ and $V_{max} = 3.3\text{V}$. In contrast the buffering electronics are able to drive any capacitative load as well as 50Ω impedance matched resistors directly without a reduction in timing.

The second, and more important reason, for the buffer electronics is to completely decouple the experiment from the computer control to avoid unnecessary ground loops as well as protecting the FPGA-Hardware from any kind of overvoltages or short circuits. The main frequency ranges in which ground loops need to be suppressed by the buffering electronics are low frequencies up to several kHz, most importantly the 50Hz mains frequency. Two different circuits are used, one for the digital channels and one for the analogue channels. The buffer electronics are driven by power supplies with a floating ground. The ground reference is adjusted to match outgoing and returning currents in order to remove ground loops. Due to the sheer amount of digital channels (192 possible channels) it is impractical to attach one of those power supplies to each of the channels. Instead we chose to divide the channels in groups of eight and attach one floating power supply to each of those groups.

As the computer control only offers 16 analogue channels we attached a floating power supply to each of those. In the following chapters the principle of the floating power supplies as well as the buffering electronics will be explained first for the digital channels and then for the analogue channels.

6.2.1 Digital electronics

Floating power supply - Digital

The aforementioned floating power supply is a 5V power supply driven with 9V, nominally allowing for the ground to be adjusted by ±2V. As a voltage drop occurs over the transistors this is however reduced. The circuit diagram can be seen in fig. 6.5[5].
The circuit is supplied with 9V at PAD3 and 4. A differential amplifier[6] compares the currents going through high precision resistors R1 and 2. The differential amplifier is guarded by buffering capacitors C1 to C4, while the resistors R5 and R6 form a potential divider which puts the ground set point to +2V. The Zener diode D1 causes the 5V voltage drop for the output while the output of the differential amplifier controls the bases of the transistors Q1 and Q2 and thereby controls the current. A change of the output of the differential amplifier will reduce the current through the one transistor and increase the current through the other until the currents are equal. The output and return currents are guarded by a choke L1 which balances the input/output currents for higher frequencies.

Digital linedriver

The circuit diagram of the buffering electronics can be seen in fig. 6.6. For simplicity buffering capacitors are not displayed. The digital signals are transmitted from the computer control to the buffer electronics via ribbon cables and enter the circuit at

[5]US patent 5103109 [49]
[6]Burr-Brown INA154 differential amplifier [50]

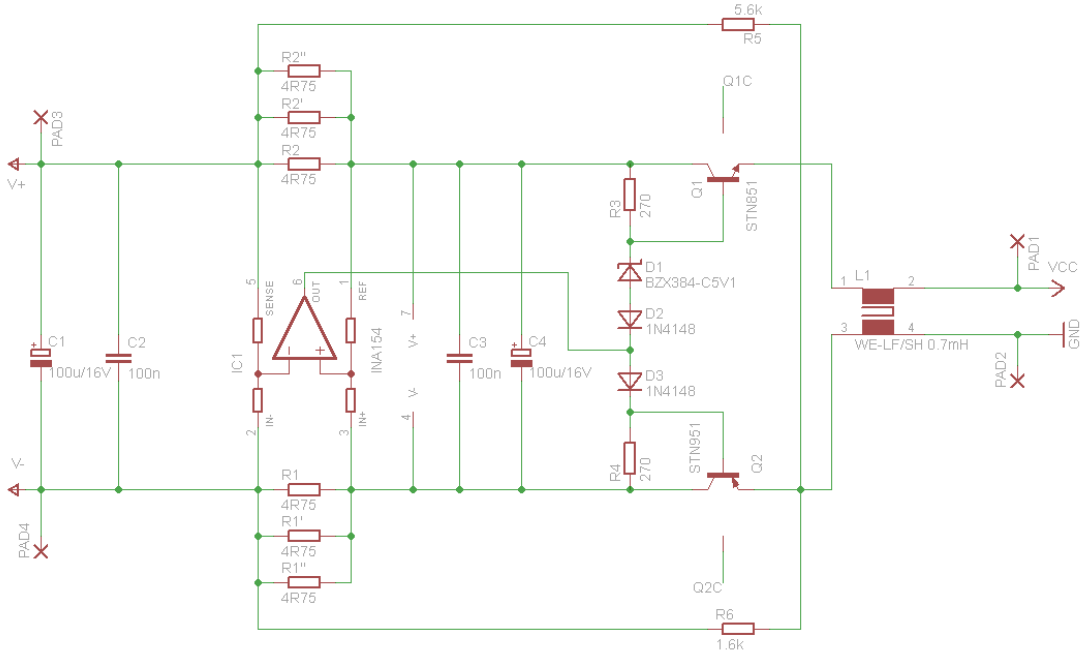

Figure 6.5: Circuit diagram of the floating power supply for the buffer electronics for the digital channels reproduced from [49]. The power is supplied at the left hand side. IC1 compares the ingoing and outgoing current and adjusts the output accordingly which in effect adjusts the ground level by controlling the current through the transistors Q1 and Q2. The ground set point is set by the voltage divider formed by R5 and R6. While changes in the ground level can be compensated this way for lower frequencies a choke L1 is included to include control for higher frequencies.

connector PL1. The chips IC2 and IC3 provide the insulation of the computer and experiment side[7] while the computer side is driven by a 5V power supply which is integrated on the FPGA cards. The experiment side is powered by the power supply described in the previous chapter. The signals are forwarded from the insulation chips to the digital linedrivers[8] IC1 which buffers the signal and gives it out impedance matched with a 47Ω resistor to the BNC connectors J1 to J8.

The digital isolator being used is based on giant magnetoresistive technology with a specified bandwidth of 110Mbps compared to conventional high speed optocouplers which

[7] NVE Corporation IL715 digital isolator [51]
[8] Texas Instruments SN74BCT digital buffer [52]

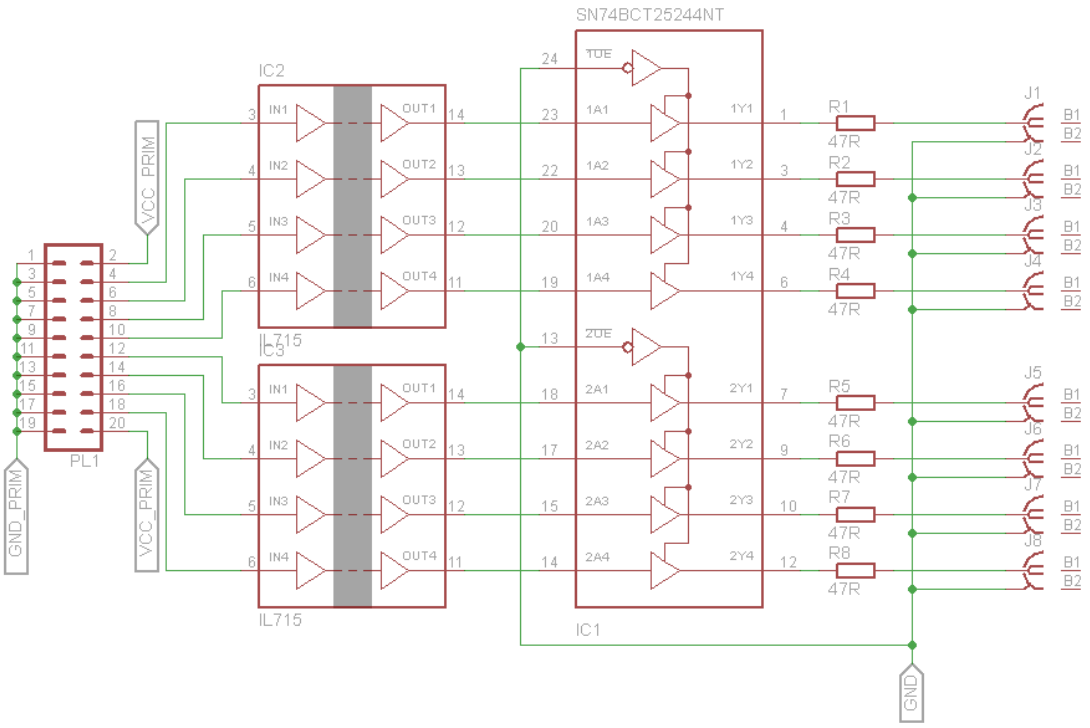

Figure 6.6: Circuit diagram of the buffer electronics for the digital channels. The signal enter the circuit on the left hand side. IC2 and IC3 provide insulation from the computer control to the experiment side while IC1 buffers the signal allowing for a higher signal load.

offer bandwidths of up to 25 Mbps. The digital linedriver used offers an output current of up to 80mA with rise times of $1 - 5.5$ns and fall times of $2 - 6$ns

Digital linedriver - measurement

In the following the results of measurements undertaken to characterize the digital buffering electronics will be presented. The channels on which measurements have been performed were randomly chosen. These include measurements of the rise- and fall times, jitter between channels, latency induced by the electronics, measurement of the load dependence of the output voltage and the ground insulation.
At first the rise and fall-times are characterised. Fig. 6.7(a) shows the rising slope of two different digital channels while 6.7(b) shows the falling slope.

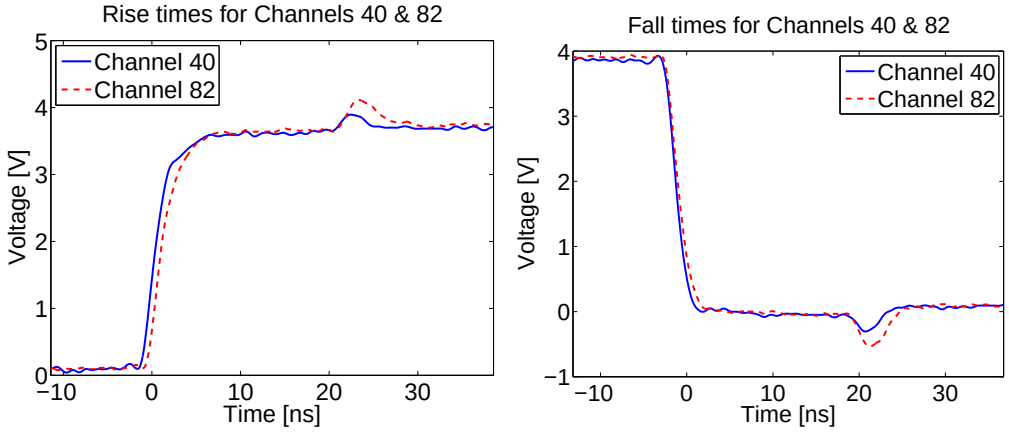

(a) Rising slope (b) Falling slope

Figure 6.7: These graphs show the buffered outputs of two different digital channels from two different FPGAs (channel 40: FPGA 1 & channel 82: FPGA 2). a) shows the rising slope while b) shows the falling slope. Note the artefact around 20-25ns on both graphs. This is a reflection caused by the MΩ input of the oscilloscope. It is consistent with a round trip along the 2m BNC cable.

The rise time as shown in fig. 6.7(a) is 5.25ns (10% to 90%) and the fall time as shown in fig. 6.7(b) is 2.4ns (90% to 10%). This is well within the margins of the specifications of the linedriver which states a maxmimum for the rising slope of 5.5ns and 6ns for the

falling slope. The dips at $20 - 25$ns in fig. 6.7(a) as well as the dips at 20ns in fig. 6.7(b) are caused by reflections of the oscilliscope input and delayed by the 2m BNC cable used for the measurement. This is consistent with an expected signal propagation speed of $2 \cdot 10^8$m/s inside the BNC cable. If the oscilliscope is set to 50Ω input impedance these dips vanish completely which demonstrates that the buffering electronics are well matched to an impedance of 50Ω.

Observe that the two channels are slightly out of synchronisation with a delay of 0.6ns. One factor is that the FPGA introduces a specified jitter of 350ps [14] when the 40MHz is phase locked to the 10MHz clock of the PXI Bus. This lock to the Bus clock is necessary to synchronise the different FPGA boards. Another reason becomes apparent when comparing the direct outputs of the digital channels without the linedriver electronics compared to the same measurement with the linedriver electronics. In fig. 6.8(a) & 6.8(b) you can see the non-buffered rising slope of the buffered output of channel 39 in comparison to the unbuffered output of channel 80.

The direct output shows a much slower slope which is expected with a specified rise and fall time of 12.5ns. It can also be seen that the output is much less clean and defined than the buffered version which happens as the outputs are not impedance matched on the FPGA board. Various RF reflections will deform the signal leading to jitters in the timing when the inputs of the isolation switches breach the thresholds for high and low values. The isolation switches themselves are also causing a jitter between different channels as the thresholds vary from chip to chip which is specified to a maximum of 2ns by the data sheet [51]. The falling slopes show the same behaviour as can be seen in fig. 6.9(a) & 6.9(b).

From both measurements it can also be seen that the buffering electronics causes a latency of 10ns for the rising slope and 9.5ns for the falling slope.

The digital linedrivers are specified to support an output current of up to 80mA per channel. The next measurement is thus determining the level of the output voltage in

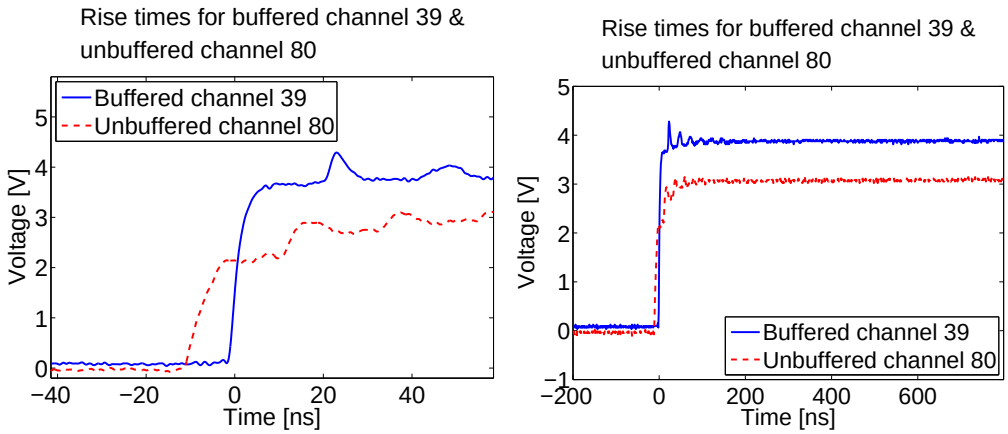

(a) Rising 10ns

(b) Rising 100ns

Figure 6.8: These graphs show one buffered and one unbuffered output of two different digital channels from two different FPGAs (channel 39: FPGA 1 & channel 80: FPGA 2). a) shows the rising slope on a short time scale emphasizing how undefined the unbuffered slope is compared to the buffered equivalent. This also shows the latency of the buffering electronics. b) shows the rising slope on a longer time scale. The constant reflections of the oscilloscope can be seen as a ripple on the signal of the unbuffered output. The buffered output shows one overshoot and afterwards fully absorbs the reflections.

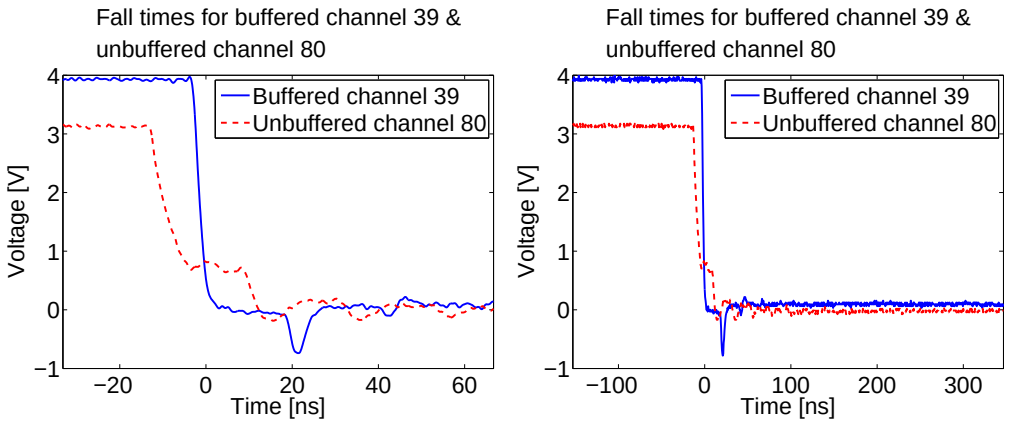

(a) Falling 10ns

(b) Falling 10ns

Figure 6.9: These graphs show one buffered and one unbuffered output of two different digital channels from two different FPGAs (channel 39: FPGA 1 & channel 80: FPGA 2). a) shows the falling slope on a short time scale same as in fig. 6.8(a). Observe how deformed the unbuffered slope is compared to the buffered equivalent. Observe also the latency of the buffering electronics. b) shows the falling slope on a longer time scale. As in 6.8(b) observe the constant reflections of the oscilloscope as a ripple on the signal of the unbuffered output while the buffered output only shows one overshoot and afterwards fully absorbs the reflections.

dependence on the current as can be seen in fig. 6.10 which is strictly linear as would be expected from the linearly increasing voltage drop over the resistors which are in series with the digital linedriver (see fig. 6.6). The impedance of the digital connectors is gained of the fitting parameters of the slope and is $51\Omega - 52\Omega$. Together with the 47Ω in-line resistance this gives an impedance of the line driver of $4 - 5\Omega$ which is well in acceptable limits. There is also a slight difference in the output voltage between different channels which is well within the specifications of the linedriver.

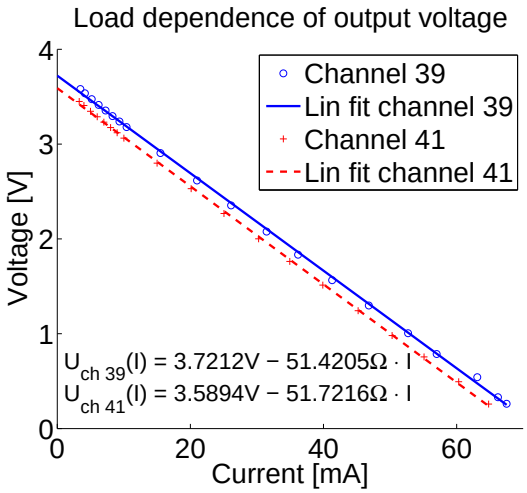

Figure 6.10: This graph shows the output voltage of two digital channels in relation to the current and thus shows the load dependence of the channels. Observe a strictly linear behaviour which is used to determine the impedance of $51\Omega - 52\Omega$.

Finally the effectiveness of the floating power supplies needs to be tested to determine how well the ground-insulation works. For that the impedance of the BNC grounds needs to be measured. We use an impedance matched frequency source as well as an impedance matched detector. Both output and input are connected whilst a BNC "T-piece" is between them whose signal is connected to the device, whose impedance is to be measured. This is represented by the circuit diagram in fig. 6.11.

For the output and input voltages we get:

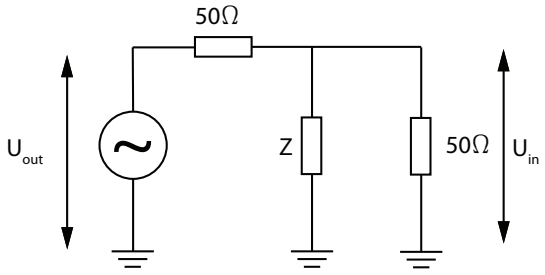

Figure 6.11: Circuit diagram for impedance measurement. The output voltage drops off over the 50Ω output resistor at the top in series with Z and the input 50Ω on the right hand side which are parallel to each other. The input voltage is measured over the 50Ω resistor on the right hand side which means that the measured voltage is the voltage that drops off over the 50Ω input resistor parallel to Z.

$$U_{out} = (50\Omega + 50\Omega \parallel Z) \cdot I \tag{6.1}$$

$$U_{in} = 50\Omega \parallel Z \cdot I$$

where $50\Omega \parallel Z$:

$$\frac{1}{50\Omega \parallel Z} = \frac{1}{50\Omega} + \frac{1}{Z} \tag{6.2}$$

and further we divide U_{out} and U_{in}:

$$\frac{U_{in}}{U_{out}} = \frac{50\Omega \parallel Z}{50\Omega + 50\Omega \parallel Z} \tag{6.3}$$

for the trivial case of $Z = \infty$, $\frac{U_{in}}{U_{out}} = \frac{1}{2}$. equation (6.3) can be rearranged for Z:

$$Z = \frac{50\Omega}{\frac{U_{out}}{U_{in}} - 2} \tag{6.4}$$

We calibrate the measurement technique by attaching a 50Ω resistor and afterwards a 100pF resistor instead of Z as can be seen in fig. 6.12(a) and 6.12(b).

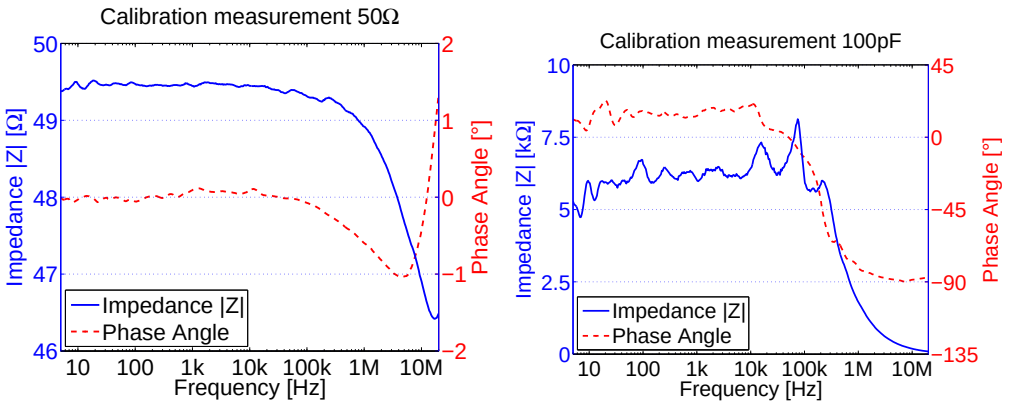

(a) Calibration R = 50Ω

(b) Calibration C = 100pF

Figure 6.12: Impedance calibration measurements. Using the circuit from fig. 6.11 the impedance Z has been exchanged with a) a 50Ω resistor and b) a 100pF capacitor. The graphs show the impedance of those measurements and the phase. Observe that (a) shows a measurement consistent with that of a 50Ω resistor and (b) shows a very high resistance up to a certain frequency at which the phase changes and the resistance falls. This also consistent with the measurement of a capacitor.

The 50Ω measurement shows a resistance of 49.5Ω which is within the tolerance levels. At 0.5MHz the effect of the capacitor is seen as a small negative phase shift, following which the resistance drops by 3Ω until at 20MHz the phase changes to a positive shift. This behaviour has to be considered when interpreting ensuing results.

The 100pF measurement shows a very high resistance of $|Z| > 5\text{k}\Omega$ up to a frequency of 200kHz at which point, the capacitor starts to dominate the measurement as can be seen by the negative phase shift. The fluctuations for low frequencies are caused by noise on the output, in comparison to the output-calibration (U_{out}) which was measured in a

separate measurement. From a frequency of 1MHz onwards the phase shift stays mostly constant at $-90°$ coincident with a decreasing resistance which tends to zero at 20MHz.

Fig 6.13 illustrates the measurement for the impedance of the digital connectors.

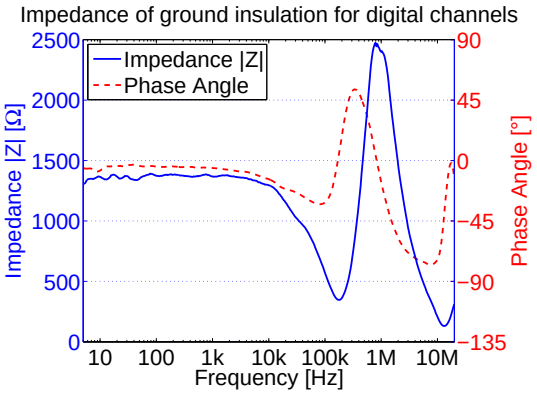

Figure 6.13: Using the circuit from fig. 6.11 the graph shows the impedance measurement of the digital connectors. Observe that the resistance stays high up to a frequency of 10kHz then falls rapidly with increasing frequency followed by a large peak in resistance which is caused by the choke (see fig. 6.5)

Up to a frequency of 20kHz we observed a high impedance which decreased due to the capacitative effects (minimum impedance obtained at 300Ω at 200kHz). An inductive resonance phenomenon can be observed in the phase at $100 - 200$kHz which is followed by a peak in the impedance. This behaviour is caused by a resonance in the choke (see fig. 6.5). Subsequently the phase drops to negative values and the impedance decreases again. This illustrates that the ground insulation of the digital channels works well up to 10MHz. We expect most interference to come from the mains frequency of 50Hz and other low frequencies, i.e. kHz noise from switch-mode-power-supplies, from which we conclude that the digital channels are well insulated against ground loops.

6.2.2 Analogue electronics

Floating power supply - Analogue

The floating power supply for the analogue buffer electronics is a ±18V power supply driven with 36V. The 18V of the floating power supply are applied to 15V voltage regulators which have an additional voltage drop off of 2.5V. This means that the voltage regulators need a minimum supply voltage of 17.5V to allow for a change in the ground level of ±0.5V. The circuit diagram can be seen in fig. 6.14.

6.14

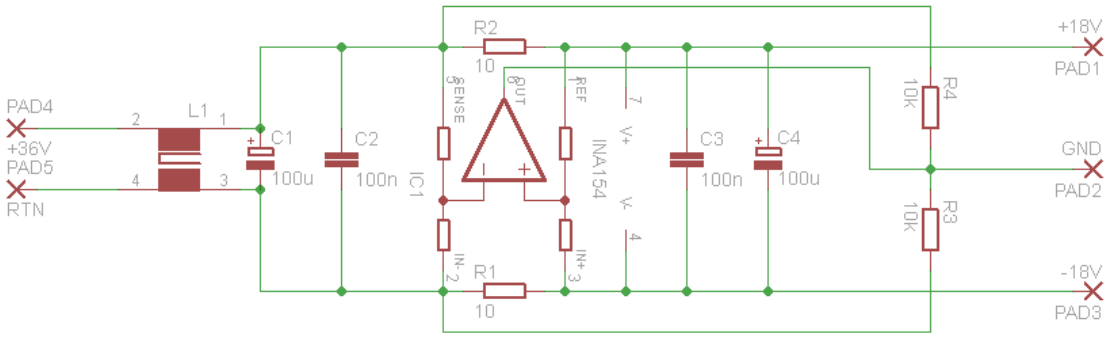

Figure 6.14: Circuit diagram of the floating power supply for the buffer electronics for the analogue channels. The power is supplied at the left hand side. IC1 compares the ingoing and outgoing currents and adjusts the ground level accordingly which is set in the middle of a voltage divider (R3 & R4). The choke L1 filters high frequency changes of the ground loop.

The circuit is supplied with 36V at PAD4 and PAD5. The input and return currents are guarded by a choke L1. A differential amplifier IC1 compares the currents going through high precision resistors R1 and R2 with V_- on pin 4 and V_+ on pin 7 giving the supply for the amplifier which is guarded by buffering capacitors C1 to C4, while the resistors R3 and R4 form a potential divider which puts the ground set point to +18V. For a load between PAD1 and PAD2 the current flows from the power supply through R1 to

the differential amplifier[9] supply V_{-}. From the output of the amplifier the current flows to PAD2 and through the load returning at PAD1 going through R2 back to the power supply. The output of the differential amplifier shifts the potential level of the ground at PAD2 in the attempt to level the currents through the high precision resistors.

Analogue buffer

The circuit diagram of the buffering electronics is illustrated in fig. 6.15. The floating power supply of the previous chapter connects to PAD1 to PAD3. The adjacent voltage regulators generate the supply voltage for the differential amplifier IC1 and buffering operational amplifier IC2. The supply voltage is filtered by capacitors C1 to C6.

The analogue signal enters the buffering part of the circuit at jumpers J2-1 and J2-2. The voltage level of the input is sensed by the differential amplifier IC1[10] which forwards this level to a buffering high speed operational amplifier IC2[11] and is eventually output at BNC connector J1. The high power operational amplifier is able to drive capacitive and resistive loads directly without a decrease in timing and also reduces the offset voltage. The arrangement of differential and buffer amplifier however introduces oscillations with high capacitative loads which needs to be taken into consideration.

Analogue buffer - measurement

The results of measurements undertaken to characterise the analogue buffering electronics is given below. These include measurements of the offset, load dependence of the output, noise measurements, measurement of the rise times and the ground insulation.

Due to varying offset voltages of the differential amplifier and buffering operational amplifier in fig. 6.15 we expect each channel to carry a characteristic offset. Measurements

[9] Burr-Brown INA154 differential amplifier [50]
[10] Burr-Brown INA154 differential amplifier [50]
[11] Analog Devices AD817 high speed amplifer [53]

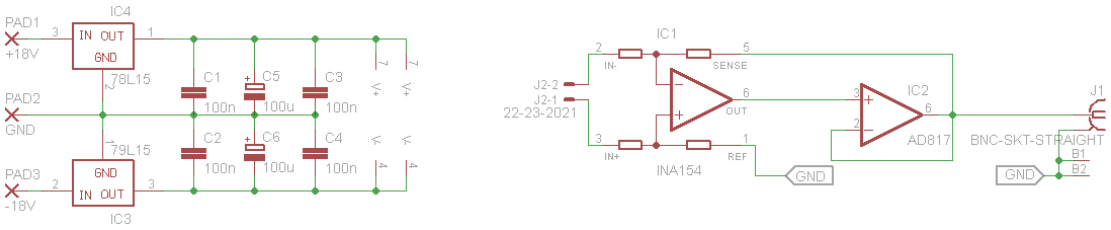

Figure 6.15: Circuit diagram of the buffer electronics for the analogue channels. The circuit on the left hand side generates a stable ±15V supply voltage for the main circuit. The circuit on the right hand side accepts the inputs on jumper J2-1 and J2-2. The signal is forwarded by IC1 and buffered by IC2 to allow for a higher load to be applied to the analogue channel.

taken of all channels show an average offset of $V_{off} = -194\mu\text{V} \pm 366\mu\text{V}$. This complies with the maximum specified offset voltage of $750\mu\text{V}$ for the differential amplifier.

The output voltage levels were compared using a 1kΩ resistor and a resistor with several MΩ (resistance of the Voltmeter) as different loads respectively. No significant differences were found with only marginal changes in the μV range occurring.

Next the noise level of the analogue channels is analysed with representative measurements taken on analogue channel 15. The background noise of the spectrum analyser in fig. 6.16 shows a slightly raised noise level up to 2MHz of −100dBm which afterwards drops to a white noise with a level of −110dBm. Fig. 6.16 also shows the noise measurement of channel 15. The noise level is generally raised compared to the noise level of the calibration by 10dB for higher frequencies. Up to a frequency of 6MHz the level is increased by 20dB. There are three distinct features at $2-3$MHz, 4MHz and 5MHz which do not show up on the calibration and are presumed to be generated by the electronics. The noise level is overall low and well within acceptable limits.

The speed of the analogue channels is analysed next. Observe the measurements of a rising slope with step sizes of 100mV, 1V, 10V and 20V in fig. 6.17(a) to 6.17(d). The graphs contain measurements with a load of 1kΩ and no load.

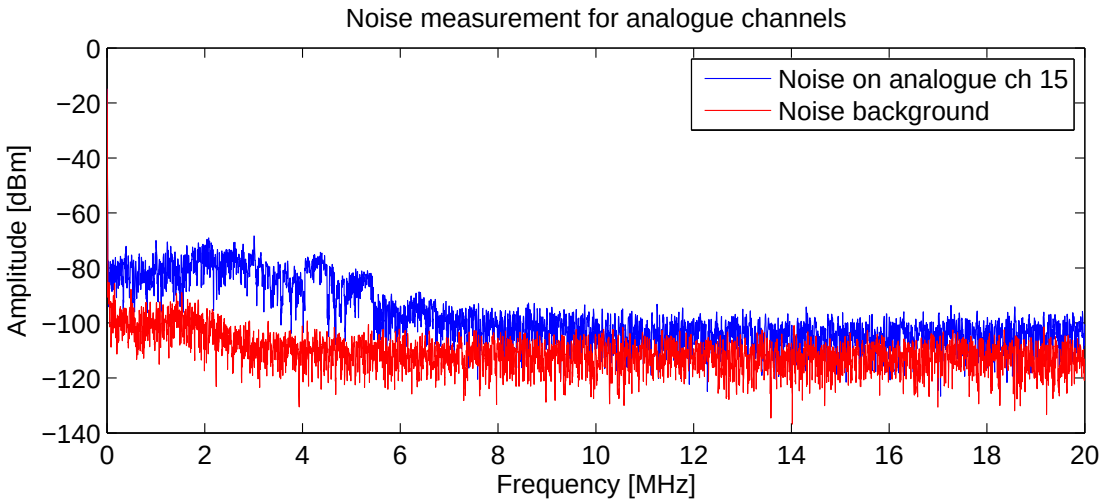

Figure 6.16: Noise measurement for analogue channels. Observe the noise measurement of an analogue channel with the noise background of the spectrum analyser used. The noise level of the analogue channel is generally raised by 10dBm while up to a frequency of 6MHz the noise level is raised by 20dBm with two distinct features occurring around 4 and 5MHz.

All measurements show no significant difference between the measurement with and without load. The rise times (10% to 90%) of voltage steps up to 10V are all similar with a mean of $\Delta t = 1.02\mu\text{s} \pm 0.06\mu\text{s}$ which agrees with the specified update rate of 1MHz. For the 20V step observe a rise time of $\Delta t = 1.34\mu\text{s}$ which is limited by the specified slew rate of $10\text{V}/\mu s$ of the FPGA board and thus is also in agreement with the specifications. The slew rates of the buffering differential amplifier ($14\text{V}/\mu\text{s}$) as well as the buffering amplifier ($350\text{v}/\mu\text{s}$) are not a limiting factor.

To measure the ground insulation the impedance has to be measured which will be done with the same technique as described in the digital electronics results chapter (see ch. 6.2.1). The measurement for the impedance of the analogue connectors is shown in fig 6.18.

Up to a frequency of 2kHz a high impedance of about $2\text{k}\Omega$ is observed which decreases afterwards due to capacitative effects. The minimum impedance is reached at a frequency

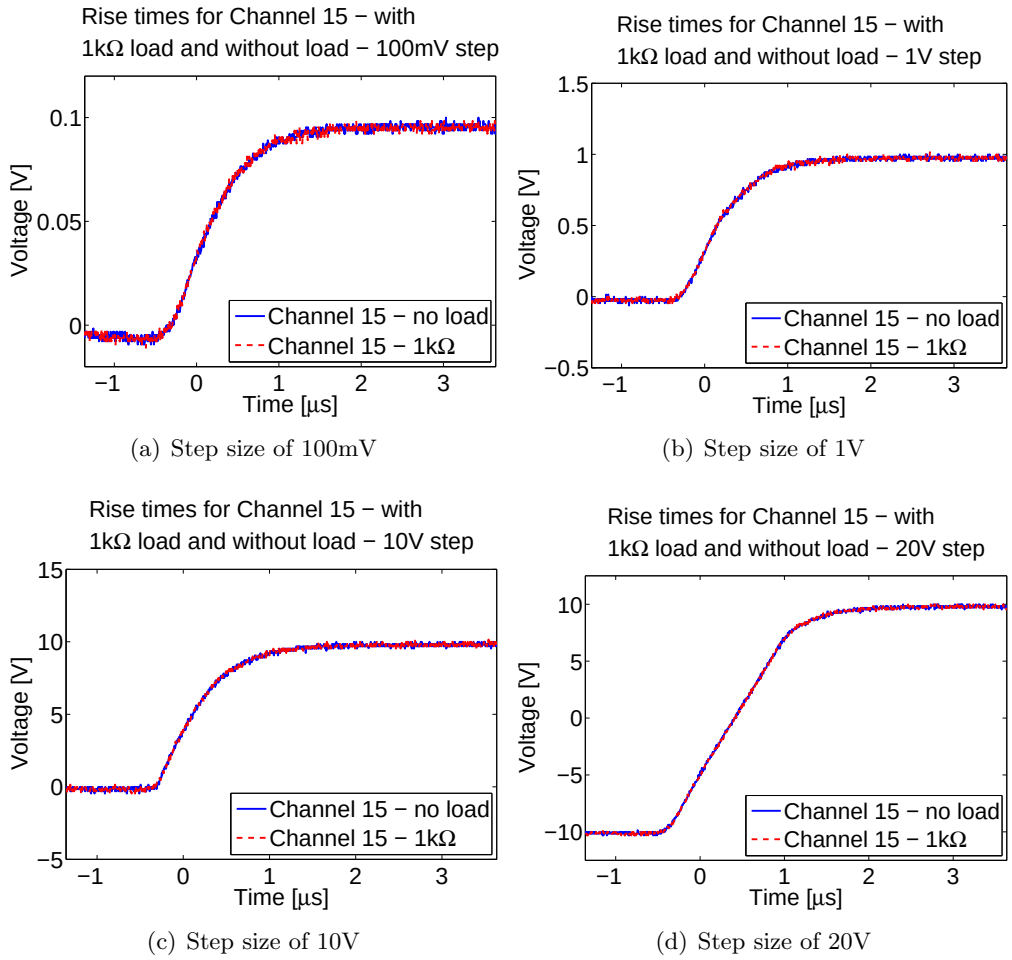

(a) Step size of 100mV

(b) Step size of 1V

(c) Step size of 10V

(d) Step size of 20V

Figure 6.17: Measurements of the rising slopes of channel 15 with varying stepsizes. a) Step size of 100mV. b) Step size of 1V. c) Step size of 10V. d) Step size of 20V. Note that all graphs except for (d) show an asymptotic approach towards the target voltage from the start while (d) is at first linear before asymptotically approaching the final value. This is caused by the slew rate of the analogue channels which do not allow for the voltage to be changed by the maximum amplitude in one refresh cycle.

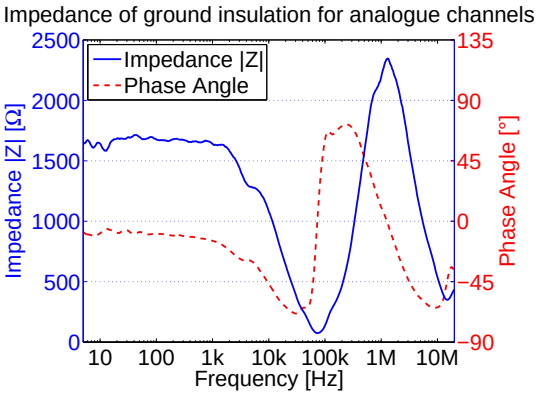

Figure 6.18: Using the circuit from fig. 6.11 the graph shows the impedance measurement of the analogue connectors. You can see that the resistance stays high up to a frequency of 10kHz when it steeply drops down unto nearly zero. It is subsequently followed by a large peak in resistance which is caused by the choke (see fig. 6.14)

of 70kHz. At around 100kHz an inductive resonance occurs in the phase angle followed by a peak in the impedance at 2MHz. This illustrates that the ground insulation of the analogue channels works well up to 10kHz and for frequencies spanning 300kHz − 5MHz. As with the digital channels most interference is expected to come from the mains frequency of 50Hz and other low frequencies. This shows that the analogue channels are well insulated against ground loops.

6.2.3 Summary

The buffering electronics devised for the digital and analogue channels successfully decouples clusters of digital channels and all individual channels for the analogue channels. For the digital channels the electronics effectively filter the signal and offer rise- and fall-times lower than the specified times for the FPGA board. A small delay between different digital channels has been measured but this is well below the maximum timing limit of 25ns. The impedance was measured to be $51 - 52\Omega$. The floating power supply successfully rejects ground loops up to 20kHz for clusters of 8 digital channels.

For the analogue channels rise times comparable to the FPGA specifications were measured. The noise level of the analogue channels is raised over the background noise by 20dBm and 10dBm for different frequency ranges respectively. The floating power supply successfully provides protection against ground loops up to a frequency of 10kHz.

6.3 Moving atoms

In order to move the MOT clouds to their destinations a commercial motorised actuator was acquired[12, 13] (see [56, 57] for experiments using the same technology). Fig. 2.1 contains a schematic showing the linear positioner used. The actuator has a specified maximum velocity of $v = 1\text{m/s}$ with an accuracy of the positional read out of $\Delta s = 2.15\mu\text{m}$ using the SinCos encoding option [55]. The positional accuracy for travel distances of 30cm, a typical distance in the set up, is specified to $\Delta s = 24\mu\text{m}$ [54]. In the following the control of the linear positioner is discussed and the calibration and characterisation of the equipment outlined.

6.3.1 Programming language

The program controlling the actuator was written in the IEC61131-3 programming language. It is a language which is suitable for automisation and consists of 5 sub languages. Functions written in either of these languages can be called in the code of the other languages. There are different applications for each language, three languages are graphically based, one of those takes the form of a top to bottom flow diagram whilst the two others are similar to LabVIEW programming. Of the two text based languages one is similar to assembly type whilst the other is a higher programming language. The graphical languages are suited to different purposes be it a repetitive movement or a dynamic control. The text based languages aim at code size. The storage space for

[12] Parker 406 XR actuator [54]
[13] Parker Compax3 controller [55]

commands is very limited on the controller of the actuator so code written in assembly is preferable to a code written in a higher language. With increased complexity, however, it is not feasible to maintain large amounts of assembly code and it was decided to employ the language which closely resembled LabVIEW. Subsequently it was shown that the programming content was low enough not to have to optimise the code for storage space, indeed only one sixth of the available storage space being used.

Program

The program (see fig 6.19) is set up to allow travel to three different positions[14]. Each position is controlled by a digital input. The signal from the digital channels is filtered to only trigger on a rising slope. Further it is identified which destination the carriage has been triggered to go to. This includes fail safes to prevent that more than one position can be triggered at a time. If no current movement is being executed the appropriate data for the triggered movement are selected and forwarded to the motor. The motor gets energised, executes the movement and shuts down. An output trigger is activated to signal the completion of the movement.

[14]this can be easily scaled up to 6 positions which is the number of usable digital inputs

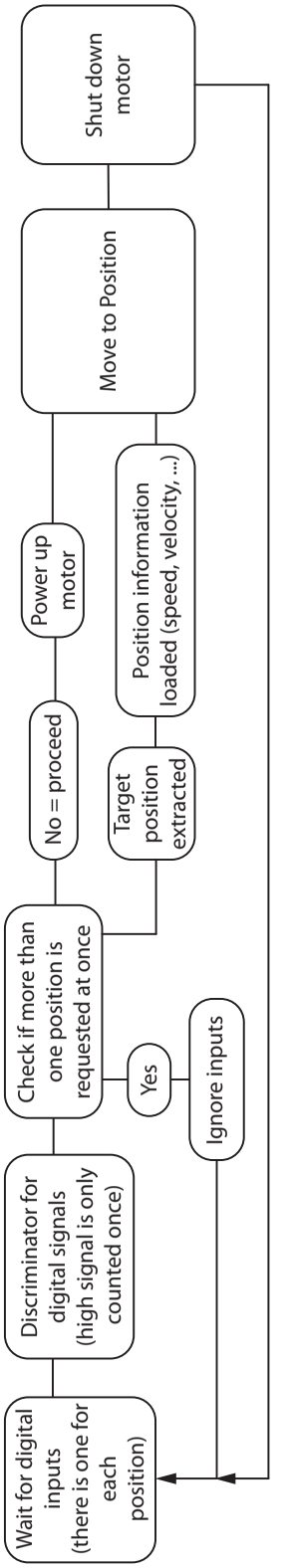

Figure 6.19: Main actuator control program. The program waits for digital inputs which is followed by sanity checks to ensure that no more than one destination is requested at any one time. The parameters for the movement are established, the rail is powered up, the carriage moves to its new position and the motor is powered down again.

6.3.2 Calibration

The actuator controller needs to be calibrated in order to achieve a desired accuracy of 10μm and a fast transfer speed. The main parameters are the maximum velocity, acceleration and "jerk", the first derivative of the acceleration. The maximum velocity of the hardware is specified to $v = 1\frac{\mathrm{m}}{\mathrm{s}}$ and is limited to $v = 1.25\frac{\mathrm{m}}{\mathrm{s}}$. It transpired that this velocity was never reached due to constraints in acceleration and "jerk" so this value is always left at the maximum of $v = 1.25\frac{\mathrm{m}}{\mathrm{s}}$. Acceleration also turned out to be non-critical. The "jerk", however, needs to be adjusted to achieve a stable movement. If the values are set too high an uncontrollable oscillation in the carriage is induced and the tracking of the carriage fails leading to an immediate shut down of the device. Stable operation was achieved using a jerk of $j = 35.000\frac{\mathrm{mm}}{\mathrm{s}^3}$ whilst the maximum acceleration sustained is $a = 6000\frac{\mathrm{mm}}{\mathrm{s}^2}$ which is noticeably below gravity. These parameters are invariant in direction, acceleration and deceleration even though the carriage load is not symmetric in the axis of travel.

The positioning, at first, ran short of the target distance by more than 1mm regardless of the direction of approach. One parameter used by the controller is the stiffness of the load, a measure of the bandwidth of the velocity control. By increasing this by a factor of five it was possible to reduce the tracking error to less than 10μm.

Further measurements were conducted to record the position tracking error at any time as well as velocity and position. Fig. 6.20 shows the position (dark blue) from -360.5cm (position of the MOT chamber) to 0cm (position of the science chamber) as well as the target speed (red) overlayed by the actual speed (blue) and the position tracking error(dark green). The transfer takes $t = 0.7$s.

It was noted that there was an oscillating position tracking error, caused by oscillations excited by the load of the carriage, see fig. 6.21.

The oscillating pattern of the position tracking signal of subsequent movement processes seems at first random though a frequency analysis shows that the frequency spectrum of

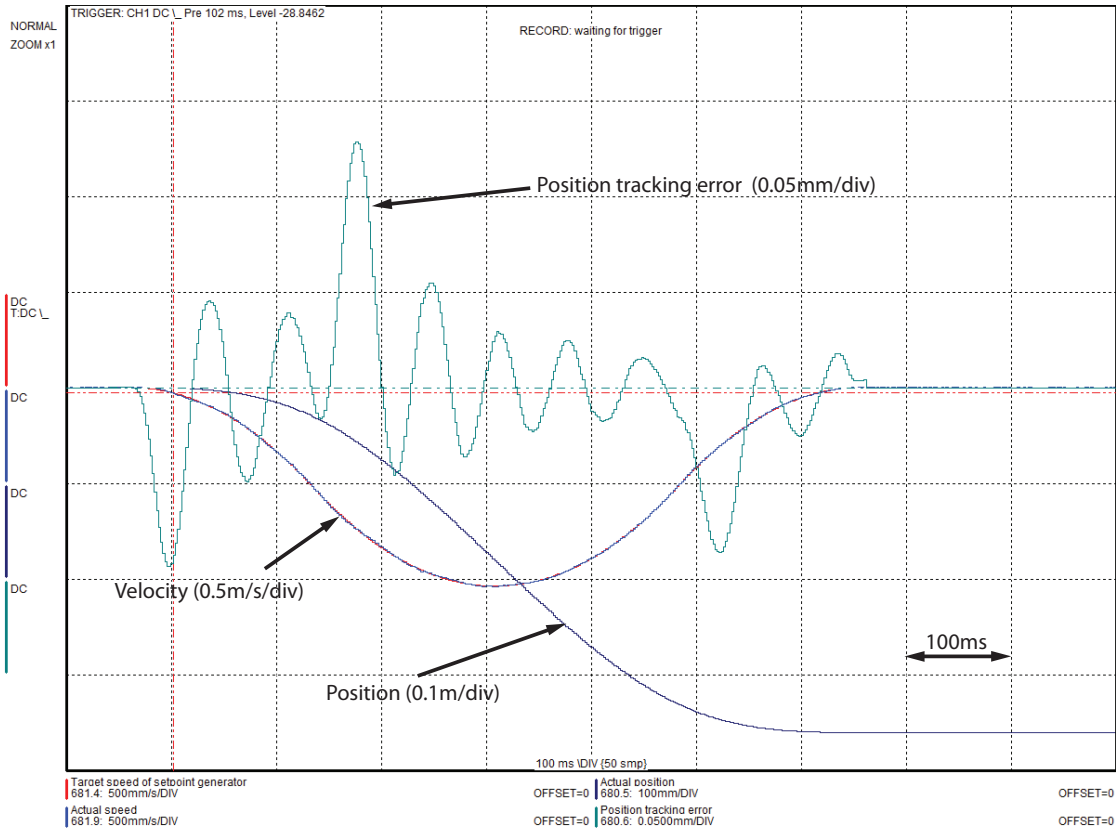

Figure 6.20: Diagnostic measurements of coil transfer from the science chamber to the MOT chamber. Illustrated is the position, velocity and position tracking error. The position changes from 0cm which is the position of the glass cell to -360.5cm which is the position of the MOT chamber. The modulus of the velocity increases at first to a maximum which is slightly larger than 1m/s and decreases afterwards. The position tracking error show an oscillating behaviour with a maximum amplitude of 0.2mm.

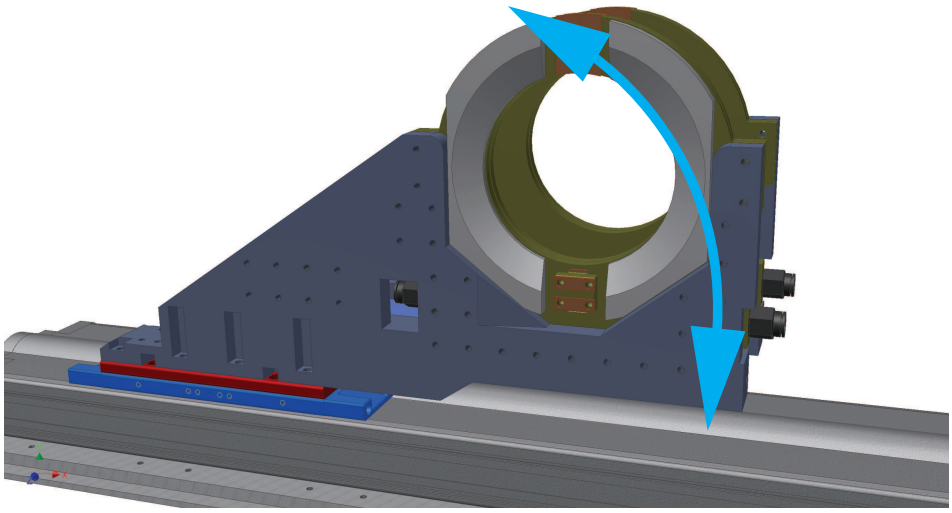

Figure 6.21: Oscillation of the carriage mount and coil. The coil mount has a design which is off-centred in order to allow for the space underneath the glass cell to be used. As a consequence of this a degree of freedom for oscillations has emerged.

excited frequencies is constant. This is also the case for the different movement directions the only difference being the magnitude of the spectrum as seen in fig. 6.22(a) and 6.22(b).

After the end of the movement the motor is shut down in order to remove any interference by EM noise. It is particularly interesting to see what happens to the carriage after the motor is unpowered. Fig. 6.23 shows the moment the motor switches off happens at the point where the tracking error goes abruptly to zero. The dark blue trace is again the position while the blue trace shows the velocity. Up to the point where the motor is shut down the trace shows a smooth curve held firmly in place and that the carriage overshoots the target distance. Following which oscillations in the mount and coils start move the carriage which oscillates back in this process by $\approx 13\mu$m.

It would be possible to increase the time at the end for which the carriage is held firmly in place. This would not, however, solve the problem of oscillations after a delayed shut down as the damping in the carriage load is insufficient to reduce the oscillation

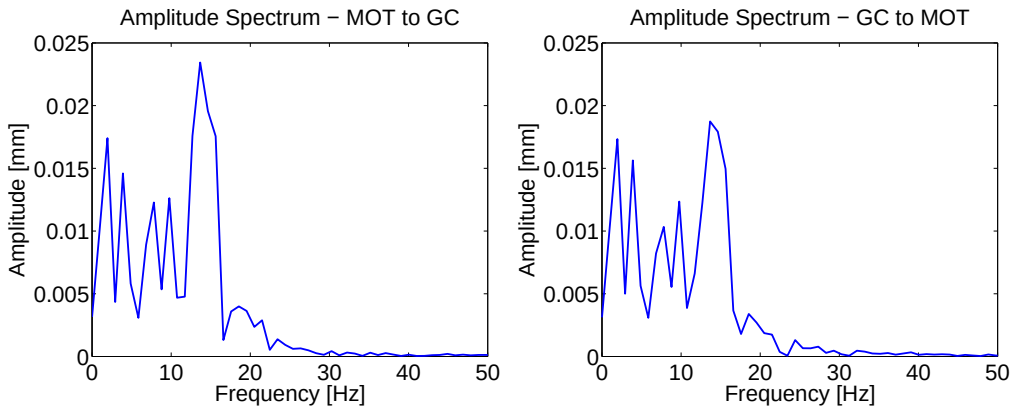

(a) Travel MOT to GC

(b) Travel GC to MOT

Figure 6.22: The graphs show a Fourier analysis of the oscillations of the position tracking error observed in fig. 6.21. a) shows the spectrum for a travel from the MOT chamber to the glass cell. b) is showing the spectrum of a transfer from the glass cell to the MOT chamber. It is interesting to note that despite the asymmetry of both movements the spectrum stays largely the same with the most apparent difference being the amplitude.

quickly enough. The movement of the carriage after shut down does itself constitute a very effective dampening process leading to a sufficient reduction of the oscillations after $\approx$ 10ms. Two main consequences follow from this, from fig. 6.23 the oscillation frequency is approximately $\nu = 1$kHz. The magnetic trap holding the atoms has to be set to a trap frequency sufficiently different to that of the carriage to avoid any heating excitations that might occur. The MOT coils and moving coils are both oil cooled (see also appendix A). In the current design all cooling bodies started to leak after about 100h of operation, as a result of which the structural design of the coil cooling bodies have to be reassessed to make sure that they permanently resist the stresses induced by the oscillations.

Overall the transfer speed (1m/s) and accuracy (10μs) are sufficient with the positioning accuracy largely exceeding the specifications of the system.

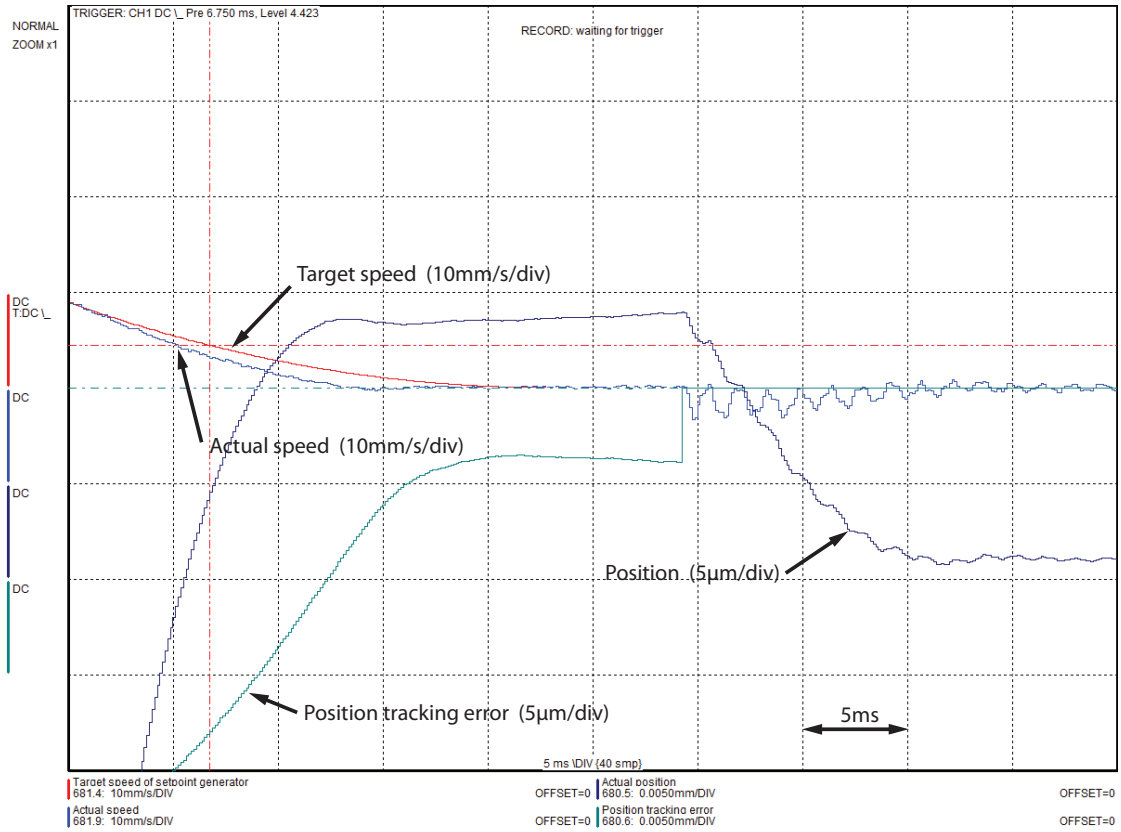

Figure 6.23: Diagnostic measurement of the carriage arriving at the glass cell. The target and actual velocity are slightly apart, the carriage position slightly overshoots the target position of zero. The position tracking error goes down to $\approx 4\mu$m until the rail controller considers the movement complete, at that point the rail powers down and the position tracking error disappears. The carriage is not electrically held at this point which allows the coil mount oscillations to transfer some of the energy to the carriage causing it to move. There is a slight oscillation in the velocity after switch off as well as the carriage moving back by 12μm giving the impression that the carriage has not arrived at the target position.

6.4 Glass cell

The experiments with the condensed/degenerate atom clouds are to happen in a glass cell made to satisfy several criteria. The cell needs to be very flat to allow for the microscope lenses to be positioned at the appropriate working distance. Losses have to be kept at a minimum as one of the goals of the experiment is to detect individual atoms, that each side has specialised coatings which reduce any reflections from incoming laser beams to an acceptable minimum. The coatings need to by optimised for the wavelengths of the respective lasers and the incident angles. This caused a some concern as the glass cell had to be designed before certain specific details of the final arrangement had not been decided. It was, however possible, to prepare the glass cell for several likely scenarios. For the coatings to be effective they need to be applied upon both the outside and the inside of the cell. The most common way to produce UHV glass cells is by a glass welding process which welds adjoining glass plates at temperatures of up to 800°C. The coatings do not survive these temperatures and they have to be applied afterwards, however, this does not permit application of the coatings from the inside. To overcome this limitation the glass cell for this experiment was glued together which is requiring curing temperatures of 150°C. This allows for the coatings to be applied prior to assembly.
Reflections within the glass caused by stray light from any light source can travel in a wave guide like manner throughout the glass of the cell. To obviate this effect the plates constituting the cell had black quartz glass fused to the plate edges thereby closing any optical path from one plate to another. By this means photons which, travel within one glass plate will be absorbed before they exit the plate.

6.5 Dipole trap laser system

In this section the experimental implementation of the dipole trap as presented in ch. 4.5 is described. The laser system is set up to meet the specifications of ch. 4.6.4 i.e. a laser

beam with a horizontal beam size of $w = 10\mu$m and a vertical beam size of $w = 394\mu$m. A schematic of the dipole trap laser system is shown in fig. 6.24. The system is based on commercially available 1550nm fibre amplifiers[15] and is designed to support two different configurations: a one-beam astigmatic trap as described in ch. 4.5 and a conventional crossed two-beam dipole trap. Three amplifiers are available, of which in the current set up a maximum of two are going to be used at any one time. As the amplifiers need to be seeded with a low power laser a diode laser was set up[16] with a maximum output power of 40mW. The diode laser comes fibre coupled and is connected to a splitter module based on the module design which was developed in the course of the Quantus project which miniaturised a BEC experiment for experiments in micro-gravity [60, 61].

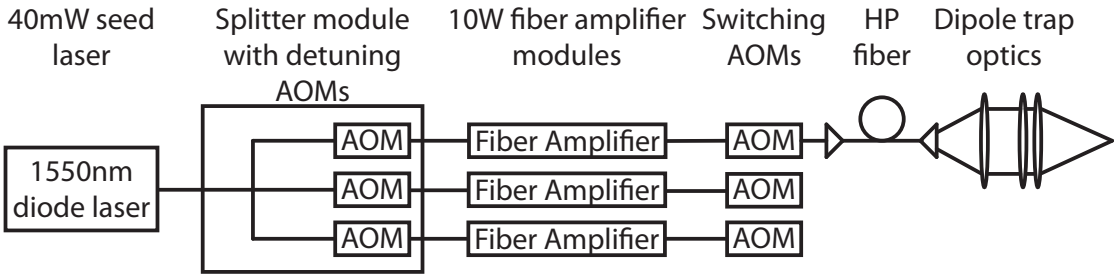

Figure 6.24: Schematic of the set up of the dipole trap laser system. A fibre-coupled 1550nm diode laser is coupled into a splitter module which splits the beam into three beams of equal power with the possibility of detuning the three beams to each other. The three beams are fibre coupled and connected to the 10W fibre amplifiers whose outputs are sent through high-power single pass AOMs and coupled into high-power fibres. The AOMS are solely used for switching the beams rather than further detuning the beams to each other. One of these fibres is inserted into the dipole trap optics which is mounted close to the experiment glass cell.

The splitter module at first splits the light into three linearly polarised light beams and then couples these into polarisation maintaining fibres with $\lambda/2$ plates in the line of the beam to match the polarisation to the slow axis of the optical fibre.

[15] Nufern 10W fiber amplifier [58]
[16] Thorlabs fibre coupled diode laser [59]

The design of the splitter module initially included the possibility to detune the laser beams to each other. This was initially planned to also generate the optical lattice using the fibre amplifiers. For that reason three AOMs are included in the module in double pass configuration while there is a lens behind the AOMs focussing the beam down onto the mirror in order to re-collimate the beam and reduce overall losses. As the optical lattice is going to be generated by a frequency doubled ND:YAG laser[17] this feature is obsolete for the time being and has been bypassed. If it turns out that detuning between the different fibre amplifiers is beneficial for some reason as yet unknown it is relatively straightforward to re-enable this feature.

The output fibres of the splitter module are directly inserted into the amplifiers. It is important that the seed power needs to be between $1 - 15$mW. The amplifiers are controlled by a switch which turns the pump diodes on and off and a potentiometer which can adjust the power between a minimum of 10% of the rated output power to the maximum output. This enables adjustment of the power between $1 - 10$W. In practice it was found that the potentiometer allows for a reduction of the output power to a minimum of 300mW which permits adjustment of the optical system without having to take precautions to protect the optical elements. Since the high power fibre couplers and the high power fibres in particular can be easily damaged by 1W when not properly aligned.

The output of the amplifiers comes through a fixed built in output fibre with a fixed built in output coupler which generates a collimated and linearly polarised beam.

This beam is sent through a high power AOM in single pass and is eventually coupled into the aforementioned high power fibres (HP fibers) which lead to the dipole trap optics. This last AOM is solely used to switch the laser output as all built in functions of the amplifiers are too slow.

[17] Coherent Verdi V12 [12]

6.5.1 Dipole trap - characterisation

In this section the dipole trap optics are described and characterised.

The dipole trap optics consist of a beam tube which collimates the laser beam and afterwards a cylindrical focussing lens and an aspherical focussing lens. The laser emits at high power with a core diameter of 8μm with an opening angle of 14°. An aspherical lens with a focal length of $f = 100$mm collimates the laser beam to a beam with a waist of $w_0 = 12.3$mm. A cylindrical lens with a horizontal focal length of $f = 5.15$m acts as the astigmatic element while an aspheric lens with a focal length of $f = 200$mm focusses the beam down with a focus in the vertical plane appearing after 19.2cm and a focus in the horizontal plane appearing after 20cm. The latter is the focus in which the atoms are actually trapped.

For characterising the beam profile in the horizontal focus a scanning slit profiler[18] is used. The profiler has scanning slits tilted 45° to the plane of the optical table producing projections in both horizontal and vertical axes.

With a large aspect between the two axes any slight tilt in any of the components will represent a distorted small focus which will appear larger than actual. The beam profiles with intensity distributions are illustrated in fig. 6.25 from which it is seen the trapping focus lies at $x = 0$mm with vertical focus at $x = -8$mm and an intermediate profile located at $x = -4$mm. This compares favourably with the theoretical predictions (see fig. 4.3).

Note that the measured profile of $x = -4$mm is normalized to it's peak value which explains the difference to the predicted graph. The vertical and horizontal profiles are displayed in 6.26(a) and 6.26(b) respectively.

The graphs have been fitted with a Gaussian beam shape at which the $1/e^2$ beam waists result as $w_v = 11.4\mu$m and $w_h = 386.1\mu$m compared to the theoretical predictions of $w_{v-theory} = 10.0\mu$m and $w_{h-theory} = 394\mu$m. The assumption of a Gaussian shape might

[18] Dataray Beam'R2 scanning slit beam profiler

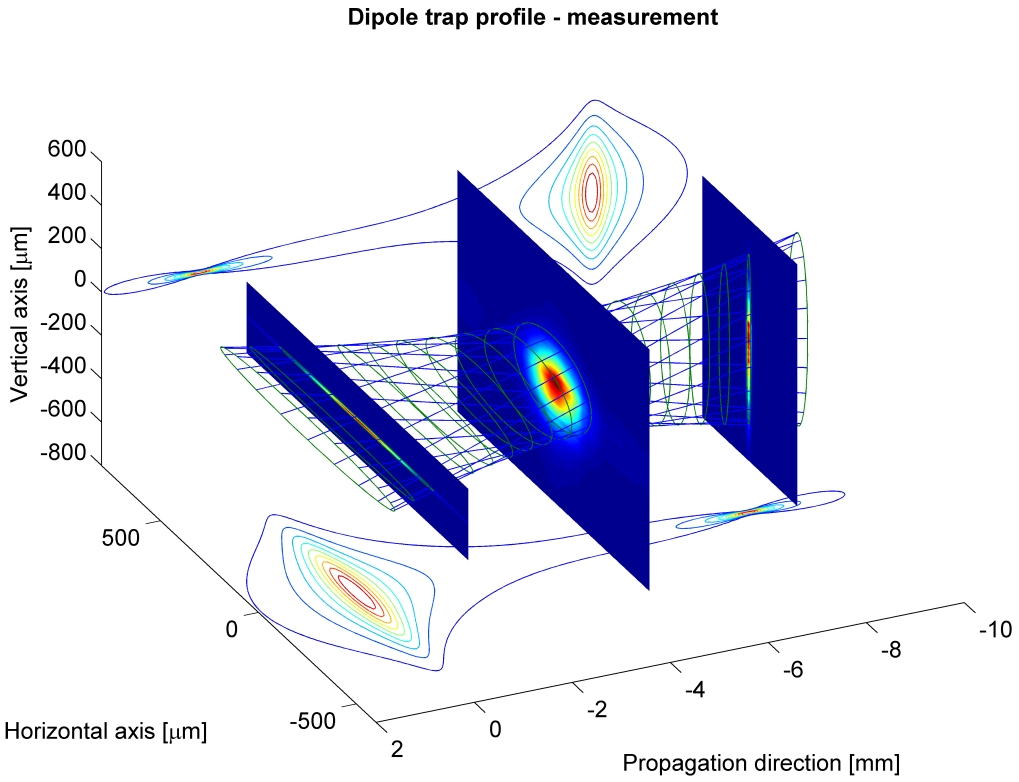

Figure 6.25: Beam profile measurements of separated horizontal and vertical foci as well as theoretical intensity distributions of the astigmatic dipole trap. The graph shows the horizontal (Propagation direction = 0) and vertical foci (Propagation direction = −8) as well as the intensity distributions (Contour plot in background). There is a good qualitative agreement with fig.4.3.

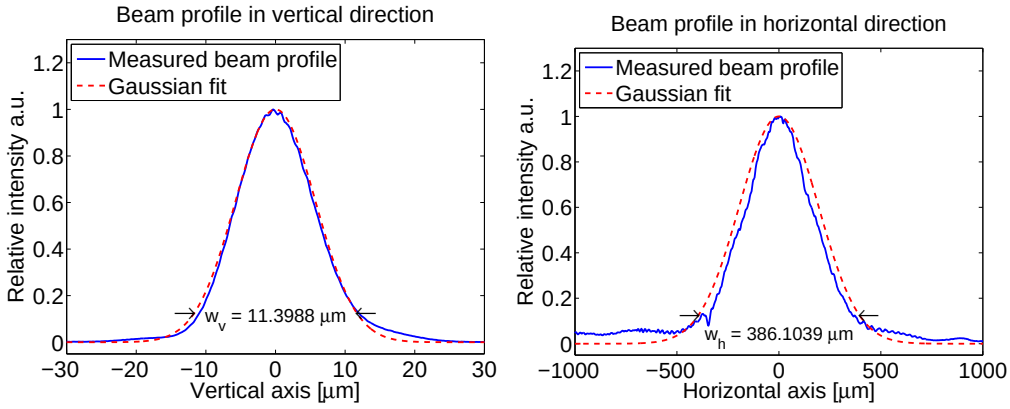

(a) Vertical profile

(b) Horizontal profile

Figure 6.26: Measured dipole trap profile. a) is showing the vertical beam profile. The measured focus of $w_v = 11.4\mu$m is in good agreement with the calculated focus of $w_{v-theory} = 10.0\mu$m. b) is showing the horizontal beam profile. The measured value of $w_h = 386.1\mu$m is also in good agreement with the calculated value of $w_{h-theory} = 394\mu$m. However the assumption of a Gaussian beam shape might not be accurate considering that the fit does in no way nicely describe the measured trace.

however not be optimal for considering fig. 6.26(b) shows a poor fit between the measured profile and the Gaussian fit. Having regard to the limitations expressed above the beam profiler results do give a good estimate and are within the tolerances set for the design of the system.

Chapter

7 Current Status and Outlook

In the course of this thesis a partially working apparatus has been constructed. The theoretical background work completed and the setting up of modules within the working apparatus has been successfully completed.

The theoretical models for optical atom trapping and optical lattices have been successfully demonstrated leading to a successful theoretical model of the system which were used to establish parameters and designs for the apparatus.

The electronics and optics for the dipole trap have been successfully assembled. The dipole trap optics have been characterised with satisfying results for the horizontal and vertical beam waists of $w_v = 11.4\mu$m and $w_h = 386.1\mu$m respectively. This is the first use of an astigmatic dipole trap for the generation of 2D quantum gases.

The computer code for controlling the experiment was composed and demonstrated to deliver a fast reliable and stable control of the experiment whilst allowing for flexible control of the different types of devices encountered in day to day laboratory work. The control system utilizes modern FPGA technology which is being used for the first time

in this research group. The software was successfully adapted and is now being used to control four different experiments.

The motorized translation stage was successfully programmed and subsequently calibrated to allow for fast and reliable transport of captured atoms with a precision of below 10μm. The evaluation also showed vibration resonances of the coil mount. In the future these measurements can be used to reduce vibrations in enhanced designs.

A design for the science chamber was produced which effectively reduces the sources of stray light so that the ability to produce images of single atoms is greatly enhanced. This design includes anti-reflection coatings both on the outside and the inside of the cell as well as for the first time incorporating black quartz as an optical isolation to reduce stray light.

The apparatus was successfully used to demonstrate the generation of a thermal atom cloud in the magneto optical traps and the successful transport of those atoms to the science chamber (see fig. 7.1 for an atom cloud imaged in the science chamber). Evaporation in the magnetic trap, however, has not proved successful. After careful analysis of the system, a problem with the vacuum was identified as the reason for the failed evaporation attempts. The vacuum readings, deduced from the currents of the ion getter pumps indicated that the pressure was sufficient, however, the life time of the atoms in the magnetic trap indicated otherwise. Leak testing resulted in vacuum changes with a delay of several days. Further testing has shown that the main leaked component is H_2O indicating diffusion through the UHV glue used in the construction of the MOT chamber. The chamber was subsequently disassembled and redesigned to replace the glue seal with indium seals [62, 63].

In the imminent future the vacuum chamber will be refitted with indium seals and a second 2D-3D MOT chamber installed to allow for separate loading of ^{87}Rb and ^{40}K MOTs. The coils mounted to the motorized translation stage will be redesigned for the cooling bodies have proven to be unable to resist the forces induced during transport and

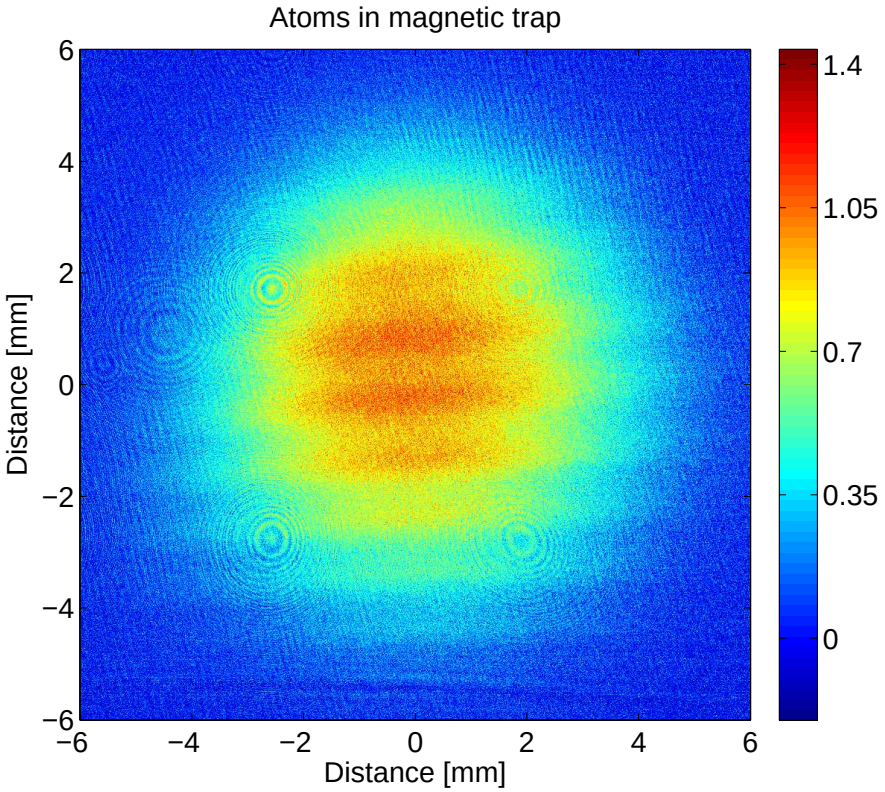

Figure 7.1: Thermal ^{87}Rb-atoms in a magnetic trap transferred to the science chamber. The image was taken using absorption imaging inside the magnetic trap, the colour map displays the optical density.

the magnetic fields leading to repeated leaks of the cooling fluid used. Feshbach coils will be installed around the glass cell into which the atoms will be immediately transferred, after successful transport, to minimize stress on the moving coils. As the name suggests these coils will also be used to achieve Feshbach resonances to generate Rb-K molecules. The microscope lenses will be installed and characterized together with the glass cell to establish the achievable resolution. Finally the SLM will be added to the experiment to allow for the versatile generation of optical lattices.

Appendix

A Oil cooling system

In this appendix I will first briefly detail out why the cooling technique described is necessary and afterwards explain the method used to cool the coils used for the magneto optical trap, transport and Feshbach resonances.

The use and application of the coils requires high magnetic fields and/or high gradients of the magnetic field. To keep the necessary currents low we elected to build the coils as small and compact as possible. This was done using copper film with neighbouring layers separated by a film of capton. This design presents problems in controlling the temperature of the coils since capton is both heat and current insulating the thermal energy inside the coils can only dissipate to the sides but not radially. The thermal energies involved in the design are however high enough to melt the coils if heat is not dissipated quickly enough. As a result the copper on the sides of the coil cannot be covered by an insulating layer of paint due to the insufficient heat conductive properties of such paint. For low voltages it would be possible to directly cool the copper with distilled water. For high voltages ($40 - 50$V) however electrolysis will be induced which

would cause the coils to disintegrate in the long term introducing an explosive mixture of oxygen and hydrogen in a high pressure environment ($4 - 5$Bar).

We found an oil based cooling fluid[1] which fulfils our requirements and allows to cool the copper directly. In order to use this cooling fluid we established a cooling circuit which is both temperature and pressure regulated. We also utilised the house water cooling system as a secondary circuit to achieve temperature control. The arrangement is shown in fig. A.1. The oil is kept inside the reservoir which feeds directly into the pump[2]. The output of the pump is guarded by a solenoid valve which is interlocked. From here the oil flows past the temperature sensor which feeds into the temperature controller and then to the four outputs and the pressure regulator[3]. The pressure regulator is set to maintain a constant oil pressure. The oil returns to the system through the flow indicators, which are also part of the interlocking system. The fluid passes another temperature indicator and enters the heat exchanger. The heat exchanger uses the house water as a coolant for the oil cooling system. The water flow is hereby controlled by the aforementioned temperature controller. After the heat exchanger the fluid returns to the reservoir. There are several ball valves which can be used to close pipelines or in an emergency to release the oil from the system.

There is a double tier interlocking system in place. The first tier indicates a problem with the coils and enables and disables the power supplies. This is triggered by a rise in the oil temperature measured by the temperature sensor also used by the temperature controller. The second tier indicates problems with the pump and shuts down the pump as well as disabling the power supplies to the coils. Triggers for the second tier are on the one hand a fill-level indicator in the reservoir and low flow through the flow indicators. Both assume under fault conditions that a major leak has occurred, either an oil spill or a coil overheating. On the other hand there is also a bi-metal switch attached to the

[1] Paratherm CR [64]
[2] Edur Model LBU 403 A135L / 3,0 KW
[3] Burling Instruments Back Pressure Regulator Model BS1.0-5 I I 4115-28131120

pump which triggers at $32.5°C$ (flash point of the cooling fluid is $40°C$). This prevents overheating and can be triggered if the water cooling valves are accidentally closed.

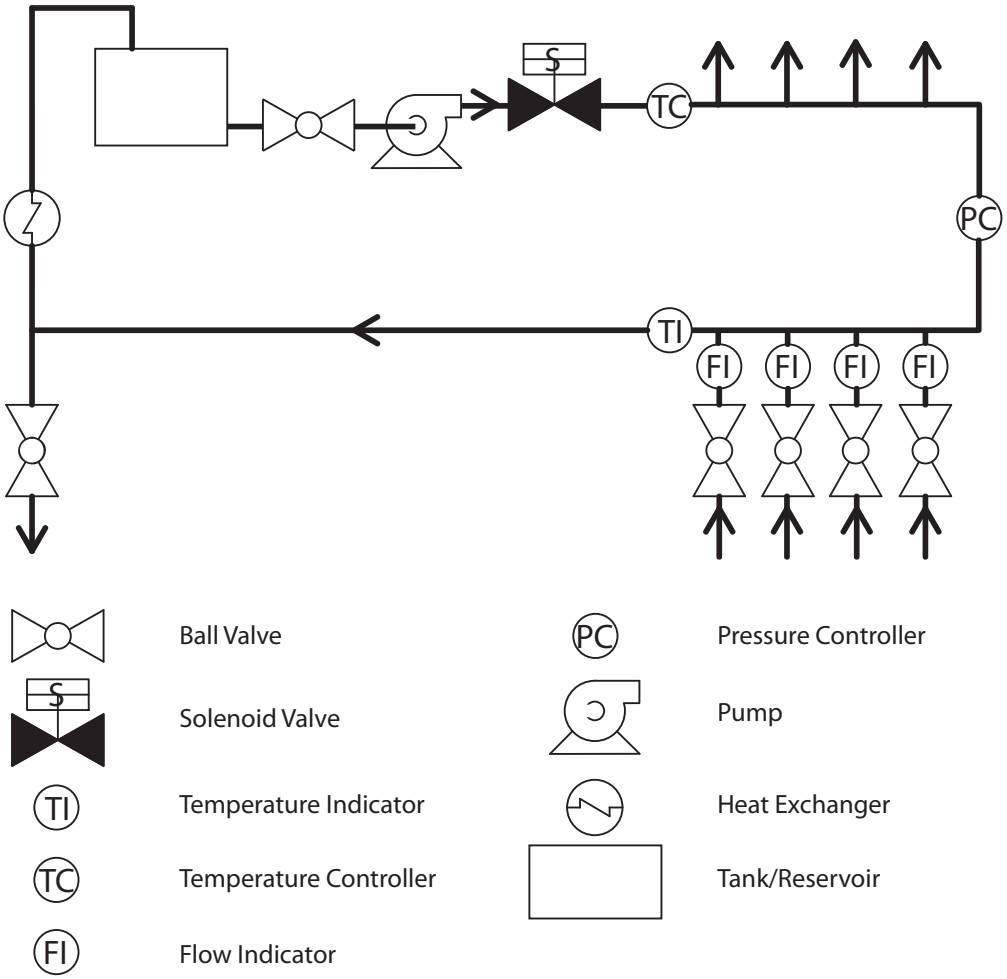

Figure A.1: Schematics of oil cooling circuit. The oil is stored in the reservoir which feeds into the pump which in return transfers the fluid to the outputs. Next to the outputs is a pressure controller which lets part of the fluid bypass any attached devices if the pressure rises too high. The fluid re-enters the system at the return inlets and gets subsequently cooled down in the heat exchanger.

References

[1] M. H. Anderson, J. R. Ensher, M. R. Matthews, C. E. Wieman, and E. A. Cornell. *Science*, 269(198), 1995.

[2] K. B. Davis, M.-O. Mewes, M. R. Andrews, N. J. van Druten, D. S. Dufree, D. M. Kurn, and W. Ketterle. *Phys. Rev. Lett.*, 75(3969), 1995.

[3] Markus Greiner, Olaf Mandel, Tilman Esslinger, TW Hänsch, and I Bloch. Quantum phase transition from a superfluid to a Mott insulator in a gas of ultracold atoms. *Nature*, pages 39–44, 2002.

[4] Anderson, P. W. *Phys. Rev.*, 109(1492), 1958.

[5] E. Abrahams, P.W. Anderson, D.C. Licciardello, and T.V. Ramakrishnan. Scaling Theory of Localization: Abscence of Quantum Diffusion in Two Dimensions. *Phys. Rev. Lett.*, 42(10):673, 1979.

[6] Juliette Billy, Vincent Josse, Zhanchun Zuo, Alain Bernard, Ben Hambrecht, Pierre Lugan, David Clément, Laurent Sanchez-Palencia, Philippe Bouyer, and Alain

Aspect. Direct observation of Anderson localization of matter waves in a controlled disorder. *Nature*, 453(7197):891–4, June 2008.

[7] S. Trotzky, P. Cheinet, S. Folling, M. Feld, U. Schnorrberger, A. M. Rey, A. Polkovnikov, E. A. Demler, M. D. Lukin, and I. Bloch. Time-Resolved Observation and Control of Superexchange Interactions with Ultracold Atoms in Optical Lattices. *Science*, 319(5861):295–299, 2008.

[8] W. S. Bakr, J. I. Gillen, A. Peng, S. Fölling, and M. Greiner. A quantum gas microscope for detecting single atoms in a hubbard-regime optical lattice. *Nature*, 462(74), 2009.

[9] JF Sherson, Christof Weitenberg, Manuel Endres, Marc Cheneau, Immanuel Bloch, and Stefan Kuhr. Single-atom-resolved fluorescence imaging of an atomic Mott insulator. *Nature*, 467(7311):68–72, September 2010.

[10] L. Marcassa, G. Telles, S. Muniz, and V. Bagnato. Collisional losses in a K-Rb cold mixture. *Physical Review A*, 63(1):013413, December 2000.

[11] J. Goldwin, S. Papp, B. DeMarco, and D. Jin. Two-species magneto-optical trap with ^{40}K and ^{87}Rb. *Physical Review A*, 65(2):1–4, January 2002.

[12] Coherent. Specifications Verdi V-series. *URL:*
http : //www.coherent.com/downloads/VerdiFamily_DSrevC_0111.pdf.
accessed 11/09/12.

[13] Mitutoyo. Specifications of G Plan Apo microscope lenses. *URL:*
http : //www.mitutoyo.com/pdf/E4191 − $378_0$10611.pdf.
accessed 12/09/12.

[14] National Instruments. Specifications of NI 7841R. *URL:*
http : //www.ni.com/pdf/manuals/372492c.pdf.
accessed 12/09/12.

[15] AL Migdall, JV Prodan, and WD Phillips. First observation of magnetically trapped neutral atoms. *Physical Review Letters*, 54(24), 1985.

[16] Steven Chu, L Hollberg, JE Bjorkholm, Alex Cable, and A Ashkin. Three-dimensional viscous confinement and cooling of atoms by resonance radiation pressure. *Physical Review Letters*, 55(1), 1985.

[17] H. J. Metcalf and P. van der Straten. *Laser Cooling and Trapping*. Springer, New York, 1. edition, 1999.

[18] TW Hänsch and AL Schawlow. Cooling of gases by laser radiation. *Optics Communications*, 13(I):68–69, 1975.

[19] PD Lett, RN Watts, and CI Westbrook. Observation of atoms laser cooled below the Doppler limit. *Physical Review Letters*, 61(2):169–173, 1988.

[20] J. Dalibard and C. Cohen-Tannoudji. Laser cooling below the Doppler limit by polarization gradients: simple theoretical models. *Journal of the Optical Society of America B*, 6(11):2023, November 1989.

[21] Kb Davis, Mo Mewes, Ma Joffe, Mr Andrews, and W Ketterle. Evaporative cooling of sodium atoms. *Physical review letters*, 74(26):5202–5205, June 1995.

[22] W Ketterle and DS Durfee. Making, probing and understanding Bose-Einstein condensates. *Arxiv preprint*, 1999.

[23] Wolfgang Ketterle. Making, probing and understanding ultracold Fermi gases. *Arxiv preprint arXiv:0801.2500*, 2008.

[24] R Zallen and H Scher. Percolation on a Continuum and the Localization-Delocalization Transition in Amorphous Semiconductors. *Phys. Rev. B*, 4(12):4471, 1971.

[25] L Pezzé, M Robert-de Saint-Vincent, T Bourdel, J-P Brantut, B Allard, T Plisson, A Aspect, P Bouyer, and L Sanchez-Palencia. Regimes of classical transport of cold gases in a two-dimensional anisotropic disorder. *New J. Phys.*, 13:095015, 2011.

[26] S.S. Kondov, W.R. McGehee, J.J. Zirbel, and B DeMarco. Three-Dimensional Anderson Localization of Ultracold Matter. *Science*, 334:66, 2011.

[27] M. Holynski. *Creating a two dimensional cold mixture experiment.* PhD thesis, University of Birmingham, 2012.

[28] M. Prentiss, A. Cable, J.E. Bjorkholm, S. Chu, E.L. Raab, and D.E. Pritchard. Atomic-density-dependent losses in an optical trap. *Opt. Lett.*, 13(6):452, 1988.

[29] A. Ashkin. Trapping of atoms by resonance radiation pressure. *Physical Review Letters*, 40(12):729–732, 1978.

[30] A. Ashkin. Applications of laser radiation pressure. *Science (New York, N.Y.)*, 210(4474):1081–8, December 1980.

[31] A. Ashkin. Stable radiation-pressure particle traps using alternating light beams. *Optics letters*, 9(10):454–6, October 1984.

[32] Steven Chu, JE Bjorkholm, A Ashkin, and A Cable. Experimental observation of optically trapped atoms. *Physical Review Letters*, 57, 1986.

[33] Rudolf Grimm, M. Weidemüller, and Y.B. Ovchinnikov. Optical dipole traps for neutral atoms. *Advances in atomic, molecular, and optical physics*, 42:95–170, 2000.

[34] D. A. Steck. *Rubidium 87 Line Data*, rev. 2.0.1 (2008).
URL: http://steck.us/alkalidata/rubidium87numbers.pdf, 2008.

[35] D C McKay and B DeMarco. Cooling in strongly correlated optical lattices: prospects and challenges. *Reports on Progress in Physics*, 74(5):054401, May 2011.

[36] JP Gordon and A Ashkin. Motion of atoms in a radiation trap. *Physical Review A*, 21:1606–1617, 1980.

[37] C. Becker. *Multi component Bose-Einstein condensates.* PhD thesis, Universität Hamburg, 2008.

[38] Toptica. Specifications of a variable anamorphic prism pair. *URL:* http : //www.toptica.com/uploads/media/toptica_MA_APP − J.pdf. accessed 12/09/12.

[39] Matthew P. A. Fisher, Peter B. Weichman, G. Grinstein, and Daniel S. Fisher. Boson localization and the superfluid-insulator transition. *Phys. Rev. B*, 40(1):546–570, Jul 1989.

[40] D. Jaksch, C. Bruder, J. I. Cirac, C. W. Gardiner, and P. Zoller. *Phys. Rev. Lett.*, 81(3108), 1998.

[41] Dieter Jaksch. *Bose-Einstein condensation and applications.* PhD thesis, 1999.

[42] M. Greiner. *Ultracold quantum gases in three-dimensional optical lattice potentials.* PhD thesis, Ludwig-Maximilians-Universität, 2003.

[43] Maciej Lewenstein, Anna Sanpera, Veronica Ahufinger, Bogdan Damski, Aditi Sen(De), and Ujjwal Sen. Ultracold atomic gases in optical lattices: mimicking condensed matter physics and beyond. *Advances in Physics*, 56(2):243–379, March 2007.

[44] C. Kittel. *Introduction to Solid State Physics.* Wiley, sixth edition, 1986.

[45] P. B. Blakie and C. W. Clark. *J. Phys. B*, 37(1391), 2004.

[46] Michael Köhl, Henning Moritz, Thilo Stöferle, Kenneth Günter, and Tilman Esslinger. Fermionic Atoms in a Three Dimensional Optical Lattice: Observing Fermi Surfaces, Dynamics, and Interactions. *Physical Review Letters*, 94(8):1–4, March 2005.

[47] Eigen C++ project. Member function documentation. *URL:* http : //eigen.tuxfamily.org/dox/classEigen_1_1EigenSolver.html. accessed 12/06/12.

[48] National Instruments. Specifications of NI PXI-8108 RT. *URL:* http : //www.ni.com/pdf/manuals/372561e.pdf. accessed 12/09/12.

[49] United States Patent. Ground-loop interruption circuit. *URL:* http : //patents.com/us − 5103109.html. accessed 12/09/12.

[50] Burr-Brown. Differential amplifier INA154 data sheet. *URL:* http : //www.ti.com/lit/ds/symlink/ina154.pdf. accessed 12/09/12.

[51] NVE Corporation. Digital isolator IL715 data sheet. *URL:* http : //www.nve.com/Downloads/il71x.pdf. accessed 12/09/12.

[52] Texas Instruments. Digital buffer SN74BCT data sheet. *URL:* http : //www.ti.com/lit/ds/symlink/sn74bct25244.pdf. accessed 12/09/12.

[53] Analog Devices. High speed amplifier AD817 data sheet. *URL:* http : //www.analog.com/static/imported − files/data_sheets/AD817.pdf. accessed 12/09/12.

[54] Parker Hannifin Corporation. Specifications of XR-series actuators. *URL:*
http : //divapps.parker.com/divapps/emn/
pdf/XR/404XR_406XRManual.pdf.
accessed 11/09/12.

[55] Parker Hannifin Corporation. Manual and specifications of Compax3 Controller. *URL:*
http : //divapps.parker.com/divapps/eme/EME/Literature_List/
Dokumentationen/C3T30%20eng.pdf.
accessed 11/09/12.

[56] Robert L.D. Campbell, Robert P. Smith, Naaman Tammuz, Scott Beattie, Stuart Moulder, and Zoran Hadzibabic. Efficient production of large ^{39}K Bose-Einstein condensates. *Physical Review A*, 82(6):0–5, December 2010.

[57] Bernd Fröhlich, Michael Feld, Enrico Vogt, Marco Koschorreck, Wilhelm Zwerger, and Michael Köhl. Radio-Frequency Spectroscopy of a Strongly Interacting Two-Dimensional Fermi Gas. *Physical Review Letters*, 106(10):16–19, March 2011.

[58] Nufern. Specifications of NuAMP-1550 fiber amplifiers. *URL:*
http : //www.nufern.com/filestorage/fiber_amplifiers/
NuAMP − 1.5DataSheetWEB.pdf?9556.
accessed 11/09/12.

[59] Thorlabs. Specifications of SFL1550S laser diode. *URL:*
http : //www.thorlabs.de/Thorcat/21000/SFL1550S − SpecSheet.pdf.
accessed 11/09/12.

[60] W. Lewoczko-Adamczyk. *Bose-Einstein Condensation in Microgravity.* PhD thesis, Humboldt-Universität zu Berlin, 2008.

[61] A. Vogel. *Bose-Einstein condensates for space applications and novel teaching concepts*. PhD thesis, Universität Hamburg, 2009.

[62] Bernd Kaltenhäuser, Harald Kübler, Andreas Chromik, Jürgen Stuhler, and Tilman Pfau. Low retaining force optical viewport seal. *The Review of scientific instruments*, 78(4):046107, April 2007.

[63] T. J. Manuccia. High temperature ultrahigh vacuum infrared window seal. *Review of Scientific Instruments*, 52(12):1857, 1981.

[64] Paratherm Corporation. Specifications Paratherm CR cooling fluid. *URL:* http : //www.paratherm.com/wp − content/uploads/2011/12/CREngBull.pdf. accessed 11/09/12.

Acknowledgements

At first I would like to thank Prof Kai Bongs for the opportunity to complete my PhD in his group. Kai also hugely contributed to this work in countless discussions with his ideas and the gift to spot obvious mistakes which everyone else overlooks.

I'd like to thank Dr Jochen Kronjäger without whom the experiment would be far of from where it is now. His unsurpassed knowledge of electronics and hill walking have led to many memorable moments including Scafell Pike trying to kill us. I wish Andrea and him the best of luck and much happiness together and with their new baby girl!

I want to thank my colleagues Michael Holynski, Nadine Meyer, Marisa Perea Ortiz and our latest addition Charlotte O'Neale. Mike, the prank master, you could never get him but infuriatingly enough he would always get you. It seems though that this time I outclassed him and pulled off one of the greatest pranks in cold atom history! Nadine who's been my compatriot since Hamburg and Marisa who's always been a sun of happiness for the group. I wish especially Mike well in the endeavour to write an embarrassing speech. We have been a great team and it is sad to see this time come to an end.

ACKNOWLEDGEMENTS

I'd like to thank my friends in particular Steven Johnson who is about to become a time lord and my former house mate Ole Kock (kei-oh-cee-kei) as well as my brothers in arms from Hamburg Martin Hierholzer and Andreas Eich. Special thanks goes to John Candy who will never run out of ideas of how to fix *this* or how *that* might be useful at some point.

I also want to thank all the other members of the Quantum matter group. You all have made this a very special four years to me.

Special thanks goes to Steven Brooks and the workshop team who were quite often overburdened with our jobs.

I would like to thank Kai, Jochen, Mike, John and Norman Hodgkiss for proof reading my thesis. Kai must now be able to recite the one or the other passage out of the top of his head having read certain parts three times whilst Jochen and Mike have given invaluable input on chapters covered by their expertise. John and Norman have not left a single word unturned in the attempt to polish up my English. This thesis would lie in ruins without your huge efforts!

A lot of thanks goes to my brothers and sisters Kristina, Elske, Jan-Tido, Grietje and my brothers-in-law Pierre Bubas and Peter vom Stein as well as Lukas Schellenberger and Lisa Rebber.

Thank you so much to my parents Ulrike and Peter for their continuous support all the time.

Last but not least I want to give huge thanks to my wonderful fiancée Gemma Candy and our son Stewart for much needed support and patience. I could not have done it without you!